

THEORETICAL INVESTIGATIONS OF DELAY INDUCED EFFECTS IN SEMICONDUCTOR LASERS WITH OPTICAL AND OPTOELECTRONIC FEEDBACK

by

Bejoy Varghese

Reg No. 3665

in partial fulfillment of the requirements for the degree of

Doctor of Philosophy

in Science

at the Cochin University of Science and Technology,

Supervisor: Prof. V. M. Nandakumaran

International School of Photonics

Cochin University of Science and Technology

December 2015

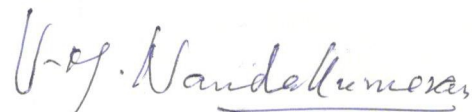
**INTERNATIONAL SCHOOL OF PHOTONICS
COCHIN UNIVERSITY OF SCIENCE AND TECHNOLOGY
COCHIN -682022, KERALA, INDIA**

Dr. V. M. Nandakumaran

Certificate

This is to certify that the thesis entitled “**Theoretical investigations of delay induced effects in semiconductor lasers with optical and optoelectronic feedback**” submitted by **Mr. Bejoy Varghese**, is an authentic record of research work carried out by him under my guidance and supervision in partial fulfilment of the requirement of the degree of Doctor of Philosophy of Cochin University of Science and Technology, under the Faculty of Science and has not been included in any other thesis submitted previously for the award of any degree.

Kochi-682022
13 - 12- 2015



Dr. V. M. Nandakumaran
(Supervising guide)

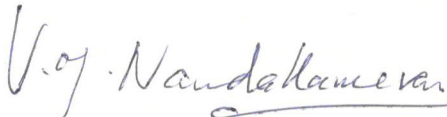
**INTERNATIONAL SCHOOL OF PHOTONICS
COCHIN UNIVERSITY OF SCIENCE AND TECHNOLOGY
COCHIN -682022, KERALA, INDIA**

Dr. V. M. Nandakumaran

Certificate

This is to certify that the thesis entitled “**Theoretical investigations of delay induced effects in semiconductor lasers with optical and optoelectronic feedback**” submitted by **Mr. Bejoy Varghese**, has incorporated all the relevant corrections and modifications suggested by the audience during the pre-synopsis seminar and recommended by the Doctoral Committee.

Kochi-682022
13- 12- 2015


Dr. V. M. Nandakumaran
(Supervising guide)

Phone: +91 9895189159 Fax: 0091-484-2576714.
Email: nandak@cusat.ac.in, nandakumaranvm@gmail.com

DECLARATION

Certified that the work presented in the proposed thesis entitled “**Theoretical investigations of delay induced effects in semiconductor lasers with optical and optoelectronic feedback**” is based on the original work done by me under the guidance of Dr. V.M. Nandakumaran, Professor (Retired), International School of Photonics, Cochin University of Science and Technology, Kochi-22, India and it has not been included in any other thesis submitted previously for award of any degree.

Kochi – 682 022

18/11/2015


Bejoy Varghese

ACKNOWLEDGEMENTS

I would like to express my gratitude to my supervisor, Dr. V. M. Nandakumaran, whose expertise, understanding and patience added to my research experience. His support and motivation helped me overcome many crisis situations and finish my dissertation. I would like to thank Dr. V. P. N. Nampoore, for his constant encouragement and help since my graduate years. A very special thanks to Dr. P. Radhakrishnan, former director of ISP, for his support and timely actions on financial matters regarding my fellowship. I also extend heartfelt thanks to Dr. M. Kailasnath, Director of ISP and Dr. Sheenu Thomas for their help and support at different stages of my research. I greatly appreciate the help from Dr. Binoy Goswami, Scientist, BARC for his help during the initial stages of the investigation. Dr. Manu Punnen John's insightful comments and constructive criticism were thought provoking and they helped me to focus on my ideas. I am grateful to him for the long discussions that helped me sort out the technical difficulties of my work. I am also indebted to Dr. S. Rajesh and Dr. Jijo P. Ulahannan, who collaborated with me at different stages of my work. Deepest gratitude to Sani and Deepthi, who were my companions in many long journeys during these years and supported me in difficult situations. Throughout the period of my research work, it was the care and support of my friends and colleagues that helped me to overcome setbacks and kept me sane. My heartfelt thanks to Nideep, Ajina, Roopa, Bony, jaison, Adrine, Ratheesh, Linesh, Pradeep, Mathew, Linslal, Libish, Bobby, Sony, Anand, Aparna, Roseleena, Vijesh, Indu, Divya, Suneetha, Jessy, Remya, Manju, Sister Anju and all who contributed to a pleasant and positive environment in the department. I would also like to thank my family for the support they provided me through my entire life. Finally, I appreciate the financial support from UGC and BRNS that funded parts of the research discussed in this dissertation.

PREFACE

Bejoy Varghese

Kochi 22, December 2015

Semiconductor lasers with different types of feedback schemes have been an active research area for many years. Feedback can induce complex phenomena in semiconductor lasers and their investigations often helped to understand the inner mechanisms of the laser. The possibility of using high dimensional chaos induced in semiconductor lasers by delayed feedback, for secure communication systems was a major motivation for intense research in the subject. Recently these systems also served as a testbed for general investigations on delay dynamical systems. The present study focuses on the aspects of the dynamical behavior of semiconductor lasers which are induced by delay feedback.

Chapter 1: First chapter introduces the subject of semiconductor lasers with delay feedback. The subject combines two well established research fields - theory and modeling of semiconductor lasers and delay dynamical systems. Necessary aspects of the operational principles and physics of semiconductor lasers required for the following chapters are discussed. Interplay of nonlinearities and delay plays a crucial role in producing the complex dynamics in semiconductor lasers when feedback is applied. Different sources of nonlinearities in the laser active medium are briefly described. Delay systems are introduced with relevant examples. Because of their high dimensionality, delay systems can exhibit very complex dynamics. Numerical methods used to simulate delay differential equation are detailed in the following section. These methods are obtained by modifying the Runge-Kutta methods of different orders which are used to solve ordinary differential equations. We first give an account of different Runge-Kutta methods and then describe how they can be modified to properly include the delay variable. We briefly go through some of the excit-

ing and relevant phenomena in the dynamics of semiconductor lasers with delay feedback, already reported in literature. Their physical significance and possible technological applications are discussed. Phenomena of Hopf bifurcation is detailed with an example as it is required to introduce the stability analysis of the delay differential system discussed in second chapter.

Chapter 2: In the second chapter we do the stability analysis of the delay differential system that describe the dynamics of a semiconductor laser with optoelectronic feedback. The general procedure for the stability analysis of delay systems, which is adopted from literature, is explained before we come to our derivations and results. For delay systems, the characteristic equation is transcendental and can have many solutions. We find the nature of the eigen values of the characteristic equation in the feedback strength-delay parameter space. Curves are obtained in the parameter space where real part of the eigen value vanishes which correspond to Hopf bifurcations. To get the direction of Hopf bifurcation, derivative of the real part of the eigen value with respect to delay are calculated. The dynamics of the semiconductor laser with optoelectronic feedback is simulated and compared with the analytical results. We compute how the change in nonlinear gain reduction factor and bias current affect Hopf bifurcations. We also find regions in the parameter space where fixed point and periodic solutions coexist. These islands are identified by giving two types of initial conditions, which are implemented by switching on the feedback process at two points in time - first one at the beginning of operation the of the laser and the second one after the laser has settled to the fixed point.

Chapter 3: In this chapter we analyze the chaotic output of a Quantum Dot Laser with optical feedback using statistical and information theoretical tools. The delay involved in feedback process is retrieved using these techniques. The model of the Quantum Dot Laser and the parameter values are adopted from literature. The output intensity series is analyzed using Auto Correlation Function, Delayed Mutual Information, Permutation Entropy and Permutation Statistical Complexity. These quantifiers are defined and explained before presenting the results. Dynamics of Quantum Dot Laser is simulated for different values of feedback rates and delays. The quantifiers are calculated from the output intensity time

series of the laser. We study how these measures behave when feedback rate or delay are varied. Permutation Entropy and Permutation Statistical Complexity are calculated for different dimensionality of reconstruction of the time series. Indications of delay feedback mechanism and relaxation oscillations are identified from the plots. We find that Permutation Statistical Complexity give the most reliable estimation of the delay due to its distinctive maximum near the delay value.

Chapter 4: From a general point of view the problem we pursue in this chapter can be summarized as follows : How the processes that occur in different time scales and constitute a complex dynamics can be understood, resolved and differentiated from the time series of an observable of the system. The system under consideration is semiconductor laser with optical feedback and current modulation, which we simulate using the well known Lang-Kobayashi model. In addition to the quantifiers used in the previous chapter, we also compute the spectra of the time series to find the indications of the component processes in the system dynamics. All the measures are first computed on the time series which is obtained without the bias current modulation. Features are least resolved in Auto Correlation Function but the spectra and Statistical Complexity give indications of relaxation oscillation and delay feedback. When the computations are repeated for intensity time series with bias current modulation, interesting results are observed. In Entropy and Complexity plots the modulation and the delay feedback are reflected in different ways and are well resolved even when they occur in similar time scales. The nature of the spectra depend on many factors like modulation frequency, modulation strength and bias current. All these measures compared for different operating conditions and we show that to get a clear picture it is necessary to inspect the features reflected in more than one of these quantifiers.

Chapter 5: This chapter summarize the important findings in the thesis. Also some of the future work directions are discussed.

LIST OF PUBLICATIONS

JOURNAL PUBLICATIONS

- *Analysis and Simulation of Semiconductor Laser Dynamics with Optoelectronic Delay Feedback.* Bejoy Varghese, S. Rajesh, V.M. Nandakumaran. **Turk J Phys** Vol.39 pages:60-68 2015
- *Delay signatures in the chaotic intensity output of a Quantum Dot Laser with optical feedback.* Bejoy Varghese, Manu P. John, V.M. Nandakumaran. *Accepted in **Pramana***

CONFERENCE PUBLICATIONS

- *Generalized Bistability in the Nonlinear Dynamics of Delayed Bidirectionally coupled Semiconductor Lasers.* B.Varghese, B.K.Goswami, K.DasGupta, V.M.Nandakumaran. *Photonics 2010 : International Conference on Fiber Optics and Photonics, December 11-15, IIT Guwahati.*
- *Control of Chaos in Current Modulated Multiple-Quantum-Well Lasers with Optoelectronic Delay Feedback.* Bejoy Varghese, Manu P. John, Jijo P. U., V.M.Nandakumaran. *International Conference on Fibre Optics and Photonics. December 9-12, 2012, IIT Chennai, India*
- *A Metal Diaphragm Based Fiber Optic EFPI Temperature Sensor.* P P Anish, J Linesh, T M Libish, Bejoy Varghese and P. Radhakrishnan *DAE-BRNS National Laser Symposium (NLS -19) December 2010, Raja Ramanna Centre for Advanced Technology, Indore.*

CONTENTS

1	Introduction	2
1.1	Semiconductor Lasers	3
1.1.1	Nonlinearities in Semiconductor Lasers	8
1.1.2	Quantum Well and Quantum Dot Lasers	10
1.1.3	Modeling of semiconductor laser dynamics	11
1.2	Delay dynamical systems	12
1.2.1	Ikeda system	13
1.2.2	Mackey-Glass system.	14
1.2.3	Kaldor-Kalecki business cycle.	15
1.3	Numerical Solution of Delay Differential Equations	15
1.3.1	Solving ODEs	16
1.3.2	Solving DDEs	18
1.3.3	Explicit RK methods for DDEs	19
1.3.4	Semiconductor laser with delayed feedback	21
1.4	Hopf Bifurcation.	22
1.5	Thesis Outline	25
2	Analysis and Simulation of semiconductor laser dynamics with optoelectronic delay feedback	26
2.1	Semiconductor Laser Model.	27
2.2	Linear stability analysis of scalar DDEs	33
2.3	Stability Analysis of SCL Rate Equations with optoelectronic feedback	36

2.4	Simulation and Results	39
2.4.1	Effect of nonlinear gain reduction factor	41
2.4.2	Effect of Bias Current	43
2.4.3	Effect of initial condition	44
2.5	Conclusions	45
3	Delay signatures in the dynamics of QDL with optical feedback	46
3.1	Quantum Dot Laser Model	48
3.2	Auto Correlation Function	51
3.3	Bandt and Pompe Symbolization method	52
3.4	Permutation Entropy	55
3.5	Delayed Mutual Information	56
3.6	Permutation Statistical Complexity	57
3.7	Numerical Simulations	59
3.8	Conclusions	64
4	Identifying the components in the delay dynamics of current modulated semi-conductor lasers	66
4.1	Semiconductor Laser with Optical Feedback : Lang-Kobayashi Model	68
4.2	Simulation and Results	70
4.2.1	Comparison of the quantifiers for Lang-Kobayashi Model	70
4.2.2	Effects of current modulation.	76
4.3	conclusions.	83
5	Summary	86
	Bibliography	90
A	Publications	100

1

INTRODUCTION

The work presented in this thesis brings together two exciting and independently established research fields - theory of semiconductor lasers (SCLs) and delay dynamical systems. Semiconductor lasers occupy a central role in today's scientific and technological advancements, and they get more than 50% of the total share in the laser market [1, 2]. SCLs meet industry requirements like compactness, long operational time, wavelength tunability, high modulation bandwidth etc. better than any other laser system. They have applications ranging from DVD players to communication systems, optical pumping of other lasers and material processing etc. which are only a few to mention. Theoretical modeling of semiconductor lasers mostly preceded experimental realizations and are very important from a technological point of view and also due to the underlying physics. Delayed interactions inevitably exist in many natural and artificial environments around us as laws of physics prevent information exchange happening at infinite speed. All systems, natural or artificial, exchange information with the surroundings in some way or other. In most cases these information exchanges can be represented as some form of coupling or feedback mechanism. To exactly model and predict the phenomena observed in such systems, it is necessary to take into account the delay involved in the feedback or coupling process. Delay systems

are capable of showing very complex behavior. When delayed interactions are incorporated into SCL dynamics by introducing feedback or coupling with other SCLs, a multitude of complex dynamical phenomena such as self pulsations[3], chaos[4], hyperchaos[5, 6], and different types of synchronizations[7, 8] have been observed. Interplay between delay and the nonlinearities present in the laser active medium underlies the complexity of the dynamics shown by such systems. Many of these observed phenomena had important technological applications and also they provide new insight into the basic physics of SCLs.

1.1. SEMICONDUCTOR LASERS

The first semiconductor laser was demonstrated by Robert N. Hall and co-workers from General Electric in 1962[9]. It was a Gallium Arsenide (GaAs) semiconductor diode emitting at 850nm. Their invention soon followed by many other groups demonstrating stimulated light emission from semiconductor diodes [10, 11]. In the most simple and primitive form semiconductor laser can be thought of as a forward biased p-n homojunction diode. The p and n regions are heavily doped and since its a homojunction, both regions are of the same semiconductor host. When the diode is not biased the n side has the Fermi Level (E_F) in the conduction band and the p side has E_F in the valence band. Carrier recombination across the junction causes the formation of a thin depletion region in the middle where no free carriers are present. A built-in potential is formed across this depletion region and this potential prevents further recombination of carriers across the junction. A schematic of the unbiased p-n junction is shown in Fig. 1.1. When the diode is forward biased both the width of the depletion region and the potential barrier reduce, and electrons and holes flow more freely across the junction. As a result, carriers of both type will concentrate in the depletion region causing population inversion. Recombination of these carriers result in the emission of photons. Cleaved facets on both sides of the crystal form the end mirrors required for the laser cavity. The cavities thus formed had typical lengths about 200-400 μm [1]. The p-n homojunction lasers suffered from two major drawbacks - (1) it was difficult to produce high carrier densities in the active region which resulted in

low efficiency for light generation. (2) Loss of light due to imperfect reflection from the end facets of the diode resulted in poor optical confinement. In short they failed to efficiently confine the carriers and the field in the active region. As a result threshold current density (J_{th}) for room temperature operation of the laser was very high ($\geq 5 \times 10^4 A/cm^2$). Initially reliable operation of the homojunction laser diodes, required liquid nitrogen temperatures and they had to be operated in pulsed mode. Fig 1.1 depict the band structure of a homojunction laser with no bias and when voltage is applied.

Room temperature continuous wave operation of SCLs were made possible by the introduction of heterostructures in laser diodes[12–14] in 1970s. This was made possible by technological advancements in semiconductor growth processes[2, 14]. Threshold current density and temperature requirements were greatly reduced for such lasers. Heterostructure is the union of two semiconductor materials having different energy gaps, causing a discontinuity in the resulting energy band. In Double Heterostructure SCLs (DHSCs), it was able to bring down the thickness of the active layer to less than $1\mu m$, which accompanied further reduction in threshold current[1]. A commonly used architecture for DHSC consist of GaAs and $Al_xGa_{1-x}As$ as shown in Fig. 1.2. Basic structure consists of a thin layer of GaAs sandwiched between a heavily p doped $Al_xGa_{1-x}As$ and heavily n doped $Al_xGa_{1-x}As$ layers. The middle GaAs layer has a smaller bandgap compared to the outer cladding layers. Fig. 1.3 detail the energy band diagram, carrier confinement and optical confinement in DHSC at high forward bias. Electrons and holes injected into the active region under forward bias, cannot easily cross over to the other side due to the potential barrier from the bandgap difference. Thus there is a substantial build up of carrier population in the active region, which produce the required optical gain for laser operation 1.3b. The active layer with a smaller band gap has a higher refractive index, compared to the outer layers. This effect the active layer to function as a dielectric waveguide. The rays traveling nearly parallel to the interface are guided through the active region due to total internal reflection. Since the cladding layers have a higher bandgap, the fraction of the guided mode outside the active region in not absorbed in DHSC. All these features of DHSC combined to achieve reliable room temperature laser operation, with required

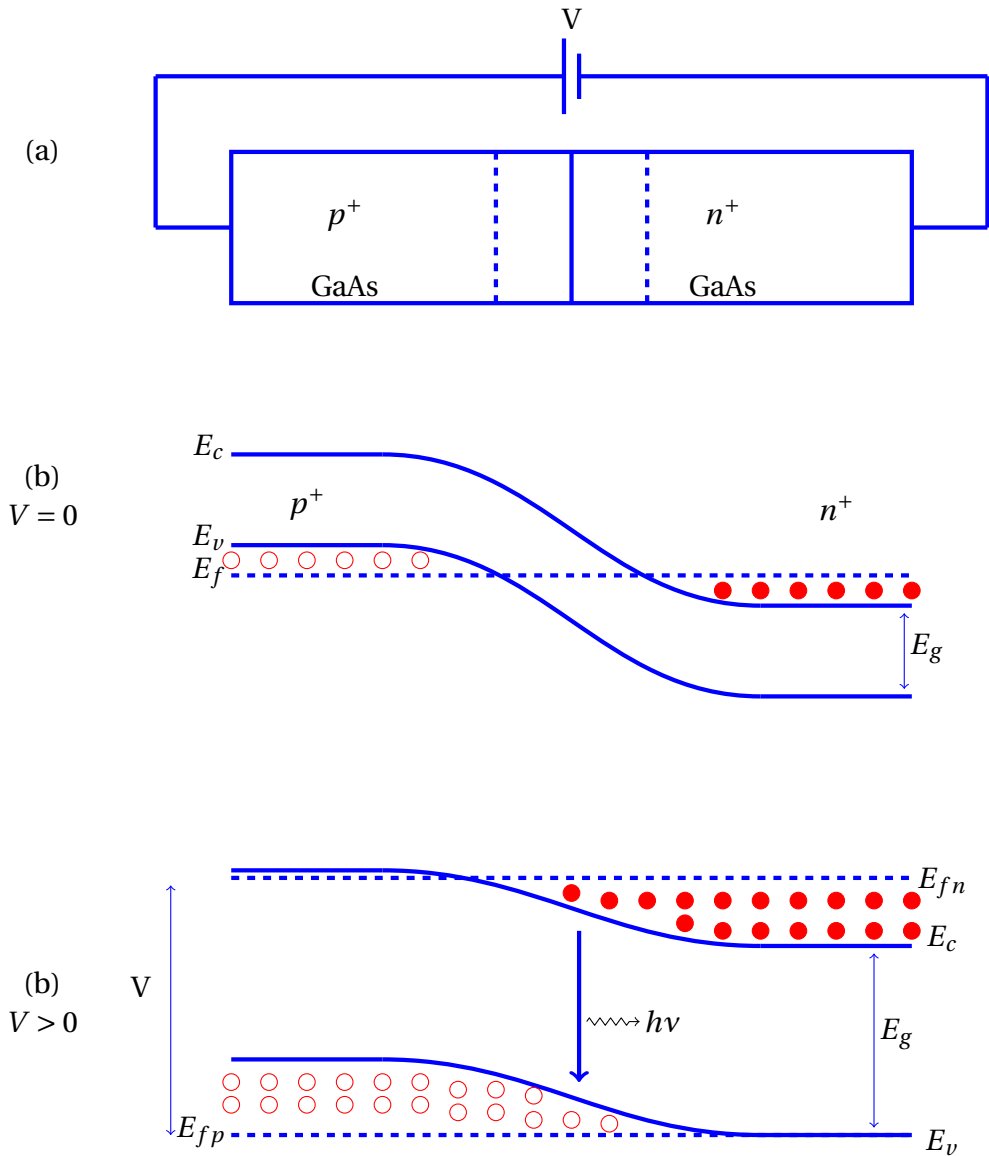


Figure 1.1: (a)schematic of a forward biased homojunction laser (b)homojunction laser under no bias (c)homojunction laser under forward bias. $E_c, E_v, E_f, E_{fp}, E_{fn}$ represent conduction band edge, valence band edge, Fermi level, Fermi level for holes and Fermi level for electrons respectively.

current densities reduced to about $1 \pm 0.5 \times 10^3 A/cm^2$ at 300K[12, 15].

In a semiconductor material energy levels of individual atoms form into a band structure. This band structure is characterized by the wave vector of the electrons k . Semiconductor materials can be classified into two groups based on their bandstructure - direct transition and indirect transition materials. In direct transition semiconductor materials the minimum energy in the conduction band and the maximum energy in the valence band

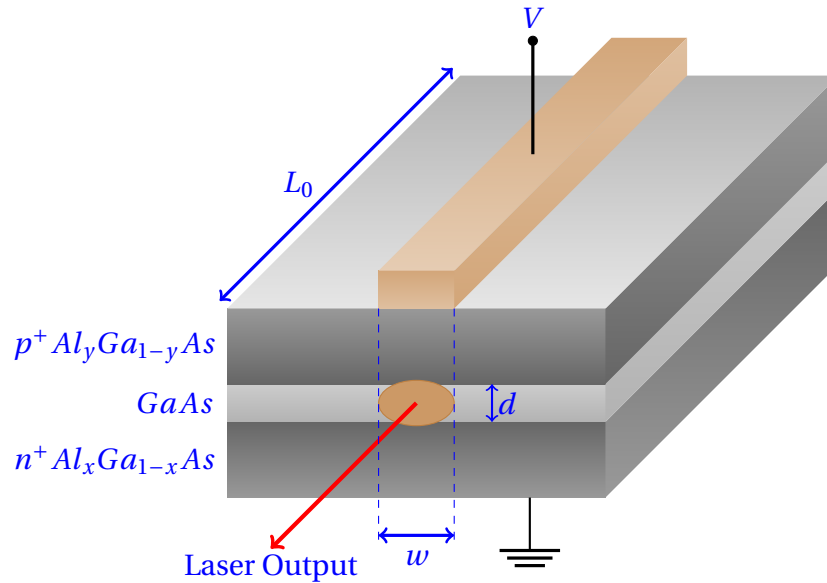


Figure 1.2: Schematic of a $GaAs - Al_xGa_{1-x}As$ double heterojunction semiconductor laser.

occur at the same value of k . If these extrema occur at different values of k , then the material is of the indirect transition type. A schematic of these two types of semiconductors is shown in Fig. 1.4. Since the extrema of the conduction and valence bands does not coincide in indirect transition material, to effect a transition between the bands an electron should emit a phonon to conserve momentum. Thus a two step process is required for this transition, and this reduces the transition probability in such semiconductors. So they are not suited for the active media of lasers. On the other hand, direct band gap materials the transition from conduction to valence band is straight forward. GaN, GaAs and InP are examples of direct bandgap materials [15]. Also there are complex compound materials such as $Al_xGa_{1-x}As$ which can be made either type by tailoring composition[15].

Nonradiative processes occurring in SCLs affect device performance by reducing efficiency and carrier life time [16, 17]. As name suggest, these processes do not include photon emission so do not contribute to the optical field in the laser cavity. Nonradiative recombination occurring in semiconductor lasers are primarily due to two different processes[15]. One is due to the presence of recombination sites or defects in the semiconductor material and the second one is the Auger recombination. In Auger process the energy released in electron-hole recombination is transferred to another electron or hole,

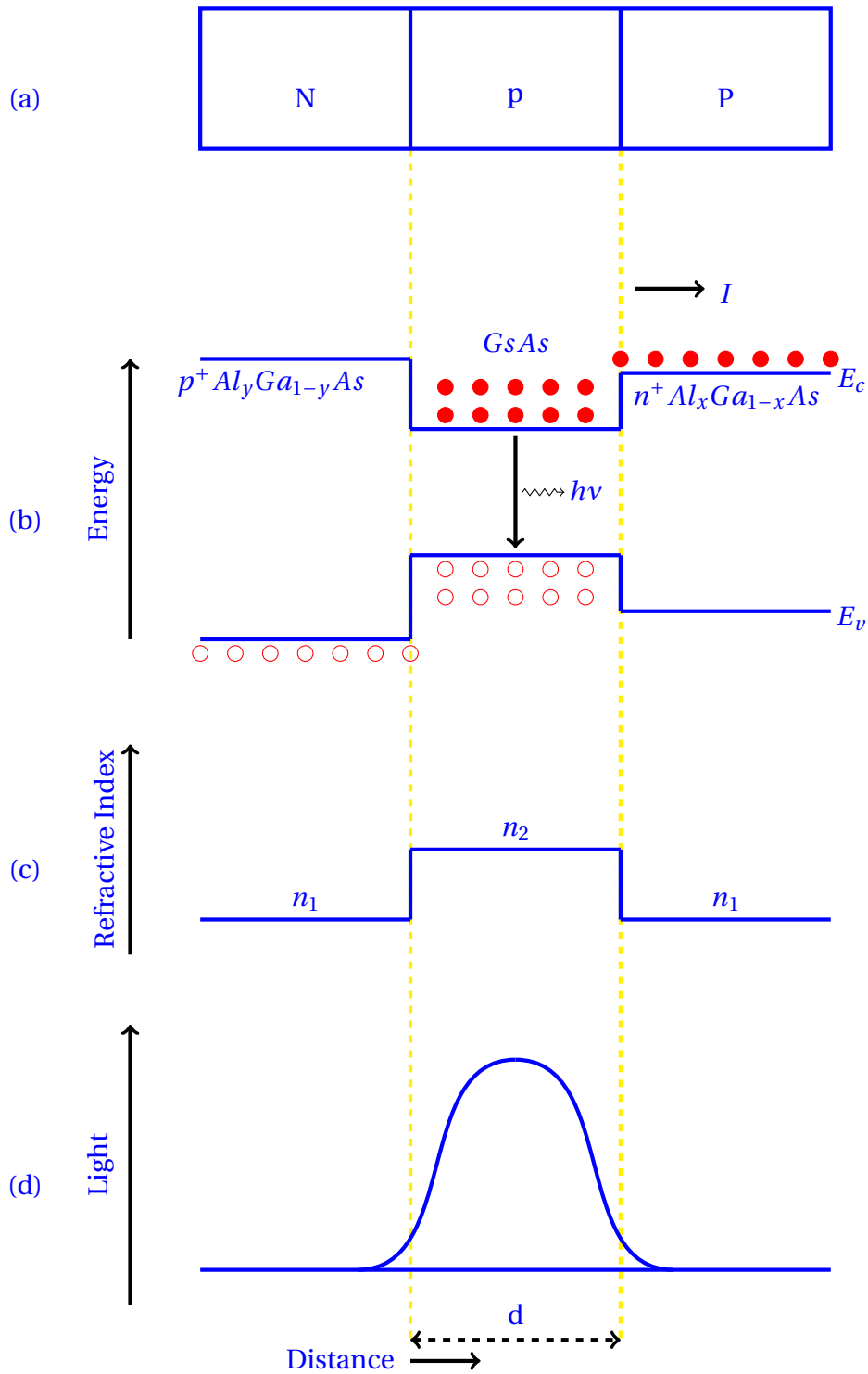


Figure 1.3: (a) Schematic of a DHSEL with an active GaAs layer surrounded by heavily p-doped $pAl_yGa_{1-y}As$ layer and heavily n-doped $Al_xGa_{1-x}As$ layers. (b) Simplified energy band diagram of the laser at high forward bias. Solid and open circles represent electrons and holes respectively. (c) Refractive index profile (d) Optical field distribution

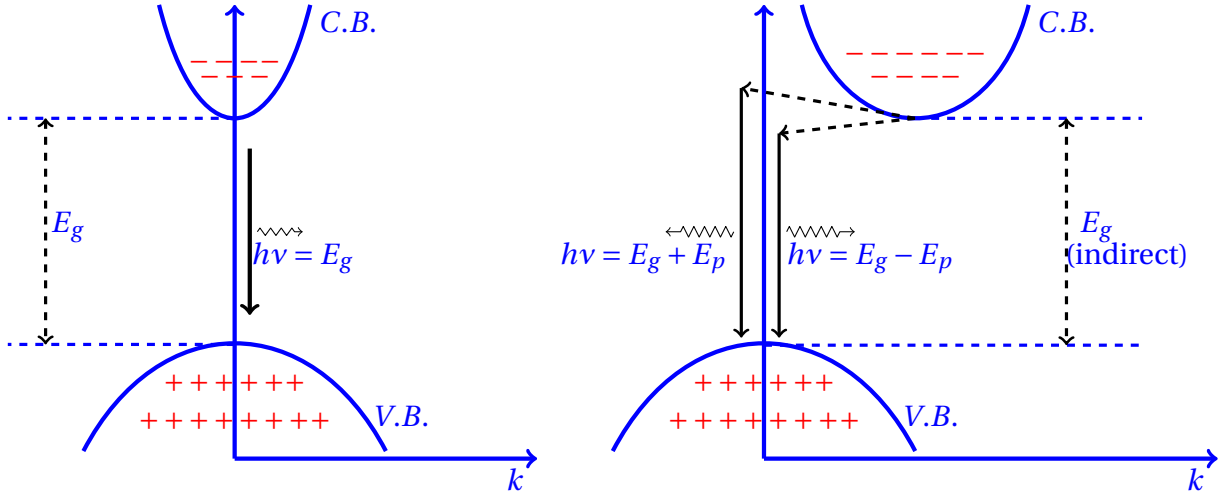


Figure 1.4: Electron-hole recombination in (a) direct and (b) indirect band gap semiconductors. C.B. and V.B. represent the conduction band edge and the valence band edge respectively. '-' denotes electron and '+' denotes holes. Since phonon is involved to conserve momentum in the band-to-band transition in indirect bandgap material, the energy of the emitted photon is either smaller or larger than the bandgap energy (E_g). The difference will be equal to E_p , the energy of the participating phonon.

then they get excited without moving to another band and subsequently relaxes to the lower energy state by emitting phonons. Both Auger recombination and recombination with defects are random events as in spontaneous emission. But no photons are emitted during these processes. So the total recombination rate get contributions from three processes - recombination with defects, radiative recombination which is also termed as bimolecular recombination and Auger recombination. The total recombination can be expressed as

$$R = A_{nr}n + B_{rad}n^2 + C_{Aug}n^3 \quad (1.1)$$

A_{nr}, B_{rad}, C_{Aug} are respectively the defect and surface recombination coefficient, radiative recombination coefficient and Auger recombination coefficient. n is the carrier density.

1.1.1. NONLINEARITIES IN SEMICONDUCTOR LASERS

There are different sources of origin for the nonlinearities in semiconductor lasers[15]. Nonlinear amplitude-phase coupling of the electric field is strong in SCLs compared to

other laser systems [18, 19]. This result from the carrier-induced variation of real and imaginary parts of the semiconductor material's susceptibility $\chi(n) = \chi_r(n) + i\chi_i(n)$. Amplitude-phase coupling is described by the linewidth enhancement factor (α). It is defined as the ratio of the rate of changes in the real and imaginary parts of the susceptibility (χ_r & χ_i), with respect to the carrier concentration, given as

$$\alpha = \frac{d[\chi_r(n)]/dn}{d[\chi_i(n)]/dn} \quad (1.2)$$

α is a key factor in determining many of the laser's characteristics like modulation response, frequency chirp and optical feedback effects[20]. The first calculation of laser linewidth ($\delta\nu$) is by Schawlow and Townes, but their formula was valid only below threshold conditions. This was later modified to account for the stabilization of amplitude fluctuations above threshold and was found to be correct in gas lasers[19, 21]. But for semiconductor lasers the linewidth is enhanced by a factor $1 + \alpha^2$, due to the strong amplitude-phase coupling. The formula for linewidth for SCLs is given by [19, 20]

$$\delta\nu = \frac{v_g^2 h\nu g \alpha_m \beta_{sp} (1 + \alpha^2)}{8\pi P} \quad (1.3)$$

Here v_g is the group velocity, $h\nu$ is the lasing energy, g is the modal gain, α_m is the mirror loss, β_{sp} is the spontaneous emission factor and P is the output power of the laser. α parameter is not constant for a given laser, but depends on factors like carrier density and the detuning of the laser frequency from the gain maximum[18]. Thermal effects are another source of nonlinearity in semiconductor lasers. As the temperature increases, the bandgap energy decreases and the carrier distribution becomes broad. This results in the reduction in gain and increase in refractive index, close to the wavelength of maximum gain. Non-equilibrium carrier distribution in the bands such as spectral hole burning and carrier heating effects also contribute to the nonlinearities. Spectral hole burning is the slight reduction occurring in gain, around the spectral region of the lasing wavelength. Stimulated emission depletes carriers in the active region near to the lasing wavelength. Due to the finite intraband relaxation time of carriers, they are refilled at a lower rate than

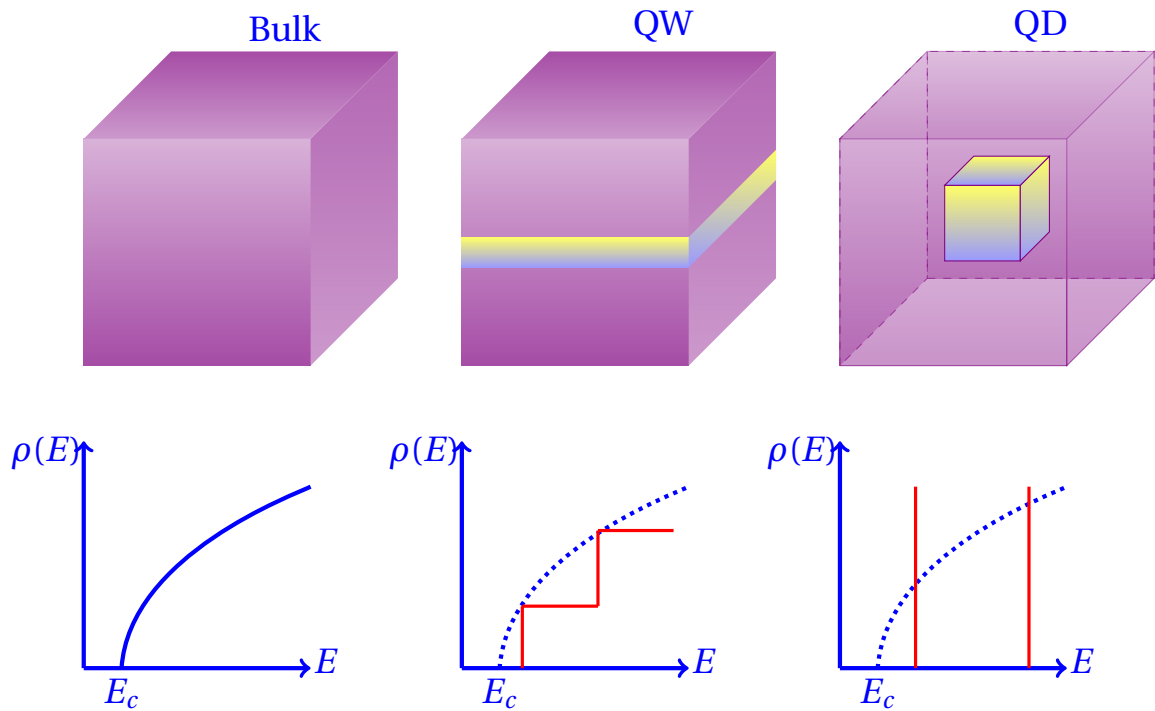


Figure 1.5: Simple picture of density of states $\rho(E)$ for bulk semiconductor materials, Quantum Wells and Quantum Dots

the depletion process, which make 'holes' in the spectral gain. Carrier heating result from stimulated emission and free carrier absorption. Since the active layer gain is sensitive to carrier temperature, carrier heating reduces gain.

1.1.2. QUANTUM WELL AND QUANTUM DOT LASERS

The use of low dimensional structures like Quantum Wells(QW), Quantum Wires or Quantum Dots(QD) can enhance the performance of lasers in different ways[22]. These enhancements include extreme temperature insensitivity, low power consumption, high temperature stability, wavelength tunability, high speed modulation capabilities etc[22, 23]. To observe the effects of quantum confinement, the carriers need to be restricted to regions of size comparable to the deBroglie wavelength of carriers. Taking into account the typical effective mass of electrons and operating temperatures, this length scale turn out to be few nanometers. In a double heterostructure, if the thickness of the middle layer is made to this length scale, it acts as a quantum well, and the electrons form standing wave patterns with

their energy quantized. Developments in epitaxial methods allow controlled fabrication of QW structures with precision in the atomic scale [22]. Quantum confinement strongly modifies the density of states ($\rho(E)$) of the carriers. $\rho(E)$ can be defined as the number of states per unit volume, per unit energy at any particular energy value E . Change in $\rho(E)$ in low dimensional structures can improve electronic and optical properties of devices. Confinement in one, two and three dimensions result in Quantum Wells, Quantum Wires and Quantum Dots respectively. $\rho(E)$ for bulk semiconductors, Quantum Wells and Quantum Dots are given in Fig. 1.5. $\rho(E)$ is continuous for bulk materials, break down into sub bands in Quantum Wells. As the dimensionality is decreased, compared to the band edge $\rho(E)$ is reduced at higher energies. Thus the number of available states that the carriers can be thermally excited is limited and this result in better thermal stability of the laser. Also, increase of $\rho(E)$ at the band edges enhance the differential gain which in turn enhance the modulation bandwidth. The performance characteristics of Quantum Dot lasers were first published by Arakawa and Sakaki[23]. They showed that if carriers are confined in three dimensions in the laser active region, the temperature dependence of threshold current density is virtually eliminated. In QDs, the sub-band structure give way to discrete states like in atoms, shown as delta functions in Fig.1.5. The separation between these states exceed thermal energy, so the electron-phonon interaction is minimal. This brings down threshold current density (J_{th}) and improve temperature stability.

1.1.3. MODELING OF SEMICONDUCTOR LASER DYNAMICS

The dynamics of SCL is described by a set of rate equations for the carriers and the field in the active region. In the simplest case this consists of two equations - one for the total number of electron-hole pairs and the second equation for the complex amplitude of the electric field[24]. But when more advanced structures like quantum wells and quantum dots are used in the active region this situation can change. For example, for Quantum Dot Lasers(QDL) separate equations are written for the carriers and the field in the QD and for the surrounding QW region[25, 26]. Also different rate equations for electrons and holes are written because the total number of electrons and holes may differ in numbers due to dif-

ferent depths of conduction and valence bands in the QD and the difference in the effective mass of electrons and holes [27]. If one consider many bound states in the QD, transitions between these states still increase the required number of equations. Recent published research works consists of models of QDL with more than two hundred equations[28]. In spite of all these complications excellent simple models exist which can simulate the essential features of the QDL dynamics effectively[29].

1.2. DELAY DYNAMICAL SYSTEMS

Delay dynamical systems are getting more relevance in recent times, as it is recognized that accurate description of many physical phenomena require delayed interactions to be accounted for. One example, frequently quoted is that of El-Nino/Southern Oscillations (ENSO) phenomenon, which is an irregular cycle of coupled ocean temperature and atmospheric pressure oscillations across equatorial pacific[30, 31]. ESNO is an active research topic, as it has effects in global scale. Relatively simple delay differential models can model these irregular oscillations[32], which otherwise require large scale computing resources. The most interesting aspect of delay systems is that its state space is infinite dimensional. To specify the state of a delay system at any instant t_0 , one needs a space of continuous functions on the interval $[t_0 - \tau, t_0]$. Mathematical models describing a delay dynamical system can take several forms depending on the nature of the dynamical system it describes. All these models include the delay parameter in some specified way, which bring the dependence of the present rates of change on the past rates and values of the variables[30]. The models considered in the present work consists of delay differential equations with single constant delay which belongs to the class of retarded functional differential equations[30]. An example for such a system can be given as

$$q_0 \frac{dx(t)}{dt} + q_0 x(t) + q_1 x(t - \tau) = f(t) \quad (1.4)$$

Here q_0 , q_1 and q_2 are arbitrary constants and $f(t)$ is forcing term. Below we discuss some well known examples of delay systems.

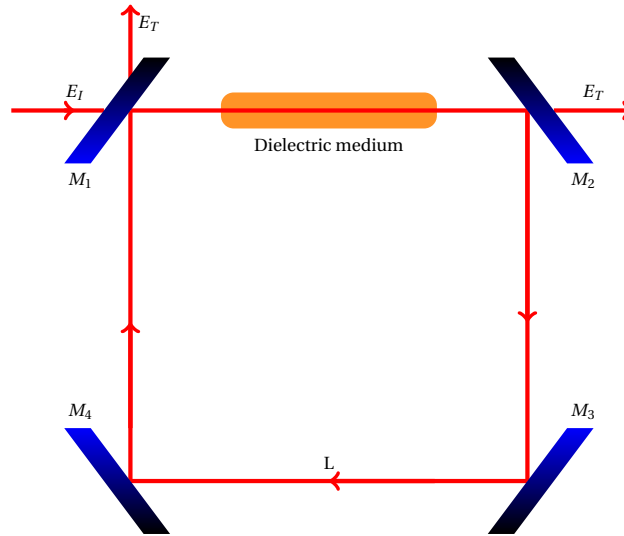


Figure 1.6: Schematic of Ikeda system - a ring cavity containing a nonlinear dielectric medium. M_i are cavity mirrors, E_I is the incident field and E_T is the transmitted field.

1.2.1. IKEDA SYSTEM

The model proposed by Kensuke Ikeda describes the field dynamics in a bistable ring cavity filled with nonlinear dielectric medium[33]. The schematic of the Ikeda system is shown in Fig. 1.6. A nonlinear absorbing medium containing two level atoms is placed in the ring cavity and a constant input intensity is given. For sufficiently large length of the cavity, the optical system undergoes a time delayed feedback. This can introduce behaviors others than steady state output. In the original paper, Ikeda showed that the transmitted intensity from the cavity will undergo a series of transitions from stationary state to periodic and nonstationary states as the input intensity is increased. Ikeda derived a set of delay differential equations to describe the system starting from Maxwell-Bloch equations. They are given by

$$\dot{E}(t) = A + BE(t - t_R) \exp\{i[\varphi(t) - \varphi_0]\} \quad (1.5)$$

$$\gamma_D^{-1} \dot{\varphi}(t) = -\varphi(t) + \text{sgn}(n_2) |E(t - t_R)|^2 \quad (1.6)$$

$E(t)$ is the field at the boundary of the ring cavity where input and feedback lights are

added up. $\varphi(t)$ denotes the phase change occur in the electric field when it passes through the medium. φ_0 is the linear phase shift across the medium. n_2 is the coefficient of the nonlinear refractive index and sgn function extracts the sign of n_2 . A is a parameter proportional to the intensity of the incident field and B characterizes the dissipation of the field in the cavity. t_R is the delay which arises as time taken by the light to traverse the length of the cavity(L). $t_R = L/c$. γ_D is the Debye relaxation rate. If one assume that dissipation is strong (small B) and input intensity is high (large A), but A^2B fixed, the set of equations given above reduce to a scalar Delay Differential Equation (DDE)

$$\gamma_D^{-1}\dot{\varphi}(t) = -\varphi(t) + A^2 [1 + 2\cos(\varphi(t - t_R) - \varphi_0)] \quad (1.7)$$

This equation is known as the Ikeda DDE. Many experimental realizations of Ikeda like systems followed the theoretical work. Bifurcations in optoelectronic bistable systems are reported in [34, 35]. Similar system was demonstrated by Neyer et. al.[36] based on an electro-optical Mach-Zehnder modulator. An acousto-optic system which show similar dynamics is reported by Vallee and Delisle[37]. In all the cases the dynamics of of the system is described by an equation similar to 1.7. Anticipating synchronization in coupled Ikeda systems have been extensively studied and reported in literature[38, 39].

1.2.2. MACKEY-GLASS SYSTEM

This model was proposed by Michael C. Mackey and Leon Glass in 1977 to describe the blood production in patients with Chronic Granulocytic Leukemia(CGL)[40]. This model consist of a delay differential equation with single constant delay. In CGL patients circulating granulocyte numbers can show large amplitude oscillations. The period of the oscillations also show significant deviations. Mackey-Glass equation successfully demonstrate the relation between the time taken for production of the blood cellular components and the oscillation periods. The model is described by the equation[40]

$$\frac{dP}{dt} = \frac{\beta_0 \theta^n}{\theta^n + P_\tau^n} - \gamma P \quad (1.8)$$

Here P is the density of the circulating blood cells and β_0, θ, n and γ are constants.

1.2.3. KALDOR-KALECKI BUSINESS CYCLE

Formally, business cycles can be defined as type of fluctuations found in aggregate economic activity [41]. Kaldor-Kalecki model is a macroeconomic model introduced to describe these business cycles. The Kaldor-Kalecki system of differential equations can be written as[41]

$$\dot{Y}(t) = \alpha [I(Y(t), K(t)) - S(Y(t), K(t))] \quad (1.9)$$

$$\dot{K}(t) = I(Y(t - \tau), K(t - \tau)) - \delta K(t) \quad (1.10)$$

$Y(t)$ denotes real production and $K(t)$ denotes capital at any time t . $S(t)$ is the savings. $I(Y(t), K(t))$ represent investment. α is a constant that represent the speed of adjustments of the goods in the market and δ represent capital depreciation rate. The first term on the R.H.S of the second equation take into account the delay in investment decision and delivery of investment. Time delay induce more complex behavior in the dynamics and these are extensively reported in literature[42, 43].

1.3. NUMERICAL SOLUTION OF DELAY DIFFERENTIAL EQUATIONS

In this section we give numerical methods for solution of DDEs. Most of the existing methods to numerically solve DDEs come as natural extensions of the methods used to solve Ordinary Differential Equations(ODEs)[44]. So we discuss ODE solvers first and then in the next section describe how some of these methods can be used for solving DDEs. Runge-Kutta methods of different orders are most frequently employed to solve ODEs. Euler method, Heun's method etc. turn out to be particular members of Runge-Kutta family.

1.3.1. SOLVING ODES

The discussion in this section is restricted to Explicit Runge-Kutta(RK) methods. This is justified in the next section. General form of ERK method can be expressed as[45, 46]

$$y_{n+1} = y_n + h \sum_{i=1}^s b_i k_i \quad (1.11)$$

where

$$k_1 = f(t_n, y_n)$$

$$k_2 = f(t_n + c_2 h, y_n + h(a_{21} k_1))$$

$$k_3 = f(t_n + c_3 h, y_n + h(a_{31} k_1 + a_{32} k_2))$$

.

.

$$k_s = f(t_n + c_s h, y_n + h(a_{s1} k_1 + a_{s2} k_2 + \dots + a_{s,s-1} k_{s-1}))$$

Any particular explicit RK3 method is completely defined if s, a_{ij} (for $1 \leq j < i \leq s$), b_i ($i = 1, 2, \dots, s$) and c_i (for $i = 2, 3, \dots, s$) are given. s gives the number of stages in the method, b_i and c_i are known as the weights and nodes and the matrix $[a_{ij}]$ is called the Runge-Kutta matrix. All information regarding the RK method can be arranged in what is called Butcher tableau given by.

0					
c_2	a_{21}				
c_3	a_{31}	a_{32}			
.			.		
.				.	
.					.
c_s	a_{s1}	a_{s2}	.	.	$a_{s,s-1}$
	b_1	b_2		b_{s-1}	b_s

EULER METHOD

The simplest method in the RK family is the Euler method. Its tableau is given by

$$\begin{array}{c|c} 0 & \\ \hline & 1 \end{array}$$

Corresponding formula becomes

$$y_{n+1} = y_n + hf(t_n, y_n) \quad (1.12)$$

SECOND ORDER METHOD

Second order method with two stages can be in general represented by tableau

$$\begin{array}{c|cc} 0 & & \\ \alpha & & \alpha \\ \hline & (1 - \frac{1}{2\alpha}) & \frac{1}{2\alpha} \end{array}$$

Here α is a parameter and if its value is 1, we get Heun's method, given by,

$$k_1 = f(t_n, y_n)$$

$$k_2 = f(t_n + h, y_n + h(k_1))$$

$$y_{n+1} = y_n + \frac{h}{2}(k_1 + k_2) \quad (1.13)$$

When the value of α is $\frac{1}{2}$ the method is called the midpoint method.

RK3 METHOD

The tableau for explicit RK3 method is given by

$$\begin{array}{c|cc}
 0 & & \\
 \frac{1}{2} & \frac{1}{2} & \\
 1 & -1 & 2 \\
 \hline
 & \frac{1}{6} & \frac{2}{3} & \frac{1}{6}
 \end{array}$$

The corresponding equations are given by

$$\begin{aligned}
 k_1 &= f(t_n, y_n) \\
 k_2 &= f\left(t_n + \frac{h}{2}, y_n + \frac{h}{2}(k_1)\right) \\
 k_3 &= f(t_n + h, y_n + h(-k_1 + 2k_2))
 \end{aligned}$$

$$y_{n+1} = y_n + \frac{h}{6}(k_1 + 4k_2 + k_3) \quad (1.14)$$

RK4 method is not detailed here because to solve DDEs we use the extended version of either Heun's method or RK3 method.

1.3.2. SOLVING DDEs

The description in this section is restricted to the DDEs of the form

$$\dot{y} = f(t, y(t), y(t - \tau)) \quad (1.15)$$

such that $\tau > 0$ and $y(t) = g(t)$ for $t \leq 0$, which should be given in order to solve the DDE.

In addition we assume that

- Delay is a constant. There can be situations where the value of delay depends on the state of the system or time, but for our work presented in this thesis, this assumption is always valid.
- $h < \tau$, where h is the time step used in integration.

The situations arise in this work always fall into this particular form. As discussed in [44], these assumptions enable the use of explicit RK methods for integration. DDEs can be effectively solved with methods that combine Explicit Runge-Kutta methods and the method of steps. Method of steps is detailed below.

METHOD OF STEPS^[46]

For DDEs of the form 1.15, the solution in the interval $[0, \tau]$ is given by $\phi(t)$, which is the solution of the inhomogeneous initial value problem[46]

$$\dot{\phi} = f(\phi(t), g(t - \tau)) \quad (1.16)$$

where, $\phi(0) = g(0)$. Using the solution in each interval, the DDE can be solved for the next interval by repeating this procedure.

1.3.3. EXPLICIT RK METHODS FOR DDEs

General form of an explicit RK method used to solve DDEs can be represented as[47]

$$y_{n+1} = y_n + h \sum_{j=1}^s b_j f(t_n + c_j h, y_{nj}, y_{n\tau j}) \quad (1.17)$$

where y_{nj} satisfy the relation

$$y_{ni} = y_{n-1} + h \sum_{j=1}^{j<i} a_{i,j} f(t_n + c_j h, y_{nj}, y_{n\tau j}) \quad (1.18)$$

for $i = 1, 2, 3, \dots, s$

The argument $y_{n\tau j}$ denotes approximation to $y(t_n + c_j h - \tau)$ which is obtained by specific polynomial interpolation at $t = t_n + c_j h - \tau$ from the known values of y . Also when $t_n + c_j h - \tau \leq 0$, $y(t - \tau)_{nj} = g(t_n + c_j h - \tau)$, where g is the initial function.

HEUN'S METHOD

According to the discussions given above, Heun's method for DDEs can be written as

$$\begin{aligned}
k_1 &= f(t_n, y_n, y(t_n - \tau)) \\
k_2 &= f(t_n + h, y_n + hk_1, y(t_n - \tau + h))
\end{aligned}$$

Since $y(t_n - \tau + h)$ is in the solution grid, separate interpolation procedure to estimate delay argument is not required for Heun's method. The final approximation formula for y_{n+1} is given as

$$y_{n+1} = y_n + \frac{h}{2} (k_1 + k_2) \quad (1.19)$$

RK3 METHOD

When RK3 method is adopted to solve DDEs, the modified equations for calculating k_i s are given by

$$\begin{aligned}
k_1 &= f(t_n, y_n, y(t_n - \tau)) \\
k_2 &= f\left(t_n + \frac{h}{2}, y_n + \frac{h}{2}k_1, y\left(t_n + \frac{h}{2} - \tau\right)\right) \\
k_3 &= f(t_n + h, y_n + h(-k_1 + 2k_2), y(t_n + h - \tau))
\end{aligned}$$

$y(t_n - \tau)$ and $y(t_n + h - \tau)$ are in the solution grid and should be already known. $y(t_n + \frac{h}{2} - \tau)$ is to be estimated using interpolation[47, 48]. We use Hermite interpolation taking four points in the grid close to $t_n + \frac{h}{2} - \tau$. The approximation formula for y_{n+1} remains the same as in the RK3 method for ODEs.

$$y_{n+1} = y_n + \frac{h}{6} (k_1 + 4k_2 + k_3) \quad (1.20)$$

1.3.4. SEMICONDUCTOR LASER WITH DELAYED FEEDBACK

In this section we give a brief overview of the dynamical behaviors observed in SCLs with delayed feedback. Instabilities in the emission of semiconductor lasers when output light is coupled back to the laser cavity were reported from late 1960s[49]. For many technological applications, where stable operation was essential, this turned out to be a highly undesired feature. Completely eliminating back reflection to the laser cavity from the external environment was a difficult task, so the "intensity noise" or "instabilities" were frequently observed in many semiconductor laser systems[2]. Later it was proposed that these instabilities can be made useful in many ways. The complex emission patterns provide useful information about the internal processes in the laser dynamics[50]. The prospect of using feedback induced intensity modulations in optical communication systems catalyzed intense research on the subject [50–52]. Also, semiconductor laser with feedback provided a laboratory example of a delay system which is capable of exhibiting rich variety of complex phenomena but at the same time can be reliably controlled. Many phenomena, first observed in semiconductor lasers with feedback in laboratory conditions were later discovered in natural systems[2, 53]. By 1970, it was shown that the use of optical feedback can be employed for better selection of longitudinal modes[54], increase in coherence length[54] and intensity self pulsations[3]. The feedback can be given either optically or optoelectronically. Simplified schematics of both these schemes are given in Fig: 1.7. In optical feedback(Fig. 1.7a) a mirror is placed outside the laser cavity which form a external cavity and constitute the feedback mechanism. In optoelectronic feedback scheme(Fig. 1.7b), the laser output is detected using a high bandwidth detector and after required amplification, the detector signal is added with the laser bias current. In 1980, Lang and Kobayashi proposed a model to describe the time evolution of the complex field and carriers in a single mode laser with delayed optical feedback[55]. The model became an immediate success because it accounted for many of the observed phenomena when feedback rate is low or moderate[56]. As discussed in previous sections, delay systems are in principle infinite dimensional and this gives the prospect of high dimensional dynamics and many exciting new phenomena. Interplay between the time delay and nonlinearity is the key aspect in

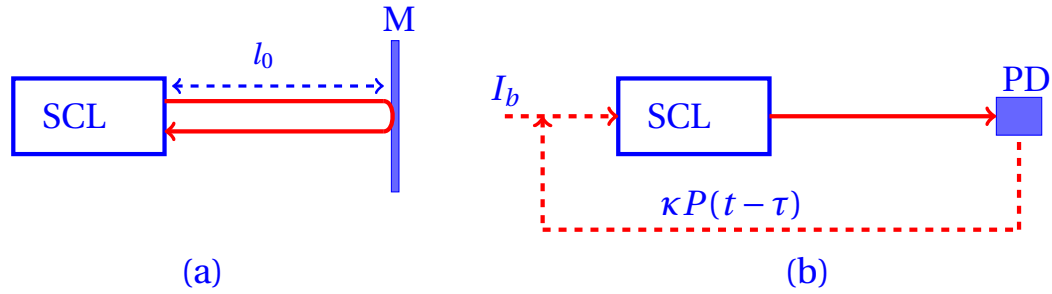


Figure 1.7: Simplified schematic of (a) optical and (b) optoelectronic feedback schemes for semiconductor lasers. In (a) M the mirror that form the external cavity, l_{ec} is the length of the external cavity, τ_d is the time taken by light for round trip in the external cavity and κ is the feedback rate. In (b), I_b is the bias current, PD is the photodetector, κ is the optoelectronic conversion factor and τ_d is delay involved in the optoelectronic feedback process. $P(t)$ denote the output power at any time t .

understanding of the delay dynamics in SCLs[15].

Chaotic behavior observed in SCLs with optical feedback is roughly categorized into two regimes - Low Frequency Fluctuations and Coherence Collapse(CC)[57, 58]. LFFs occur for moderate feedback and near lasing threshold[58, 59]. In LFF the optical power develops sudden dropouts at irregular times and recover over microsecond timescales. This time scale is much larger than other timescales of the SCL like the relaxation oscillation period. As the bias current increases, the average time gap between the power dropouts decreases and eventually they merge to form completely irregular output traces. This is called the Coherence Collapse regime[60]. Optoelectronic feedback scheme has the possibility of bringing any desired optical configuration between the laser and the detector. Chaos is reported extensively with optoelectronic feedback scheme in different types of configurations [52, 61, 62]. Also positive and negative feedback schemes and its many variations are investigated and found show interesting features[63, 64].

1.4. HOPF BIFURCATION

Bifurcations are sudden qualitative changes in the nature of motion, as some control parameters cross critical values. To understand these bifurcations, local stability of the solution in the phase space of the system near the critical value of the control parameter is to be studied. Some of the simple bifurcations, often encountered in low dimensional contin-

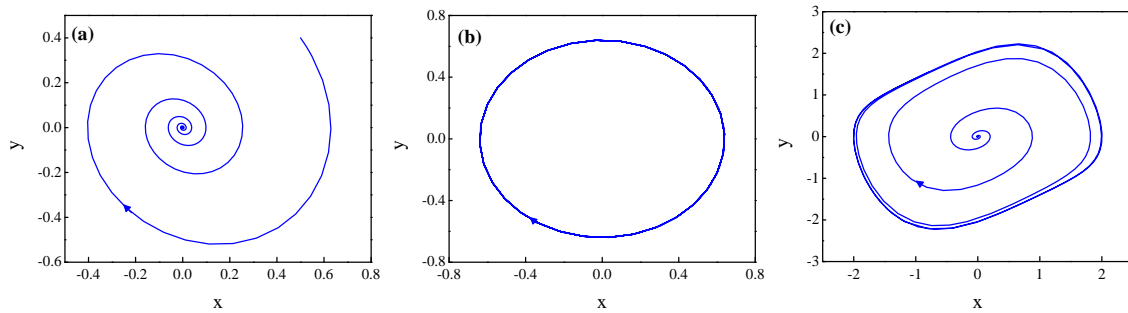


Figure 1.8: Phase space trajectories of van der Pol oscillator for (a) $b=-0.3$ (b) $b=0$ and (c) $c=0.5$. In (a) the equilibrium point is a stable focus, in (b) equilibrium point is of center type, in (c) equilibrium point is an unstable focus.

uous dynamical systems are

- saddle node bifurcation
- pitchfork bifurcation
- transcritical bifurcation
- Hopf bifurcation

Extensive literature exist on these bifurcations and the underlying mechanisms. Here we detail only the Hopf bifurcation, since we observe Hopf bifurcation in semiconductor laser when optoelectronic feedback is given, which is discussed in chapter 2. In Hopf bifurcation, at the critical value of control parameter, an equilibrium point loses its stability and a limit cycle is born[65]. Hopf bifurcation is characterized by a change of the real parts of the pair of complex conjugate eigen values associated with an equilibrium point from a negative to positive value while the imaginary part remains greater than zero [66].

EXAMPLE : VAN DER POL OSCILLATOR

van der Pol model describes the dynamics of a circuit with a triode valve, where the resistance of the valve changes with current. The model is described by a set of equations given below[66].

$$\dot{x} = y \tag{1.21}$$

$$\dot{y} = \mu(1 - x^2)y - x \quad (1.22)$$

μ is the damping constant. The equilibrium point of the system is the origin $(0, 0)$. The characteristic equation of the system is

$$\lambda^2 - \mu(1 - x^2)\lambda + 2\mu xy + 1 = 0 \quad (1.23)$$

At the equilibrium point $(0, 0)$, the eigen values are obtained as

$$\lambda = \frac{1}{2} \left\{ \mu \pm \sqrt{\mu^2 - 4} \right\} \quad (1.24)$$

When $-2 < \mu < 0$, the eigen values are complex conjugate with negative real parts. This means the equilibrium point is stable and the trajectories starting in the neighborhood of the equilibrium point will wind around and asymptotically reach it. Such type of equilibrium point is called stable focus. At $\mu = 0$, the eigen values become $\lambda = \pm i$. Also the van der Pol equations reduces to that of simple harmonic motion and the solutions turn to periodic orbits. Now, the equilibrium point is said to be center type. For $0 < \mu < 2$, the eigen values are complex conjugates with their real part positive. Now $(0, 0)$ is an unstable focus, meaning the trajectories starting near the neighborhood of the equilibrium point spiral away from it. The fate of the the diverging trajectories can be found by calculating the quantity[67]

$$\nabla.F = \frac{\partial f_1}{\partial x} + \frac{\partial f_2}{\partial y} \quad (1.25)$$

For van der Pol equations

$$\nabla.F = \mu(1 - x^2) \quad (1.26)$$

From the above equation it can be seen that $\nabla.F$ is positive for $|x| < 1$ and negative for $|x| > 1$. This means for $|x| < 1$ damping is positive and $|x| > 1$ damping is negative. Because of the balance between positive and negative damping, there exist a closed orbit, which

turn out to be a stable limit cycle. This type of bifurcation is called Hopf bifurcation. Hopf bifurcations can be of two types **supercritical** and **subcritical**[65]. The example above is a supercritical Hopf bifurcation, because the limit cycle is stable above bifurcation point. In the case of a subcritical Hopf bifurcation the limit cycle will be unstable.

1.5. THESIS OUTLINE

This thesis is organized in the following way.

Second chapter report our work on linear stability analysis and Hopf bifurcation in semiconductor lasers with optoelectronic delay feedback. The theoretical model of the laser and necessary mathematics for the linear stability analysis of delay differential equations are provided before we present the results. Effects of delay, feedback rate, bias current and nonlinear gain reduction factor on the stability of the steady state operation and on Hopf bifurcation are studied.

Chapter 3 present the delay estimation from chaotic output of a quantum dot laser with optical feedback. Techniques like Correlation Functions, Mutual Information, Permutation Entropy and Permutation Statistical Complexity are used for the estimation. A detailed comparison of these methods is given for a range of feedback strengths and delays.

The results presented in Chapter 4 are related to distinguishing and resolving component processes of the complex semiconductor laser dynamics in the presence of current modulation and delayed optical feedback. In addition to the techniques used in the previous chapter, Fourier spectra of the chaotic output are also calculated to see how well these techniques differentiate the processes like delayed feedback, current modulation and relaxation oscillations.

The work discussed in the previous chapters are summarized in Chapter 5.

2

ANALYSIS AND SIMULATION OF SEMICONDUCTOR LASER DYNAMICS WITH OPTOELECTRONIC DELAY FEEDBACK

Semiconductor lasers (SCL) with delayed feedback have been investigated extensively in recent years, due to the rich variety of nonlinear phenomena they exhibit and also because of their potential applications [2]. They show many interesting phenomena such as low and high dimensional chaos [4], local and global bifurcations [68], control [7] and synchronization of chaos [8, 69], intensity instabilities [70], multistability and hysteresis [71], and stochastic resonance effects [72, 73]. Incorporation of time delay into the system makes it infinite dimensional and consequently the system can exhibit very complex dynamics. Many aspects of delay dynamics have been observed and studied first in laser systems [2, 30]. These nonlinear effects in semiconductor lasers have novel technological applications like secure information encryption [56, 72], chaotic lidar [74] etc. Modification of laser dynamics with feedback depends on many factors such as type and strength of feedback, delay time involved in the feedback mechanism, bias current and other pa-

rameters like gain nonlinearities. Feedback mechanism can be either optical [75, 76] or optoelectronic [70, 77]. In optical feedback, a part of the output laser field is injected back into the laser cavity. The optoelectronic feedback technique involves a high bandwidth photodetector for optoelectronic conversion of the laser output and the injection of a suitably amplified detector signal into the pumping current of the SCL. Even when the nonlinear gain reduction is strong enough to inhibit period doubling and chaos in current modulated semiconductor lasers [24], delay feedback has been proved to induce bifurcations and chaos [62]. Destabilization of the fixed point by Hopf bifurcation in SCL with optoelectronic feedback has been reported in many works [76, 77]. Given such considerations, it is of utmost importance for the system designer to know how the SCL stability varies with feedback and changes with different parameters. In this work, we analyse the delay differential equations of the SCL with optoelectronic delay feedback to study the of Hopf bifurcation phenomena in the feedback strength-delay parameter space and its dependence on nonlinear gain reduction factor, bias current and initial conditions. The effect of initial condition on the dynamics is studied by switching on the delay mechanism at different stages in the operation of the laser.

2.1. SEMICONDUCTOR LASER MODEL

In this section we give an outline of how the SCL rate equations can be derived from basic principles. A detailed derivation of the same can be found in [78]. A schematic model of the laser cavity is given in Fig. 2.1. The laser is modeled as a Fabry-Perot cavity with the active medium between the two end reflectors. The cavity has the length L and the reflectivities of the end reflectors are represented by R_1 and R_2 respectively. Amplitude of the forward and backward traveling complex electric field are represented respectively as

$$E_f(z) = E_f(z=0) \exp \left[-i \frac{\eta\omega}{c} z + \frac{1}{2} (gz - \alpha_s z) \right] \quad (2.1)$$

$$E_b(z) = E_b(z=L) \exp \left[-i \frac{\eta\omega}{c} (L-z) + \frac{1}{2} (g(L-z) - \alpha_s (L-z)) \right] \quad (2.2)$$

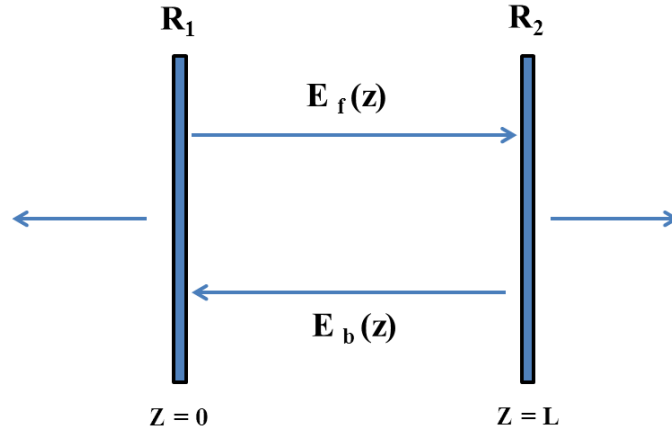


Figure 2.1: Schematic of laser cavity of length L along the z axis. R_1 and R_2 are the reflectivities of the faces and $E_{f,b}(z)$ represent the complex amplitude of the electric field traveling in the forward and the backward directions respectively.

where η is the real part of the refractive index, ω is the angular frequency, c is the velocity of light, g is the gain due to stimulated emission, α_s takes into account all the optical losses inside the cavity that does not result in the generation of carriers inside the active region. Defining r_1 and r_2 as the reflection coefficients at the end mirrors such that $|r_1|^2 = R_1$ and $|r_2|^2 = R_2$, it can be shown that

$$E_f(z=0) = E_f(z=L) r_1 r_2 \exp \left[-\frac{2i\eta\omega L}{c} + (g - \alpha_s)L \right]$$

From the above equation we can deduce the the round trip gain G and the condition for sustained laser oscillation as

$$G = r_1 r_2 \exp \left[\frac{-2i\eta\omega L}{c} + (g - \alpha_s)L \right] = 1 \quad (2.3)$$

The modulus of equation 2.3 gives the threshold gain g_{th}

$$g_{th} = \alpha_s + \frac{1}{2L} \ln \left(\frac{1}{R_1 R_2} \right) \quad (2.4)$$

At laser threshold the total gain inside the cavity just balances the total losses. The resonance angular frequency of the m^{th} mode at threshold can be written as

$$\omega_{m,th} = m \frac{\pi c}{\eta(\omega_{m,th}, N_{th}) L} \quad (2.5)$$

N_{th} is the carrier number at threshold. In the following discussions $\omega_{m,th}$ is represented as ω_m and $\eta(\omega_{m,th}, N_{th})$ as η_{th} . Frequency dependence of g , α_s , r_1 and r_2 can be neglected for frequencies close to the frequency of the laser mode under consideration. Expanding $\eta\omega/c$ in terms of the optical angular frequency and the carrier number (N) at the threshold, and substituting in the expression for G , we get

$$G = \exp \left[(g - \alpha_s)L + \frac{1}{2} \ln(R_1 R_2) - 2i \frac{\omega_{th} L}{c} \frac{\partial n}{\partial N} \Big|_{th} (N - N_{th}) \right] \exp \left[-2i \frac{\eta_{th} \omega_{th} L}{c} - 2i \frac{\eta_g L}{c} (\omega - \omega_{th}) \right] \quad (2.6)$$

where η_g is the group refractive index given by $\eta + \omega \frac{d\eta}{d\omega}$. The first exponential is independent of frequency and the second exponential is dependent on frequency. So the total round trip gain can be written as the product of frequency independent and frequency dependent parts.

$$G = G_1 G_\omega \quad (2.7)$$

To get the time evolution of electric field the round trip gain is to be applied to the time independent electric field E_f of the forward traveling wave at $z = 0$. The resultant equation is

$$E_f(t) = G E_f(t) = G_1 \exp(i\omega_{th} \tau_{in}) \exp \left(-\tau_{in} \frac{d}{dt} \right) E_f(t) \quad (2.8)$$

τ_{in} is the round trip time of light inside the cavity and $\exp \left(-\tau_{in} \frac{d}{dt} \right)$ is the shift operator which introduces time shift of $-\tau_{in}$ to the electric field. Introducing slowly varying complex amplitude $E(t)$

$$E_f(t) = E(t) \exp(i\omega_{th} t) \quad (2.9)$$

and assuming that the variation of $E(t)$ is small in one round trip time, it can be written

$$\frac{dE}{dt} = \frac{1}{\tau_{in}} \left(1 - \frac{1}{G_1} \right) E(t) \quad (2.10)$$

After some simplifications 2.10 becomes

$$\frac{dE(t)}{dt} = \left[\frac{c}{2\eta_g} \frac{\partial g}{\partial N} \Big|_{th} (N - N_{th}) - i \frac{\omega_{th}}{\eta_g} \frac{\partial n}{\partial N} \Big|_{th} (N - N_{th}) \right] E(t) \quad (2.11)$$

The real and imaginary parts of the refractive index are dependent on each other. This dependence can be derived from Kramers-Kronig relations and the dependence is given by

$$\alpha_l = \frac{\delta\eta_g}{\delta\eta'_g} = -2 \frac{\omega}{c} \frac{\partial n / \partial N}{\partial g / \partial N} \quad (2.12)$$

α_l is known as the linewidth enhancement factor which results in linewidth broadening. In bulk semiconductor lasers its value is high typically between 3 and 7. Use of lower dimensional structures like quantum wells or quantum dots can reduce the value of α_l and subsequently produce a very narrow spectrum. Up to this point the assumption was that the gain is linear with increasing population inversion. But at high intensities there is a reduction in the mode gain occurring due to different nonlinear mechanisms like spectral and spatial hole burning and dynamic carrier heating. To account for this a small nonlinear gain reduction factor (ε_{NL}) which is dependent on intensity is incorporated to the laser mode gain as

$$G(N, |E|^2) = G_N (N - N_0) (1 - \varepsilon_{NL} |E|^2) \quad (2.13)$$

Here N_0 is the carrier number at transparency. Now the time derivative of electric field inside the cavity can be written as

$$\frac{dE}{dt} = \frac{1 + i\alpha_l}{2} \left[G(N) - \frac{1}{\tau_p} \right] E(t) \quad (2.14)$$

τ_p is the lifetime of photons inside the laser cavity. Assuming almost uniform distribution of carriers in the active region and therefore neglecting the carrier diffusion, the rate equation describing the evolution of electron-hole pair number N is given by

$$\frac{\partial N}{\partial t} = \frac{I}{q} - \frac{N}{\tau_s} - R_{st}(N, |E|^2) \quad (2.15)$$

The first term represent the injection of the electron-hole pair into the active region due to the pumping current. I is total pumping current, q is the electronic charge and τ_s is the carrier lifetime. R_{st} accounts for the reduction in electron-hole pairs due to stimulated recombination.

$$R_{st}(N, |E|^2) = G(N)|E|^2 \quad (2.16)$$

Considering the above discussed factors the time evolution of semiconductor laser can be described by rate equations for electric field and the carrier number in active region. These equations are given by [24, 79]

$$\frac{dE}{dt} = \frac{1 + i\alpha_l}{2} \left[G_N(N - N_0)(1 - \epsilon_{NL}|E|^2) - \frac{1}{\tau_p} \right] E(t) + F_E(t) \quad (2.17)$$

$$\frac{dN}{dt} = \frac{I}{qV} - \frac{N}{\tau_s} - G_N(N - N_0)|E|^2 \quad (2.18)$$

The term $F_E(t)$ accounts for the spontaneous emission fluctuations. Spontaneously emitted photon will randomly perturb the amplitude and phase of the laser output. $F_E(t)$ is given by $\sqrt{2\beta N}\zeta(t)$ [80, 81]. β_{sp} is the spontaneous emission factor defined as the fraction of the total power coupled to the laser mode. $\zeta(t)$ is Gaussian white noise of zero mean unity intensity [81]. To exactly model the SCL dynamics, carrier fluctuations also need to be included in the rate equation for N . These fluctuations arise from the discrete nature of carrier generation and recombination processes. This shot noise term has much less im-

impact on the laser dynamics compared to the spontaneous emission noise [78, 80], therefore not included in the rate equations. The electric field is normalized such that $|E(t)|^2 = P(t)$, where $P(t)$ is the total number of photons inside the laser cavity at any time. So the rate equations can be written in terms of $P(t)$ by using the relation

$$E(t) = \sqrt{P(t)} \exp(i\phi(t)) \quad (2.19)$$

Also taking into account the contribution of the spontaneous emission into the oscillating laser mode, the rate equations become

$$\frac{dP(t)}{dt} = \Gamma G_N (N - N_0) (1 - \varepsilon_{NL} P) P - \frac{P}{\tau_p} + \Gamma \beta_{sp} \frac{N}{\tau_s} + F_P(t) \quad (2.20)$$

$$\frac{d\phi}{dt} = \frac{\alpha_l}{2} \left[G_N (N - N_0) (1 - \varepsilon_{NL} P) - \frac{1}{\tau_p} \right] + F_\phi(t) \quad (2.21)$$

$$\frac{dN}{dt} = \frac{I}{q} - \frac{N}{\tau_s} - G_N (N - N_0) (1 - \varepsilon P) P \quad (2.22)$$

The newly introduced term Γ is the optical confinement factor. It is defined as the ratio between the optical power confined in the active region to the total power flowing across the structure. The third term in the Equation 2.20 represent the contribution of the spontaneous emission to the laser mode. In optoelectronic delay feedback the phase of the output optical field is not involved in determining the system dynamics. So two differential equations are sufficient to simulate the time evolution of the system, one for the photon density and the other for the carrier density. Noise terms are not considered for our analysis presented in the next section. Numerical simulations are done using normalized carrier number and normalized power obtained by the transformation [24]

$$N \longleftarrow N/N_{th}, P \longleftarrow P/P_0 \quad (2.23)$$

where $P_0 = \Gamma (\tau_p/\tau_s) N_{th}$ and $N_{th} = N_0 + (\Gamma G_N \tau_p)^{-1}$ which is obtained by substituting threshold conditions in the rate equations. Also defining $\delta = N_0/N_{th}$ and $\varepsilon = \varepsilon_{NL} P_0$, the

rate equations without the noise terms can be written as[24]

$$\frac{dN}{dt} = \frac{1}{\tau_s} \left(\frac{I}{I_{th}} - N - \frac{N-\delta}{1-\delta} P \right) \quad (2.24)$$

$$\frac{dP}{dt} = \frac{1}{\tau_p} \left(\frac{N-\delta}{1-\delta} (1-\varepsilon P)P - P + \beta_{sp}N \right) \quad (2.25)$$

I_{th} is the threshold current given by $I_{th} = qN_{th}/\tau_s$. When optoelectronic feedback is introduced the total pumping current $I(t)$ at any instant of time becomes

$$I(t) = I_b + \kappa P(t - \tau) \quad (2.26)$$

here I_b is the constant bias current, κ is the feedback strength and τ represent the delay in feedback. This delay can arise from time taken for external transit of the laser beam, finite response time of the detector as well as the intentional delays included in the feedback circuitry.

2.2. LINEAR STABILITY ANALYSIS OF SCALAR DDES

A general approach to the linear stability analysis of scalar DDEs[30] is presented in this section. The basic form of the scalar DDE considered in this section is represented by

$$\dot{x} = -bx + af(x(t - \tau)) \quad (2.27)$$

parameters a and b are assumed to be positive and f is a nonlinear function. Let $x = x^*$ be an equilibrium point of Equation 2.27. When a linear perturbation of the form $x = x^* + \rho e^{\lambda t}$ where $\rho \ll 1$ is applied, the characteristic equation associated with the time delay differential equation 2.27 can be obtained as

$$\frac{d}{dt} [x^* + \rho e^{\lambda t}] = -b [x^* + \rho e^{\lambda t}] + af(x^* + \rho e^{\lambda(t-\tau)}) \quad (2.28)$$

$$\left. \frac{dx}{dt} \right|_{x=x^*} + \rho \lambda e^{\lambda t} = -bx^* - b\rho e^{\lambda t} + af(x^* + \rho e^{\lambda(t-\tau)}) \quad (2.29)$$

Since time derivative at the equilibrium point vanishes, the above expression can be reduced using Taylor expansion of the function at about the equilibrium point. This gives

$$\lambda = -b + af'(x^*)e^{-\lambda\tau} \quad (2.30)$$

This represents the characteristic equation of the scalar DDE under consideration. λ is the complex eigen value with the equilibrium point $x = x^*$ given as $\lambda = \alpha + i\beta$. In general the characteristic equation of a delay differential system $Y = f(X, X(t - \tau))$ can be written in the form

$$\left| J_0 + e^{-\lambda\tau} J_\tau - \lambda I \right| = 0 \quad (2.31)$$

where $X = \{x_i\}$ and $X^* = \{x_1^*, x_2^*, \dots, x_n^*\}$, is the equilibrium point. J_0 is the Jacobian with respect to the present variables, J_τ is the Jacobian with respect to the delayed variables respectively, evaluated at the equilibrium point given as

$$(J_0)_{ij} = \left. \frac{\partial f_i}{\partial x_j} \right|_{x_j=x_j^*} \quad (2.32)$$

and

$$(J_\tau)_{i,j} = \left. \frac{\partial f_i}{\partial x_{\tau j}} \right|_{x_{\tau j}=x_{\tau j}^*} \quad (2.33)$$

The characteristic equation happens to be a transcendental equation containing quasi-polynomials. Such type of equations can have infinite number of solutions in the complex plane. The problem of interest at this point is when the equilibrium point changes its stability. This happens when the real part of the eigen value crosses the imaginary axis i.e., $\lambda = i\beta$. Substituting this into Equation 2.31 we get

$$i\beta = -b + af'(x^*)(\cos\beta\tau - i\sin\beta\tau) \quad (2.34)$$

Separating into real and imaginary parts

$$b = af'(x^*)\cos\beta\tau \quad (2.35)$$

$$\beta = -af'(x^*)\sin\beta\tau \quad (2.36)$$

Squaring and adding the above two equations we get

$$\beta = \pm\sqrt{a^2f'^2(x^*) - b^2} \quad (2.37)$$

Since $\beta > 0$ the above equation can hold only if $|af'(x^*)| > b$. From Equation 2.35 one gets

$$\beta\tau = \pm\arccos\left(\frac{b}{af'(x^*)}\right) + 2n\pi \quad (2.38)$$

where n can take integer values $0, \pm 1, \pm 2, \dots$ etc. From the above equation one can find the condition when the real part of the eigen value becomes zero for a given value of β . To find what happens when a change in delay occurs $\frac{d\alpha}{d\tau}$ is calculated. A positive value for $\frac{d\alpha}{d\tau}$ means loss in stability and a negative value for $\frac{d\alpha}{d\tau}$ indicate gaining of stability of the equilibrium point with increase in delay on that particular curve. Since there can be many such curves, they divide the parameter space into different stable and unstable regions. From Equation 2.38 we get two sets of delay curves in the (τ, a, b) parameter space.

$$\tau_1(n) = \frac{2n\pi + \arccos\left(\frac{b}{af'(x^*)}\right)}{\sqrt{a^2f'^2(x^*) - b^2}}, n = 0, 1, 2, \dots \quad (2.39)$$

$$\tau_2(n) = \frac{2n\pi - \arccos\left(\frac{b}{af'(x^*)}\right)}{\sqrt{a^2f'^2(x^*) - b^2}}, n = 1, 2, 3, \dots \quad (2.40)$$

In the above equations n is chosen such that the values of τ is always positive. Stable regions are enclosed by curves with $d\alpha/d\tau$ negative on the lower side and positive on the upper side. For $\beta < 0$, n can take negative values and the curves thus obtained will have

identical behavior with the above ones. As mentioned above the real part of $\frac{d\lambda}{d\tau}$ tell us what happens on the stability curves. Differentiating Equation 2.30 with respect to τ , one gets

$$\frac{d\lambda}{d\tau} = af'(x^*)e^{-\lambda\tau} \left[-\lambda - \tau \frac{d\lambda}{d\tau} \right] \quad (2.41)$$

Using Equation 2.30 and some rearrangements the above equation takes the form

$$\frac{d\lambda}{d\tau} = -\frac{\lambda(\lambda + b)}{1 + \tau(\lambda + b)} \quad (2.42)$$

The real part of the above equation is

$$\frac{d\alpha}{d\tau} = \frac{\beta^2}{(1 + \tau b)^2 + \tau^2 \beta^2} \quad (2.43)$$

Thus it can be seen that $\frac{d\alpha}{d\tau}$ is always positive for both curves $\tau_1(n)$ and $\tau_2(n)$ if the condition $|af'(x^*)| > b$ is satisfied. So there does not exist an eigen value that has negative real part across the critical delay curves. By substituting $\tau = 0$ in the characteristic equation it can be directly shown that for $\tau = 0$ the equilibrium point is stable. From these arguments we can conclude that there can exist only one stable region in the (τ, a, b) parameter space bounded by the curves $\tau = 0$ and the curve closest to it. The dynamical equations of semiconductor laser as derived in the previous section comes under the category of coupled nonlinear equations. Though the above description is for scalar DDE, we follow similar approach to find the stability and Hopf bifurcations for semiconductor laser with optoelectronic feedback. The analysis of the delay differential equations derived for semiconductor laser with optoelectronic feedback turns more complicated than the scalar DDEs. A similar kind of analysis for coupled limit cycle oscillators had been reported in literature[82].

2.3. STABILITY ANALYSIS OF SCL RATE EQUATIONS WITH OPTOELECTRONIC FEEDBACK

The values of the parameters are chosen as $\tau_p = 6ps$, $\tau_e = 3ns$, $\delta = 0.692$, $\beta = 5.0 \times 10^{-5}$ [24]. To determine the stability of the fixed point of the system consisting Equations 2.24

& 2.25, nature of the roots of the characteristic equation has to be calculated. If all of the eigenvalues of the characteristic equation have negative real parts, then the equilibrium point is said to be stable. On the other hand, if at least one of the eigenvalues has a positive real part, then the equilibrium point is unstable. The characteristic equation for our set of rate equation becomes

$$\lambda^2 + K_2\lambda + K_3 + K_4e^{-\lambda\tau} = 0. \quad (2.44)$$

where

$$K_2 = \left(\frac{1}{\tau_e}\right) \left[1 + \frac{P_0}{1-\delta}\right] - \frac{N_0 - 1 - 2\varepsilon P_0(N_0 - \delta)}{\tau_p(1-\delta)} \quad (2.45)$$

$$K_3 = \frac{-1}{\tau_e\tau_p(1-\delta)} \left[\left(1 + \frac{P_0}{1-\delta}\right) (N_0 - 1 - 2\varepsilon P_0(N_0 - \delta)) + \left(\varepsilon P_0^2 - P_0 - \beta(1-\delta) \left(\frac{N_0 - \delta}{1-\delta}\right)\right) \right] \quad (2.46)$$

$$K_4 = \frac{-F}{\tau_e\tau_p(1-\delta)} [-\varepsilon P_0^2 + P_0 + \beta(1-\delta)] \quad (2.47)$$

Here F is defined as κ/I_{th} . A change in stability can occur only when a root of the Equation 2.44 crosses the imaginary axis, that is when the real part of the eigen value changes from negative to positive, where λ with $\alpha = 0$ is a solution of the equation. Substituting $\alpha = 0$ in Equation 2.44 and equating the real and imaginary parts of the resulting equation we get

$$K_2\beta - K_4\sin(\beta\tau) = 0 \quad (2.48)$$

and

$$-\beta^2 + K_3 + K_4\cos(\beta\tau) = 0 \quad (2.49)$$

which leads to

$$\tau_{\pm} = \frac{\pm \arccos\left(\frac{\beta^2 - K_3}{K_4}\right) + 2n\pi}{\beta} \quad (2.50)$$

where n is an integer. Squaring and adding equations 2.48 & 2.49 result in a fourth degree equation in β

$$\beta^4 + \beta^2(K_2^2 - 2K_3) + (K_3^2 - K_4^2) = 0 \quad (2.51)$$

This equation is solved to find the range of F , where β_2 is real and positive. τ_{\pm} are calculated using Equation 2.50 for these values of F . Both τ_{-} and τ_{+} satisfy the characteristic equation for $\alpha = 0$. The results we present in this work are specific to two types of feedback schemes. In the first scheme the feedback starts after the SCL has stabilized to the steady state operation. In the second scheme the feedback is present from the beginning of operation. In the first scheme the bifurcations happen on τ_{-} , but the feedback can be applied in many possible ways, of which one may lead to bifurcations on τ_{+} . As delay systems generally exhibit abundant multistability with complex basins of attraction [83], to devise such a unique scheme can be difficult. Since the feedback schemes we use in this work do not give bifurcations on τ_{+} , in the following discussions we assume

$$\tau_i(n) = \frac{-\arccos\left(\frac{\beta_i^2 - K_3}{K_4}\right) + 2n\pi}{\beta_i} \quad (2.52)$$

$i = 1, 2$ corresponding to two real and positive solutions of Equation 2.51. These are the critical values of delay (τ_c) where the stability changes. To find the direction in which the eigen value crosses the imaginary axis, $d\alpha/d\tau$ is calculated on each $\tau(n)$. If $d\alpha/d\tau$ is positive, at delay equal to $\tau_i(n)$, the eigen value crosses the imaginary axis to the positive side as the delay is increased and the fixed point becomes unstable. If $d\alpha/d\tau$ is negative at $\tau_i(n)$, the eigen value crosses the imaginary axis to the negative side of α and the fixed point becomes stable. Thus it can be seen that for the same value of F , depending on the value of delay, the fixed point can be stable or unstable.

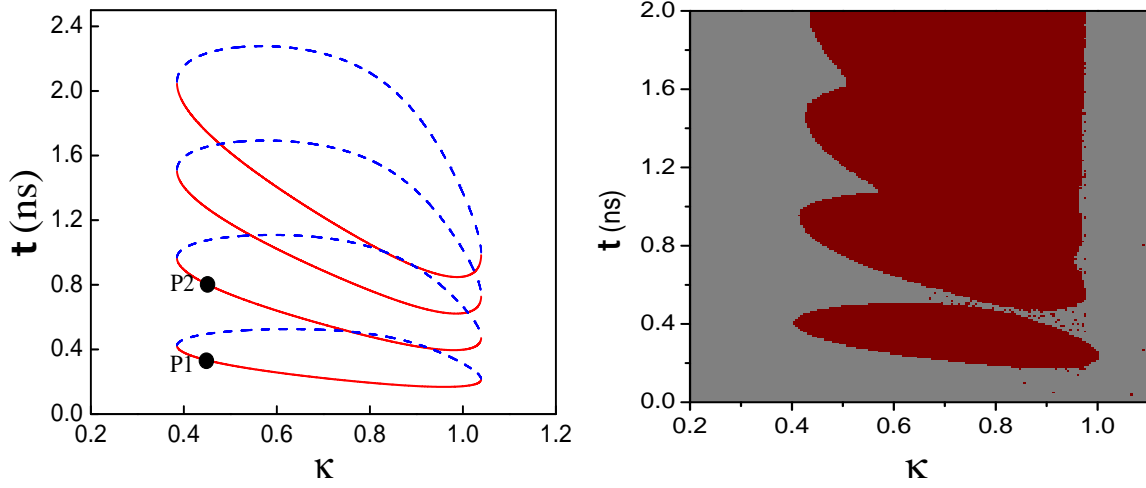


Figure 2.2: [a] Curves representing Eq.2.52 for the parameter values $I_0 = 1.5$, $\varepsilon = 0.025$ and for n from 1 to 4. Solid curves represent $\tau_1(n)$ and dashed curves represent $\tau_2(n)$. τ_1 and τ_2 for same value of n are joined to form closed curves. $\frac{d\alpha}{d\tau}$ is positive for τ_1 and negative for τ_2 . [b] Stability regions obtained by simulating the dynamical equations (1) and (2). Grey colored regions shows the points at which the laser go to a steady state when feedback is applied and the red colored regions shows the points, at which the laser go to an oscillatory state.

$$\frac{d\alpha}{d\tau} = \frac{-(K_4)\beta\sin(\beta\tau)(-K_2 + K_4\tau\cos(\beta\tau)) - K_4\beta\cos(\beta\tau)(2\beta - K_4\tau\sin(\beta\tau))}{(-K_2 + K_4\tau\cos(\beta\tau))^2 + (2\beta - K_4\tau\sin(\beta\tau))^2} \quad (2.53)$$

2.4. SIMULATION AND RESULTS

Fig. 2.2 shows the plot of $\tau(n)$'s from Equation 2.52 plotted against F for the parameter values $I_0 = 1.5$ and $\varepsilon = 0.025$, where I_0 is defined as I_b/I_{th} . Solid curves represent the critical delays with $d\alpha/d\tau$ positive and the dashed curves represent the critical delays with $d\alpha/d\tau$ negative. Substituting Equation 2.52 in Equation 2.53 we find that $d\alpha/d\tau$ is positive for τ_1 and negative for τ_2 for all values of n . τ_1 and τ_2 for the same value of n join to form closed curves ($\tau_1\tau_2(n)$). Four such closed curves for n equal 1 to 4 are shown in Fig. 2.2a. They exist only for a range of F , outside this range stability does not depend on τ . Also, immediately outside this range, α is negative, indicating fixed point is stable. Fig. 2.2b shows the scan of (F, τ) parameter space, by simulating the laser dynamics with feedback at

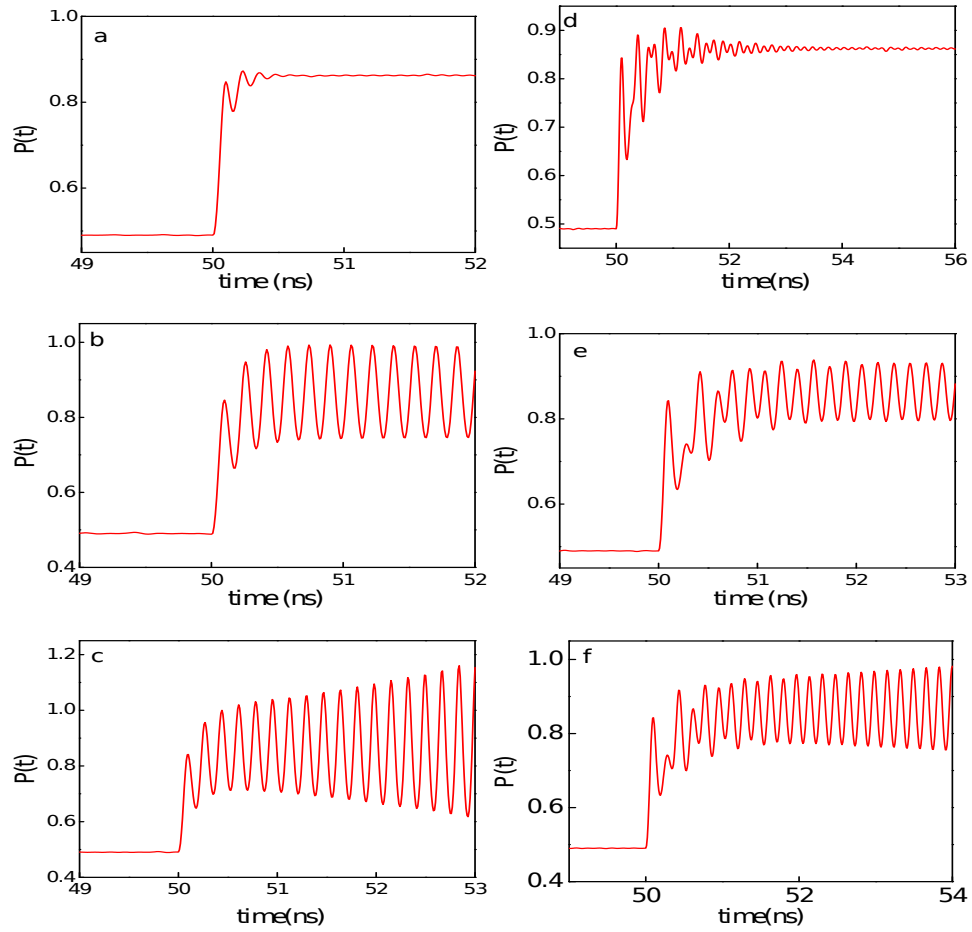


Figure 2.3: Solution $P(t)$ of the laser dynamical equations when the feedback is applied at $t = 50\text{ns}$ with $F = 0.45$. (a) Damped oscillatory decay to the fixed point at $\tau = 0.2\text{ns}$. (b) Periodic solution at $\tau = \tau_c = 0.33\text{ns}$. (c) Undamped growing oscillations at $\tau = 0.4\text{ns}$. (d) Damped oscillatory decay to the fixed point at $\tau = 0.75\text{ns}$. (e) Periodic solution at $\tau = \tau_c = 0.8\text{ns}$. (f) Undamped growing oscillations at $\tau = 0.85\text{ns}$. (a),(b) & (c) shows Hopf bifurcation happening at $\tau_c = 0.33\text{ns}$ and (d),(e) & (f) shows the same for $\tau_c = 0.8\text{ns}$.

each point. Grey colored area represent points where the solution $P(t)$ converged to a fixed point and the red colored regions represent the points where $P(t)$ is oscillatory. Substituting $\tau = 0$ in the characteristic equation and solving, we find that α is negative at $\tau = 0$ below the curve $\tau_1(n = 1)$. So the fixed point is stable at $\tau = 0$. Thus the first stability region is the area enclosed between the curves $\tau = 0$ and $\tau_1(n = 1)$. In Fig. 2.2b, this is the grey region below the first red patch. From $\tau_1(n = 1)$, stability regions are formed between a lower dashed curve and an upper solid curve. Inside the region enclosed by $(\tau_1 \tau_2(n))$, the fixed point is always unstable because, α calculated at the fixed point is always greater than

zero, as indicated by the solid lower curves and dashed upper curves. But at both ends of these curves, where there are no overlaps, stability regions are formed between $\tau_2(n)$ and $\tau_1(n+1)$. These are the protruding shaded regions on both sides in Fig. 2.2b. Successive curves overlap to greater extent in the middle and the stability regions are pushed towards both sides, reducing their area. In the simulations it is assumed that the feedback is applied after the laser has stabilized to its steady state. What happens when the feedback is applied before stabilization is discussed in section 2.4.3. Fig. 2.3 depict the Hopf bifurcations at the critical delay values. At $F = 0.45$, the first instance of losing stability occurs at the critical value of delay $\tau_c = 0.33ns$, this point is marked P1 in Fig. 2.2a. Fig. 2.3a shows $P(t)$ at 0.2 ns where $\tau < \tau_c$. When feedback is applied $P(t)$ suddenly stabilizes to the new fixed point with highly damped oscillations. At $\tau = \tau_c$ periodic solution appear as shown in Fig. 2.3b. When $\tau > \tau_c$, undamped growing oscillations are obtained (Fig. 2.3c). Fig. 2.3d, Fig. 2.3e and Fig. 2.3f depict the same scenario across the second instance (marked P2 in Fig. 2.2a) of losing stability at $\tau_c = 0.8ns$. This numerically verifies the Hopf bifurcation phenomena occurring along the critical delay curves with $d\alpha/d\tau$ is positive, that is, on $\tau_1(n)$.

2.4.1. EFFECT OF NONLINEAR GAIN REDUCTION FACTOR

We show that changes in ε can drastically change the critical delay curves. In Fig. 2.4 delay curves for increasing values of ε are plotted. For small values of ε stability regions are formed only on the lower side of F except for the first stability region that lies between $\tau = 0$ and $\tau_1(n = 1)$. This result is shown in Fig. 2.4a, for the value 0.01 of ε . Here all τ'_1 s where $d\alpha/d\tau$ is positive (solid curves) converge closer to $\tau = 0$ axis for higher values of F and at least one eigen value has positive real part above $\tau_1(n = 1)$, on the right end. The span of the curves decreases, as ε is increased to 0.02 in Fig. 2.4b, which indicates that delay has a role in determining stability only for shorter range of F . With further increase in ε , the curves with $d\alpha/d\tau$ positive and negative for the same n join at the right end to form closed structures ($\tau_1\tau_2(n)$) and stability regions are formed at both ends. At the same time, extent of overlap between these closed curves reduces. In Fig. 2.4c, ($\tau_1\tau_2(1)$) and ($\tau_1\tau_2(2)$) completely move apart from overlap for $\varepsilon = 0.03$ and the stability region becomes continuous

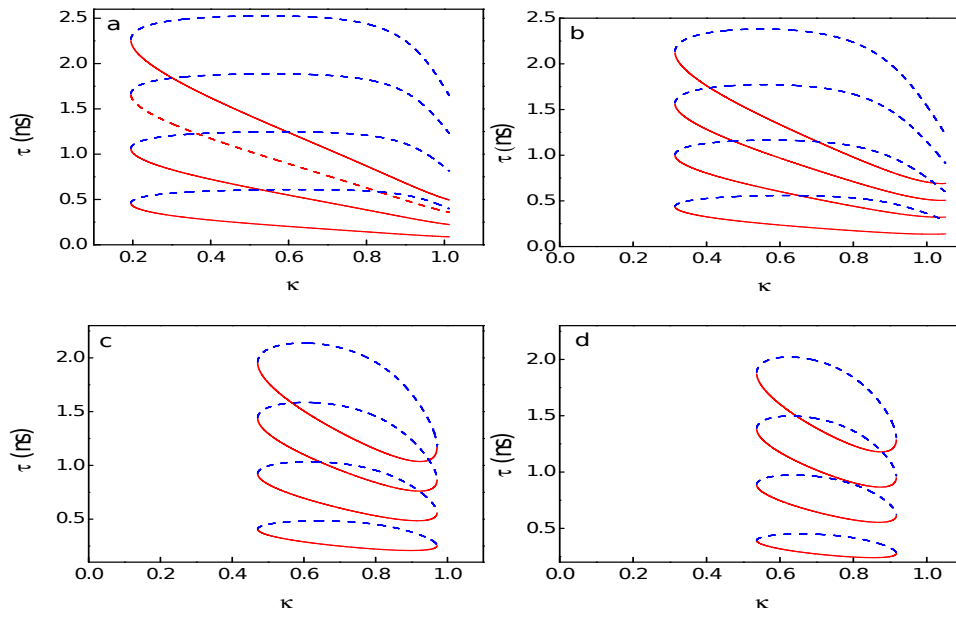


Figure 2.4: Critical delay curves for four different values of ε . (a) $\varepsilon = 0.01$, (b) $\varepsilon = 0.02$, (c) $\varepsilon = 0.03$, (d) $\varepsilon = 0.031$.

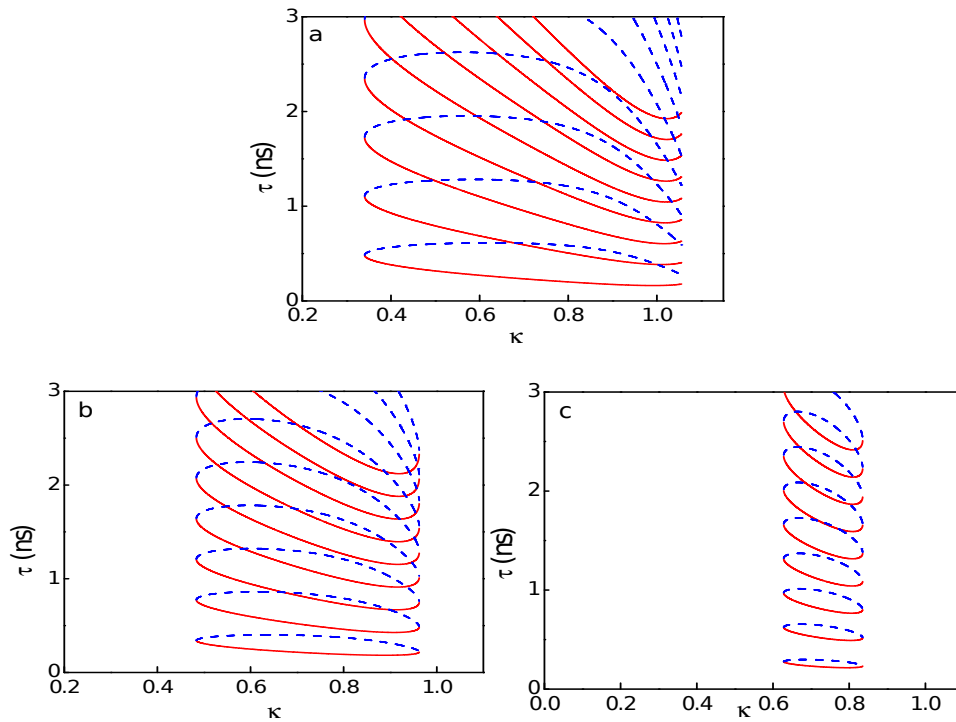


Figure 2.5: Critical delay curves for four different values of I_0 . (a) $I_0 = 1.4$, (b) $I_0 = 1.7$, (c) $I_0 = 1.9$.

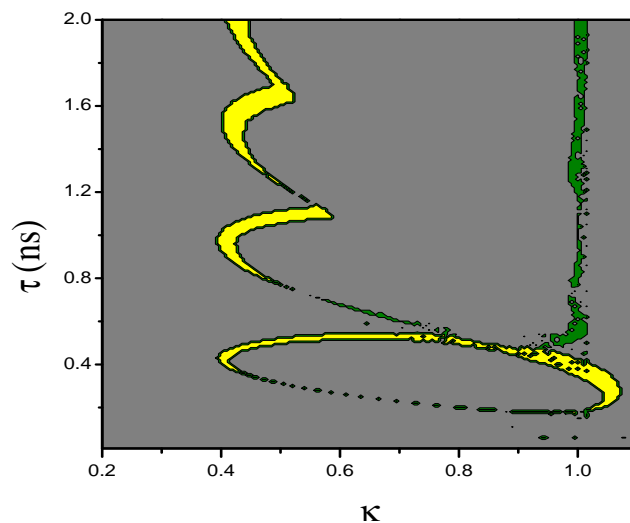


Figure 2.6: Differences in final states when feedback is applied after the SCL is stabilized to the fixed point and before stabilization, for the parameter values $I_0 = 1.5$, $\varepsilon = 0.025$. In the completely shaded region the SCL goes to the same final state in both cases. In the completely unshaded area, SCL goes to a fixed point when feedback is started after the laser is stabilized to the fixed point and to an oscillatory solution when the feedback is started at time $t = \tau(\text{delay})$. In the half shaded regions the dynamics is switched. The SCL goes to an oscillatory state under the first situation and to a fixed point under the second.

between them. More curves move apart as ε is increased and they change to elliptical in shape as shown in Fig. 2.4d. Around $\varepsilon = 0.035$ the curves completely disappear, making stability of the fixed point independent of τ .

2.4.2. EFFECT OF BIAS CURRENT

Fig. 2.5a, Fig. 2.5b and Fig. 2.5c shows critical delay curves at $\varepsilon = 0.025$ for I_0 equal to 1.4, 1.7 and 1.9 respectively. Increase in I_0 has similar effects as increase in ε . Dependence of stability on delay converges to shorter ranges of F , for higher I_0 's. The closed curve structures ($\tau_1 \tau_2(n)$) changes to oval in shape and the extent of overlap between the them reduces. Around I_0 equal to 1.9 four curves move apart and form continuous stability regions between them. As a result of flattening of the closed curves, for higher I_0 successive Hopf bifurcations come closer in delay. The curves completely disappear before I_0 is increased upto 2.

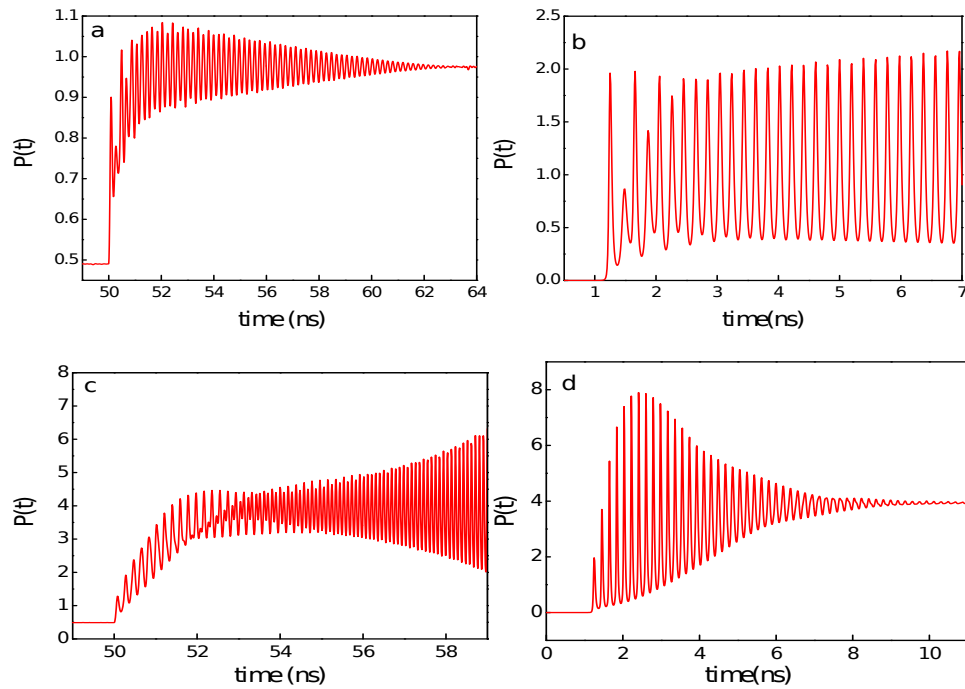


Figure 2.7: Solution $P(t)$ of the rate equations for two different initial conditions for the parameter values $F = 0.52$, $I_0 = 1.5$ and $\tau = 1.1 ns$. (a) Feedback is applied at $50 ns$ when the laser is already operating at its steady state. Dynamics converge to the new fixed point after damped oscillations. (b) Feedback mechanism is present from a time $t = \tau$ after the beginning of the operation. Here solution goes to oscillatory state. (c) and (d) shows the final states switched for $F = 0.99$, and $\tau = 0.53 ns$.

2.4.3. EFFECT OF INITIAL CONDITION

Numerical simulations in the previous sections had the assumption that the laser has settled to the steady state before feedback is applied. Thus for the delay differential equations representing the delay feedback dynamics the initial condition is a constant function, namely the steady state solution without feedback. But, situations can arise, where this is not the case. Feedback can be present from $t = \tau$, where τ is the delay in feedback. Here, if τ is shorter than the time taken by SCL to stabilize to the fixed point after relaxation oscillations, the initial function is not a constant. For certain set of (F, τ) values oscillatory states appear, in place of the fixed point in the previous case, and vice versa, with all the other parameters being same. But the final states are identical for most regions in the parameter space. Fig. 2.6 characterizes the (F, τ) parameter space for these three types of behaviour. One such instance for parameter values $F = 0.52$, $I_0 = 1.5$ and $\tau = 1.1 ns$ is given in Fig. 2.7. In Fig. 2.7a, when the feedback is applied at $t = 50 ns$, SCL is already operating at the steady

state, and $P(t)$ settles to the new fixed point after damped oscillations. Fig. 2.7b shows the case, when feedback is present from 1.1 ns, which is equal to the delay. In this case $P(t)$ is undamped and slowly growing. Such points are represented by the yellow colored regions in Fig. 2.6. If $P(t)$ is oscillatory when initial feedback function is constant, one would expect the same for a case when the initial feedback function itself is oscillatory. But we get the unexpected result as shown in Fig. 2.7c & Fig. 2.7d. Here the final state is the fixed point when feedback is applied at $t = \tau(0.53 ns)$, but final state is oscillatory when feedback is applied after the stabilization of the SCL to the fixed point. The half green regions in Fig. 2.6 represent this behaviour. For the rest of the parameter space, the initial function does not influence a change from stable fixed point to oscillatory output or vice versa.

2.5. CONCLUSIONS

We have done the linear stability analysis of the nonlinear delay differential equations arising in a semiconductor laser with optoelectronic delay feedback. Critical stability curves and Hopf bifurcation points obtained are in agreement with numerical simulations, provided feedback is given after the SCL stabilized to the fixed point. Deviations from the predicted behaviour, when the feedback is present from the beginning, are discussed. Effects of nonlinear gain reduction factor and bias current are deduced from the analysis and are numerically verified. Increase in both of these parameters reduces the range of feedback strength where the stability depends on delay. Beyond a critical value, stability of the steady state solution becomes independent of delay.

3

DELAY SIGNATURES IN THE DYNAMICS OF QDL WITH OPTICAL FEEDBACK

Research in complex systems require quantitative predictions of their dynamics, even before we completely understand the underlying mechanisms. This can only be done by collecting data about the past evolution and retrieving the structures in the dynamics from the collected data. Numerous statistical and information theoretical approaches have been successfully employed for analyzing the time series obtained from the observation of complex processes. Due to the finite speed of information propagation, interaction between different components of a complex system do inevitably involve time delays. Identifying these delays are crucial for modeling and forecasting applications in different fields including biology[40], optics[80, 84] and climate science[31]. Most conventional and widely used methods for estimating delay in complex dynamics are auto correlation function (ACF) and delayed mutual information (DMI). Several new techniques were recently discovered for delay identification [85–89]. Information theory measures like Entropy and Complexity have been particularly useful in the case of nonlinear systems[80, 88]. In the present work we focus on the dynamics of a Quantum Dot Laser(QDL) with optical feedback work-

ing in the coherence collapse regime. Dynamics of QDLs show quite distinctive features compared to bulk semiconductor dynamics. Conventional Lang-Kobayashi equations fail in many places to accurately predict QDL dynamics[27]. In QDLs relaxation oscillations are strongly damped due to different carrier capture dynamics into the Quantum Dots (QDs)[90]. Strong damping added with relatively small line width enhancement factor(α_l) make QDLs less sensitive to optical feedback[29]. So instabilities in QDLs occur at higher feedback strengths compared to bulk or Quantum Well Lasers. Synchronization of QDLs working in the chaotic regime is currently an active research area with the prospect of using them for secure communication with chaotic carriers[28]. A major concern in chaos based secure communication is the level of difficulty in identifying the parameters of the chaotic emitter from the output time series. Chaos generated in feedback systems can have very high dimensionality due to the infinite number of degrees of freedom introduced by time delay. But once the delay value is retrieved from the time series, the high dimensional attractor can be projected to a low dimensional phase space, which may result in low complexity numerical techniques to decrypt the information. This security aspect of chaos based communication had been addressed for semiconductor lasers modeled with conventional Lang-Kobayashi equations[80, 91, 92]. Rontani et.al. [91] showed that a careful choice of laser operating conditions can make delay retrieval extremely difficult. In another work [92], the same group also demonstrated that the time scales of laser dynamics in its route to chaos influence the difficulty in delay identification. Recently, information theory measures like permutation entropy(H_S) and permutation statistical complexity(C_{JS}) were employed to get good estimates of delay value from the time series of delay differential systems. Soriano et. al.[80] used this approach to find the intrinsic time scales in the dynamics of a semiconductor laser with optical feedback operating in the coherence collapse regime. We use ACF, DMI, H_S and C_{JS} to retrieve delay from the output intensity time series of a QDL with external cavity. H_S and C_{JS} are calculated from a probability distribution which is characteristic of the given time series. This probability distribution is created using a proper reconstruction of the dynamics from the time series. Bandt and Pompe symbolization method is employed for this purpose[88, 93]. Different dimensionality of reconstruc-

tion are used for the calculation and we compare the results. Reliability of these measures are investigated for different values of external cavity round trip time and feedback rates.

3.1. QUANTUM DOT LASER MODEL

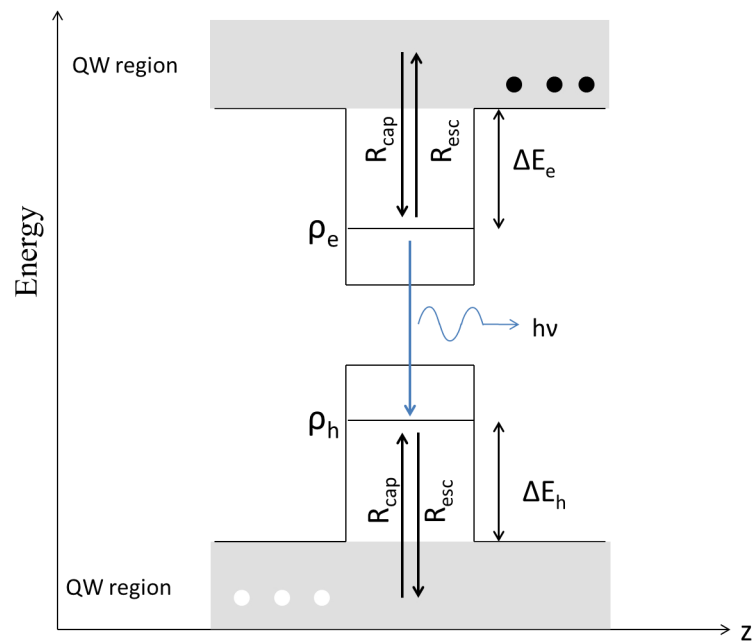


Figure 3.1: Energy band diagram of a QD. ΔE_e and ΔE_h are the energy differences of the lasing levels from the band edge of the QW, for electrons and holes respectively. The ground state lasing energy is $h\nu$. R_{cap} and R_{esc} represent the carrier capture from and escape to the QW region.

We adopt the dynamical model of QDL from Ref. [29]. A schematic representation of the band diagram assumed in the model is given in Figure 3.1. The QD is inserted into a QW and the QW will act as a reservoir for both electrons and holes. This architecture bring performance improvements like low threshold conditions and its temperature stability. The carriers are first injected into the quantum well before being captured into the quantum dots by different mechanisms as explained below. ΔE_e and ΔE_h are the energy differences of the lasing levels from the band edge of the QW, for electrons and holes respectively. Evolution of both type of carriers is given by the same rate equation, assuming equal number and similar dynamics. Also possibility of more number of energy levels in the quantum dot

and the possible transitions between them is not taken into consideration here. Despite these approximations, as mentioned in [29], this model adequately explain many features of the dynamics of QDLs. The dynamics is described by the following set of delay differential equations that give the time evolution of the complex amplitude of the electric field(E), occupation probability in a dot(ρ) and the carrier density in the well(N).

$$\dot{E} = -\frac{E}{2\tau_s} + \frac{g_0 V}{2} (2\rho - 1) E + i \frac{\delta\omega}{2} E + \frac{\gamma}{2} E(t - \tau) \quad (3.1)$$

$$\dot{\rho} = -\frac{\rho}{\tau_d} - g_0 (2\rho - 1) |E|^2 + F(N, \rho) \quad (3.2)$$

$$\dot{N} = \frac{J}{q} - \frac{N}{\tau_n} - 2N_d F(N, \rho) \quad (3.3)$$

τ_s, τ_n and τ_d are the photon lifetime, carrier lifetime in the well and the carrier lifetime in the dot, respectively. $g_0 = \sigma v_g$ where σ is the cross section of interaction of the carriers in the dots with the electric field and v_g is the group velocity. $V = 2N_d \Gamma / d$, where N_d is the two dimensional density of dots, Γ is the confinement factor and d is the thickness of the dot layer. J is the pump current density and q is the electronic charge. γ is the feedback rate and τ is the delay involved in the feedback process. $F(N, \rho)$ is the rate of exchange of carriers between the well and dots and is given by $F(N, \rho) = R_{cap}(1 - \rho) - R_{esc}\rho$. $R_{cap} = CN^2 + BN$ where B describes carrier-phonon capture and C describes Auger carrier capture. For simulations B is taken as zero. This is justified because discrete nature of QD energy levels and fixed energies of Longitudinal Optical (LO) phonons make carrier-phonon capture in QD structures highly improbable [90]. Temperature dependent carrier escape from the dots is given by R_{esc} . $\delta\omega$ take into account the dependence of laser frequency on carrier densities in QW and QD regions. $\delta\omega = \beta_1 N + \beta_2 \rho$ where plasma effect from the carriers in the well is described by β_1 and variations caused by population in the dots is described by β_2 [29]. The values used in the simulations are $\tau_s = 3ps$, $\tau_n = \tau_d = 1ns$, $g_0 = 0.9259 \times 10^{-10} m^3 s^{-1}$, $V = 2.4 \times 10^{22} m^{-3}$, $N_d = 2 \times 10^{15} m^{-2}$, $\beta_1 = 0$, $\beta_2 = 2$, $C = 10^{-20} m^4 s^{-1}$, $R_{esc} = 0$, $J = 125 A/cm^2$ [29].

When there is no feedback present equation 3.1 reduces to

$$\dot{E} = -\frac{E}{2\tau_s} + \frac{g_0 V}{2} (2\rho - 1) E + i \frac{\delta\omega}{2} E \quad (3.4)$$

Complex conjugate of the above equation can be written as

$$\dot{E}^* = -\frac{E^*}{2\tau_s} + \frac{g_0 V}{2} (2\rho - 1) E^* - i \frac{\delta\omega}{2} E^* \quad (3.5)$$

Multiplying Equation 3.4 by E^* and 3.5 by E and adding the resulting equations we get

$$E^* \dot{E} + \dot{E}^* E = -\frac{E^* E}{\tau_s} + g_0 V (2\rho - 1) E^* E \quad (3.6)$$

The term on the left is the total derivative of $E^* E$ and this quantity is the photon density in the active region (S). So the rate equation without feedback can be written as

$$\dot{S} = -\frac{S}{\tau_s} + g_0 V (2\rho - 1) S \quad (3.7)$$

$$\dot{\rho} = -\frac{\rho}{\tau_d} - g_0 (2\rho - 1) S + F(N, \rho) \quad (3.8)$$

$$\dot{N} = \frac{J}{q} - \frac{N}{\tau_n} - 2N_d F(N, \rho) \quad (3.9)$$

At threshold the losses in the cavity just equals the gain. In Equation 3.7 the first term on the right had side represent the losses and the second term represent the gain. So at threshold

$$-\frac{1}{\tau_s} + g_0 V (2\rho - 1) = 0. \quad (3.10)$$

This gives the carrier density in the dots at threshold as

$$\rho_{th} = \frac{1}{2} + (2\tau_s g_0 V)^{-1} \quad (3.11)$$

If one keep the current density just at the threshold value, the rate equation for carrier density in the active region is given by

$$\dot{\rho} = -\frac{\rho_{th}}{\tau_d} - g_0(2\rho_{th} - 1)S + CN_{th}^2(1 - \rho) = 0 \quad (3.12)$$

From the above equation the carrier density in the well at threshold (N_{th}) can be derived as

$$N_{th} = \sqrt{\frac{\rho_{th}}{C\tau_d(1 - \rho_{th})}} \quad (3.13)$$

Substituting the values for ρ_{th} and N_{th} in the rate equation for N ,

$$\dot{N} = \frac{J_{th}}{q} - \frac{N_{th}}{\tau_n} - 2N_dCN_{th}^2(1 - \rho) \quad (3.14)$$

An approximate equation for threshold current density can be obtained from the above equation as

$$J_{th} = \frac{q}{\tau_n} \sqrt{\frac{\rho_{th}}{c\tau_d(1 - \rho_{th})}} + \frac{2N_d\rho_{th}q}{\tau_d} \quad (3.15)$$

3.2. AUTO CORRELATION FUNCTION

ACF quantifies the linear relationship between a signal and its time-shifted version. In other words it is the similarity between observations as a function of the time lag between them. ACF find applications in different fields and its definition may slightly differ depending on the application. For our study ACF for a random process $X(t)$ is defined as [92]

$$\Gamma(\theta) = \frac{1}{\hat{\sigma}_X^2} \langle (x(t) - \hat{\mu}_X)(x(t + \theta) - \hat{\mu}_X) \rangle \quad (3.16)$$

$x(t)$ and $x(t + \theta)$ are sampled from $X(t)$. $\hat{\mu}_X = \langle x(t) \rangle$ and $\hat{\sigma}_X = \langle (x(t) - \hat{\mu}_X)^2 \rangle^{1/2}$. $\langle \cdot \rangle$ denotes expectation value.

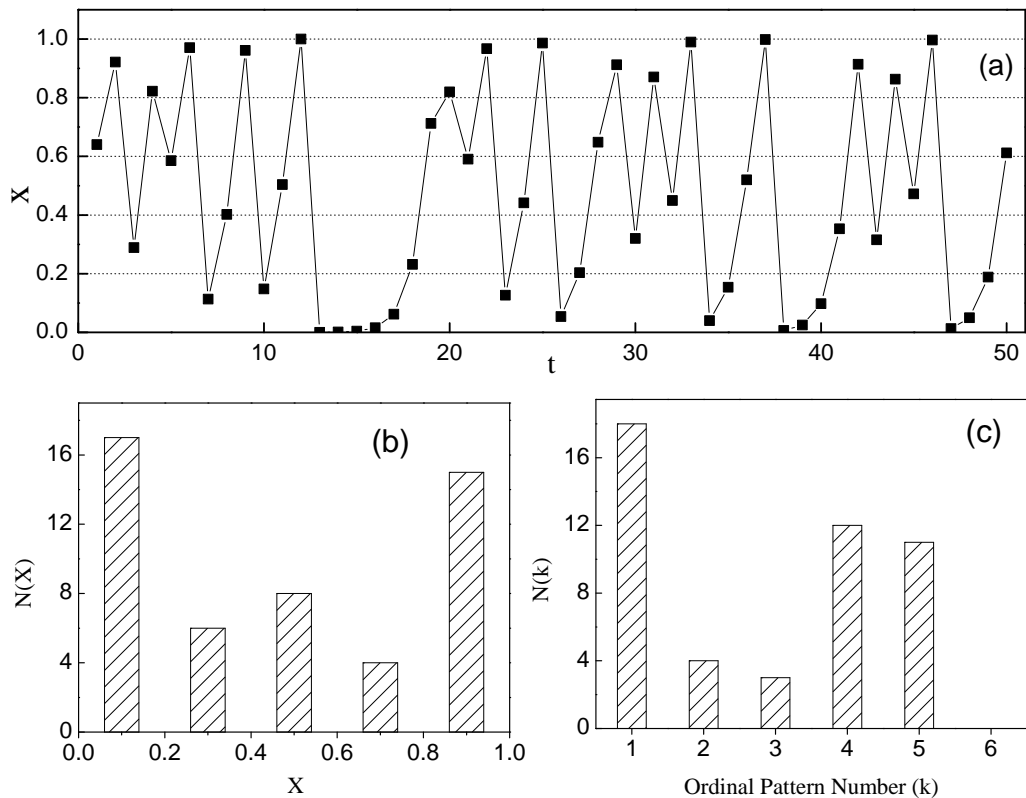


Figure 3.2: Comparison of histogram and ordinal pattern based methods. (a) shows the time series generated using logistic map for control parameter value of 4. (b) shows the histogram generated and (c) shows the distribution generated using BP method.

3.3. BANDT AND POMPE SYMBOLIZATION METHOD

Information theoretic measures are computed from a probability distribution which is constructed from a time series, which in turn is obtained by recording some real world process. The construction of the probability distribution from the time series is very crucial because any loss of information in this phase will get reflected in the final quantitative measure. One approach is to divide the total range of data into large number of bins and count the number of occurrences of the data in each bin. The histogram thus generated can serve as the probability distribution for the calculation of the proposed measures. The histogram method has the drawback that it does not take into account the time correlations arising in the time series. In this work we use the method proposed by Bandt and Pompe, which is based on the symbolic reconstruction of time series data. Bandt and Pompe (BP) method

is devised such that information regarding the time causality is not lost in the generated probability distribution. The original work and many research works that followed showed the robustness of this method in the presence of dynamical or observational noise[93]. BP method has recently been applied successfully in the time series analysis of chaotic dynamical systems[80, 88]. A detailed description about the method is given in references [80] and [88]. The method is briefly explained below. Given a time series $x_t, t = 1, 2, \dots, n$, an embedding dimension D and a time delay (τ), a D dimensional vector is constructed as

$$s \mapsto (x_{s-(D-1)\tau}, x_{s-(D-2)\tau}, \dots, x_{s-\tau}, x_s) \quad (3.17)$$

This vector is then rearranged as

$$x_{s-r_0\tau} \geq x_{s-r_1\tau} \geq x_{s-r_2\tau} \dots \geq x_{s-r_{D-2}\tau} \geq x_{s-r_{D-1}\tau} \quad (3.18)$$

to get an ordinal pattern

$$\pi = (r_0, r_1, \dots, r_{D-1}) \quad (3.19)$$

Each possible ordinal pattern that is generated in this way, is an element of the set of all permutations of $(0, 1, \dots, D-1)$. If we have a sufficiently long time series that satisfy $N \gg D!$, an ordinal pattern probability distribution $P = \{p(\pi_i), i = 1, 2, \dots, D!\}$ can be generated.

In the following example (Figure 3.2) a comparison of histogram and ordinal pattern based methods is presented. The data shown in the figure 3.2a is generated using the well known logistic map given by

$$x(t+1) = \mu x(t)(1-x(t)) \quad (3.20)$$

Here μ is the control parameter and t is the discrete time. x can take values between 0 and 1. The value of λ is taken as 4, which results in chaotic dynamics. For demonstration purpose only 50 data points in the time series are considered. The range of x is divided into 5 bins as shown in Fig. 3.2a. The histogram obtained is shown in Fig. 3.2b. After proper

normalization, this will serve as a probability distribution that characterizes the given time series. For ordinal pattern calculation D is taken as 3, so $3! = 6$ different patterns can be formed. They are numbered as given below.

pattern	Number
(0,1,2)	1
(0,2,1)	2
(1,0,2)	3
(1,2,0)	4
(2,0,1)	5
(2,1,0)	6

Delay of reconstruction is 1. Since $D = 3$, first vector can be constructed at $t = 3$. Thus

$$S_3 = (x(1), x(2), x(3)) = (0.64, 0.9216, 0.28901)$$

Similarly

$$S_4 = (x(2), x(3), x(4)) = (0.9216, 0.28901, 0.82194)$$

Rearranging S_3 and S_4 in descending order we get

$$\begin{aligned} S'_3 &= (0.9216, 0.64, 0.28901) = (x(2), x(1), x(3)) \\ &= (x(3-1), x(3-2), x(3-0)) \end{aligned}$$

and

$$\begin{aligned} S'_4 &= (0.9216, 0.82194, 0.28901) = (x(2), x(4), x(3)) \\ &= (x(4-2), x(4-0), x(4-1)) \end{aligned}$$

Following the procedure described above we get the 4th ordinal pattern from S'_3 and the

5^{th} ordinal pattern from S'_5 . Totally 48 such vectors can be generated from 50 data points and the distribution obtained is given in 3.2c. The pattern 6 is completely absent in the time series (Fig.3.2c). The absence and presence of such patterns in the distribution plays an important role in complexity calculations. This type of behavior is generally absent in histogram based calculations. This is because when generating a histogram we take the values at each point in time without considering the values preceding it.

3.4. PERMUTATION ENTROPY

One of the natural approaches to quantify the information content of a process is the Shannon Entropy(S). It is given by

$$S[P] = - \sum_{i=1}^M p_i \ln(p_i) \quad (3.21)$$

S is calculated from a probability distribution $P = \{p_i : i = 1, \dots, M\}$ of some observable, associated with the process. M represent the total number of states the observable can take. S is also the measure of uncertainty associated with the process. If we can perfectly predict the outcome at any instant, there is minimum uncertainty, and $S[P] = 0$. In contrast, if there is equal probability for all the states to occur, uncertainty is maximum and $S[P_e] = \ln(M)$. Here P_e denotes uniform probability distribution $P_e = \{1/M, 1/M, \dots, 1/M\}$. Normalized Shannon Entropy H is defined as

$$H[P] = S[P]/S[P_e]. \quad (3.22)$$

Here we construct the probability distribution using the BP method described above. Shannon Entropy calculated using this probability distribution is the Permutation Entropy represented by $H_S[P]$. In the following discussions, Permutation Entropy is always used in the normalized form.

3.5. DELAYED MUTUAL INFORMATION

Mutual Information quantifies the amount of information that one random variable contains about another random variable. It is the reduction in the uncertainty of one random variable due to the knowledge of other. Mutual information can be defined in terms of relative entropy. Relative entropy is a measure of the distance between two distributions. In other words relative entropy gives the inefficiency of assuming that the distribution is q when the actual distribution is p . The relative entropy or Kullback Leibler distance between two probability density functions p and q is defined as [94]

$$S_{KL}(p/q) = \sum_x p(x) \ln [p(x)/q(x)] \quad (3.23)$$

Using the above definition of relative entropy, Mutual Information can be defined in the following way. Consider two random variables X and Y with a joint probability density function $p(x, y)$ and marginal probability density functions $p(x)$ and $p(y)$. Then, the Mutual Information $I(X, Y)$ is the relative entropy between the joint distribution and the product distribution [94].

$$I(X, Y) = \sum_{x \in X} \sum_{y \in Y} p(x, y) \log \left(\frac{p(x, y)}{p(x)p(y)} \right) \quad (3.24)$$

$I(X, Y)$ can also be expressed in terms of Shannon Entropy S .

$$I(X, Y) = S(X) + S(Y) - S(X, Y) \quad (3.25)$$

Here $S(X, Y)$ is the joint entropy given by

$$S(X, Y) = - \sum_{x \in X} \sum_{y \in Y} p(x, y) \log(p(x, y)) \quad (3.26)$$

Delayed Mutual Information (DMI) is the Mutual Information between a signal $X(t)$ and its time shifted version $X(t + \theta)$. It can be obtained from the above definitions as

$$I(\theta) = \sum_{x, x(t+\theta) \in X} p(x(t), x(t+\theta)) \log \left(\frac{p(x(t), x(t+\theta))}{p(x(t))p(x(t+\theta))} \right) \quad (3.27)$$

Also,

$$I(\theta) = S(X(t)) + S(X(t+\theta)) - S(X(t), X(t+\theta)) \quad (3.28)$$

3.6. PERMUTATION STATISTICAL COMPLEXITY

The term complexity is often accepted without a precise quantitative definition. But a lot of theoretical work had been carried out in the past to quantify complexity arising in different contexts. A detailed survey of the subject in scientific literature suggest that there may not be a unique definition of complexity, that can be applied in all circumstances. For example two important methods often used to quantify complexity are Algorithmic complexity and Dimension of a chaotic attractor. Algorithmic complexity refers to the time and memory space an algorithm needs as a function of the size of the input data[95]. In other words this measure gives how the resources required to compute a problem increases as the size of the problem increases for the algorithm under consideration. Dimension of a chaotic attractor gives the number of active variables of the system. If the number of active variables is high extremely complex dynamics can take place, as in the case of delay systems.

The complexity measure used for delay identification in this work is the statistical complexity. The definition and a detailed study of the properties of statistical complexity can be found in references [96–99]. Statistical complexity measures has recently been used for delay identification in nonlinear systems[80, 88]. Statistical Complexity measures can provide useful information about the structure of the underlying dynamics when the dynamics is not perfectly random or ordered[97]. The basic form of the definition is adopted from the work of Lopez Ruiz, Mancini and Calbet (LMC)[96, 98, 99] and their definition is given as

$$C^{LMC} = Q[P, P_e]H[P] \quad (3.29)$$

Here H is the normalized Shannon Entropy($0 < H < 1$) as defined in the previous sec-

tion. Q is called "disequilibrium" which is a measure of how far is the given probability distribution P is from the uniform probability distribution P_e . Q can be written in a general form

$$Q[P, P_e] = Q_0 D[P, P_e]. \quad (3.30)$$

where D is a measure of distance and Q_0 is a normalization constant. Rigorous theoretical work has been done to find the most suitable way to compute Q . One approach is to use the Euclidean distance[96].

$$\begin{aligned} Q_E[P, P_e] &= Q_0^{(E)} \|P - P_e\|_E \\ &= Q_0^{(E)} \sum_{i=1}^N \{p_i - 1/N\}^2 \end{aligned} \quad (3.31)$$

If one uses the Euclidean norm, the stochastic nature of the vectors P is ignored. These vectors are essentially calculated from a finite sample, so they are always prone to statistical errors. Due to these errors, the observed frequencies of occurrence of the output states may differ from the actual probabilities. In other words finite sample size always restrict us from distinguishing distributions which are closer than typical fluctuations. It is possible to circumvent this issue using other distance measures which are more statistical in nature. As stated in Ref [96] statistical complexity measures are best suited to reveal the intricate structures hidden in the complicated dynamics of simple systems. For any given value of H , C^{LMC} can take values between a minimal value and a maximal value. Another approach is to use Kullback-Leibler relative entropy $S_{KL}(p/q)$ as described in the previous section. $S_{KL}(p/q)$ measures just how different both distributions are, taking $\{q_i\}$ as the reference distribution. If we take the uniform distribution as the reference, it follows

$$\begin{aligned} S(p/p_e) &= \sum_i p_i \ln(p_i/p_e) \\ &= \sum_i [p_i \ln(p_i) - p_i \ln(p_e)] \\ &= -\sum_i p_i \ln(p_e) - \left[-\sum_i p_i \ln(p_i) \right] \end{aligned}$$

$$\begin{aligned}
&= \sum_i p_i \ln(N) - H \ln(N) \\
&= (1 - H) \ln(N)
\end{aligned} \tag{3.32}$$

In the present work we adopt a definition of Statistical complexity which goes to zero when the process is completely random or perfectly ordered[96, 100]. The distance measure is based on Jensen-Shannon divergence as detailed below. Permutation Statistical Complexity (C_{JS}) is defined over two probability distributions - probability distribution of the ordinal patterns(P) obtained as discussed previously and the uniform distribution(P_e).

$$C_{JS}[P] = Q_J[P, P_e] H_S[P] \tag{3.33}$$

where Q_J is the disequilibrium which quantify how distant P is from P_e . Q increases if the system has preferred states among the accessible ones. Q_J is defined in terms of Jensen-Shannon divergence $\mathcal{J}[P, P_e]$.

$$Q_J[P, P_e] = Q_0 \mathcal{J}[P, P_e] \tag{3.34}$$

with

$$\mathcal{J}[P, P_e] = S[(P + P_e)/2] - S[P]/2 - S[P_e]/2 \tag{3.35}$$

Q_0 is a normalization constant corresponding to the maximum possible value of $\mathcal{J}[P, P_e]$ which is equal to $-2\{((N+1)/N) \ln(N+1) - 2 \ln(2N) + \ln N\}^{-1}$. Maximum value for $\mathcal{J}[P, P_e]$ occurs for a distribution P , which has a particular component (p_j) equal to 1, and all the remaining components zero.

3.7. NUMERICAL SIMULATIONS

Dynamical equations are scaled properly before performing numerical calculations. Time(t) is nondimensionalized by scaling it with respect to the photon lifetime as $t/2\tau_s$. Feedback rate(γ) and the electric field(E) are scaled as $\tau_s \gamma$ and $(2\tau_s g_0)^{-1/2} E$, respectively. Simula-

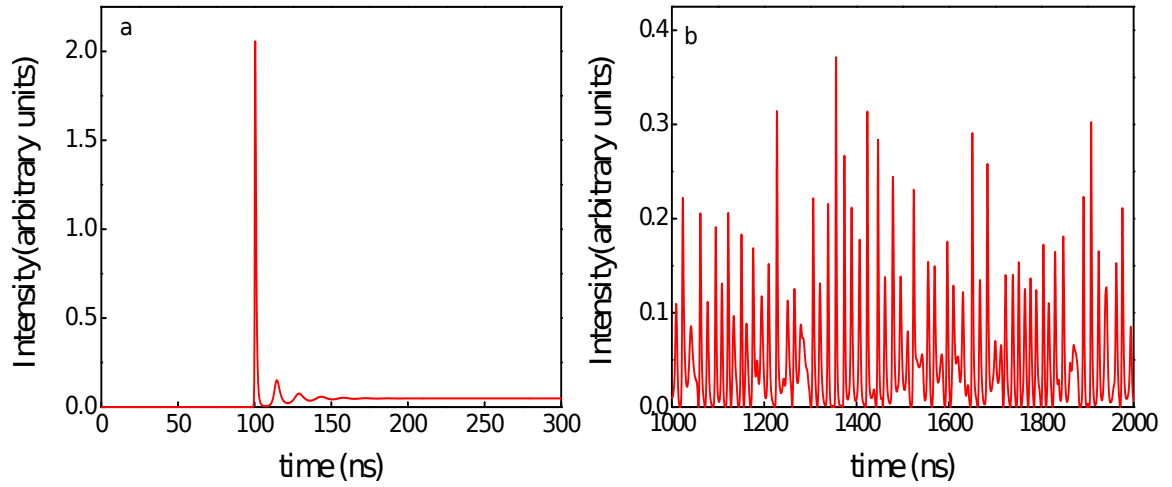


Figure 3.3: Steady state operation of QDL without feedback and chaotic operation when feedback is applied. $J = 125 A/cm^2$, delay is 200ps and feedback rate is $0.06 ps^{-1}$

tions are done using second order Runge-Kutta method and the output is sampled with a period $\Delta_s = 0.01 \cdot 2 \times 10^8$ points are used for the calculations. Figure 3.4 shows the graph of the four quantifiers discussed in previous sections for $\gamma = 0.18$ and $\tau = 66.66$. This delay value corresponds to 400ps in the original time scale. Relaxation oscillation period is approximately 89ps which scale to $\tau_{RO} \approx 14.83$. Figure 3.4a shows ACF as a function of the shift in time series. ACF does not have any vividly indicative feature near the value of τ , from which one can estimate the time delay involved in the feedback process. In contrast to ACF, all the other three quantifiers give an affirmative indication of the delay. For highly nonlinear systems like QDL with optical feedback, it is necessary to detect the nonlinear nonlocal time correlations in the output intensity time series if one wants to estimate the inherent delay in the time evolution of state variables. The ambiguity in delay estimation from ACF is attributed to the fact that it detect only linear correlations[92]. Figure 3.4b plot DMI with the inset graph showing the enlarged portion near the delay value. There is a pronounced peak near τ , which is slightly shifted to the right. This shift originate from the finite response time of the laser. The prediction of the response time beforehand is difficult and is an inherent property of the laser. Two less dominant peaks appear on both sides of the delay peak at $\tau \pm \tau_{RO}/2$. In the figure the peak on the lower side of τ is more dominant

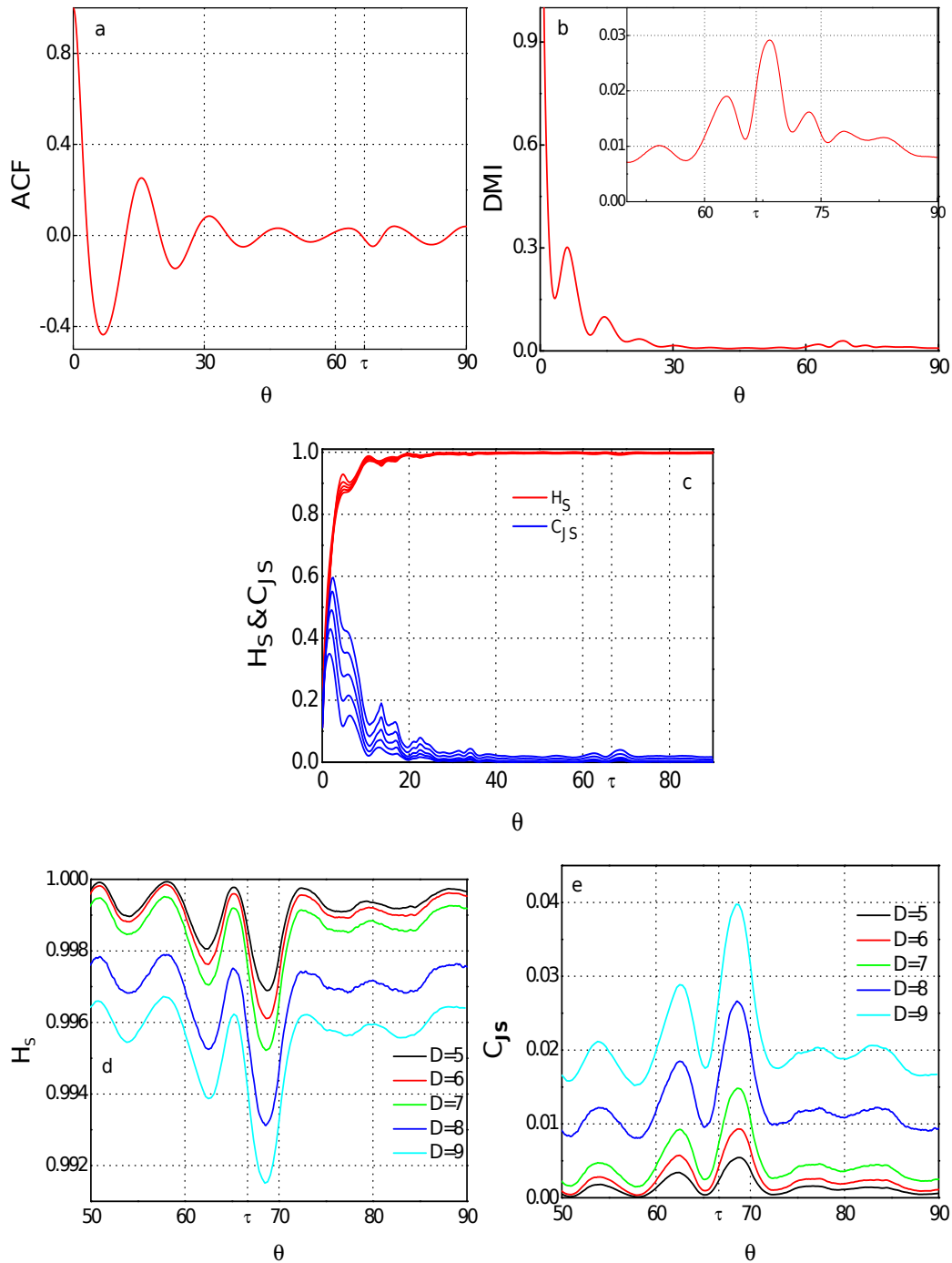


Figure 3.4: ACF, DMI, H_S and C_{JS} calculated from output intensity time series of QDL for $\tau = 400\text{ps}$ and $\gamma = 0.18$. For H_S and C_{JS} , D is varied from 5 to 9.

than the one on the higher side. The height of the delay peak as well as of the sidebands depends on the value of γ . This dependence is discussed later in this section. Figure 3.4c

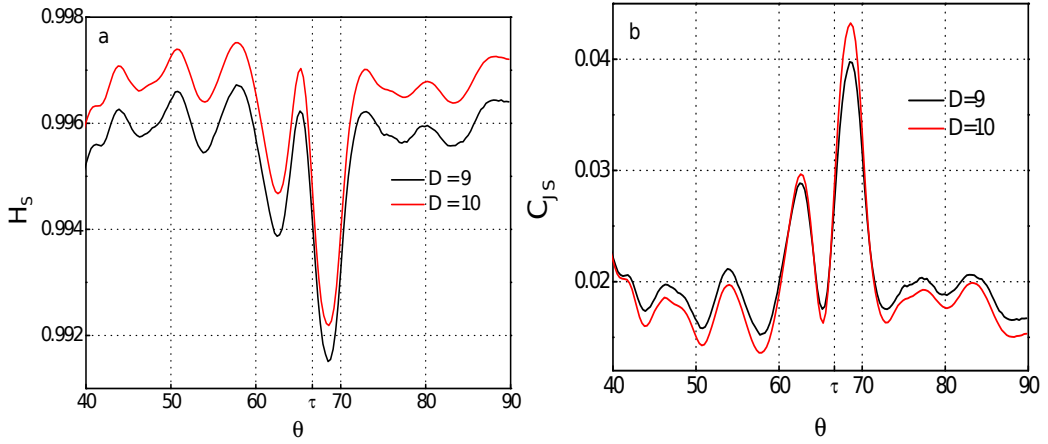


Figure 3.5: H_S and C_{JS} for D equal to 9 and 10. $\tau = 400ps$ and $\gamma = 0.18$

& 3.4e shows the plots obtained for H_S and C_{JS} for D values from 5 to 9. When the dynamics is reconstructed with a proper value of delay a minimum in entropy and a maximum in complexity are expected. 3.4c shows the plot of both the measures together. The more pronounced C_{JS} peak is visible in this plot, but it is difficult to spot the dip in H_S as its contrast from the baseline is low. The dip in H_S and the peak in C_{JS} near $\theta = \tau$ is evident from the enlarged graphs in figure 3.4d and 3.4e. Like DMI, delay estimation from both these measures suffer from the finite response time of the laser. Shift in the peak(dip) from the actual value of delay is found to be the same in all the three cases. In the complexity and entropy plots, the peak(dip) at $\tau + \tau_{RO}/2$ is suppressed while the one at $\tau - \tau_{RO}/2$ is visible. As the dimensionality of reconstruction increases the delay signature become prominent in both H_S and C_{JS} . But increasing D to 10 give a different result. In Figure 3.5 entropy and complexity are plotted for D equal to 9 and 10. For $D = 10$, H_S increases for all the values of θ reducing the contrast of the dip near τ . But C_{JS} peaks near $\theta = \tau'$ and $\tau' - \tau_{RO}'/2$ are enhanced. Interestingly, for other values of θ , $C_{JS}[D = 10]$ is less than $C_{JS}[D = 9]$. This shows that better delay retrieval using higher values of D is possible if one uses C_{JS} , even when the delay signature in H_S diminish. For higher values of D , we get the advantage that the background is minimized, and so better contrast. Next we perform the same calculations for $\tau \approx 33.33(200ps)$ keeping all other parameters constant. The results are given in

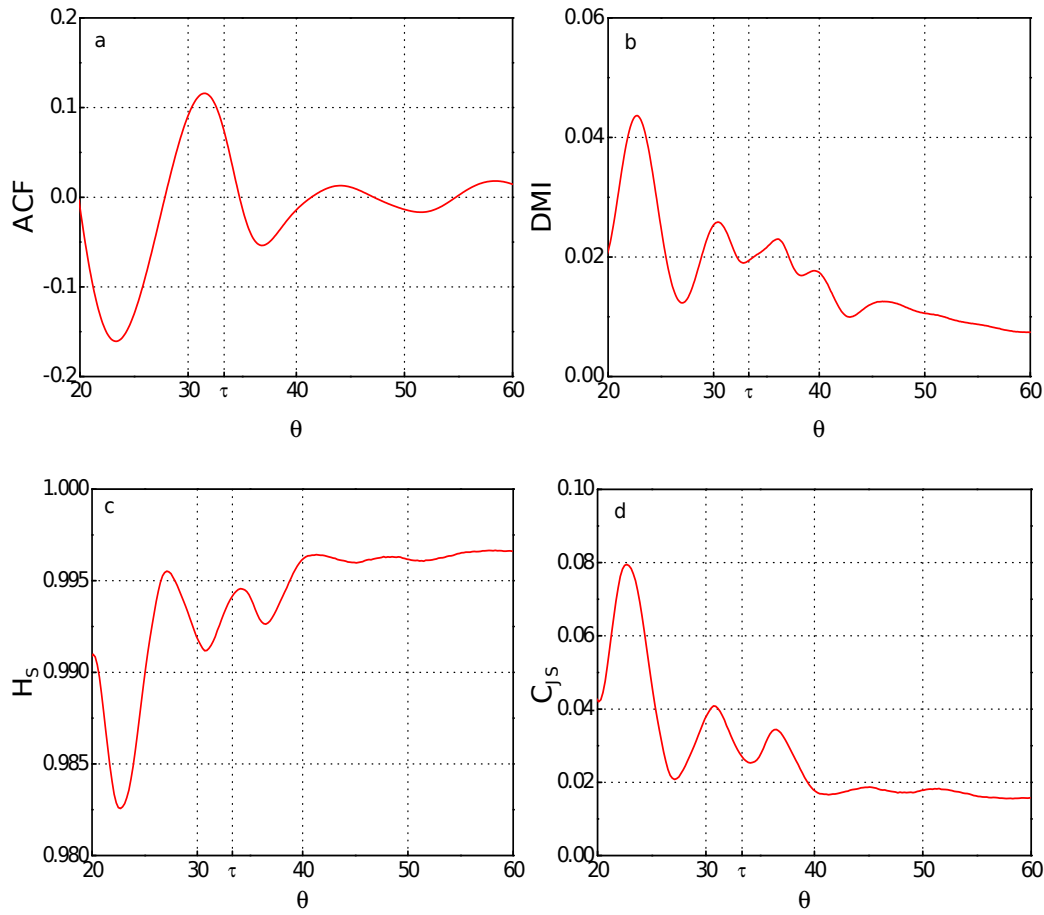


Figure 3.6: ACF, DMI, H_S and C_{JS} calculated from output intensity time series of QDL for $\tau = 33.33(200ps)$ and $\gamma = 0.18$. D is taken as 9 for H_S and C_{JS}

Figure 3.6. H_S and C_{JS} are plotted only for $D = 9$. Even with a closer scrutiny no affirmative feature indicative of delay can be spotted in any of the four plots. This reveals the practical impossibility of delay identification when the actual delay gets closer to the relaxation oscillation period. Numerous correlations exist in the QDL dynamics which die only long after the value of θ exceeds the value of τ . So when the delay gets closer to the relaxation oscillation period, the delay signature gets immersed in these correlations and a proper estimation becomes impossible. Finally we study the behavior of DMI and C_{JS} when feedback rate is varied. Figure 3.7a& b shows these quantifiers for six different values of γ . Delay is set to 66.66(400ps) in all the cases and the feedback rates are chosen such that the dynamics is in the coherence collapse regime. For both DMI and C_{JS} higher peaks are obtained for lower

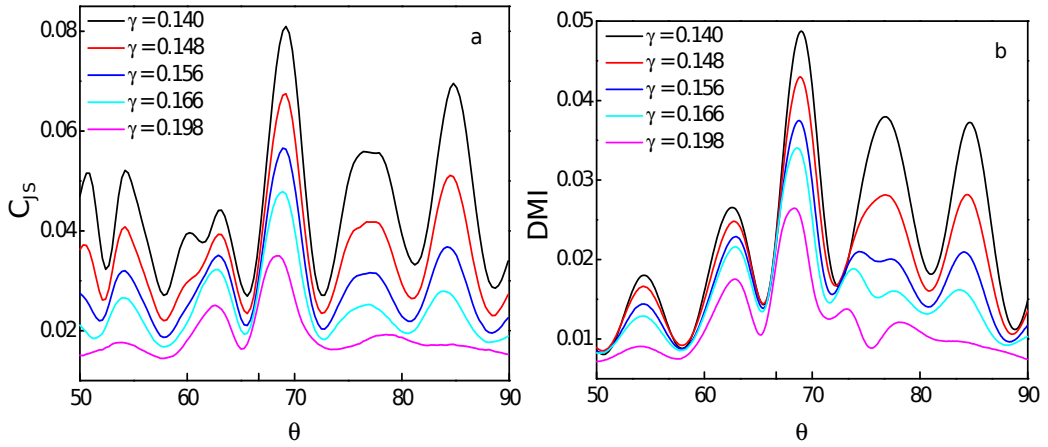


Figure 3.7: DMI and C_{JS} calculated for six different values of feedback rate(γ) with $\tau = 66.66(400ps)$

values of γ . In the figure highest peak is obtained for the value of γ equal to 0.14. But due to the pronounced nearby peaks, delay estimation can become ambiguous. As feedback rate increases the delay peaks reduce height but since the nearby peaks diminish faster, contrast from the baseline get enhanced. Especially for C_{JS} , peaks at $\theta > \tau$ get flattened. When feedback rate is high the delay estimation become more accurate because the shift due to the finite laser response time reduces and the peaks get more closer to the actual value of the delay. This happens identically for both DMI and C_{JS} .

3.8. CONCLUSIONS

We investigate the delay estimation scenarios from the time series using four quantifiers - namely Auto Correlation Function, Delayed Mutual Information, Permutation Entropy and Permutation Statistical Complexity. These numerical and information theoretical techniques are applied to the output intensity of a Quantum Dot Laser with optical feedback, which is operating in the coherence collapse regime. A Quantum Dot Laser shows many distinctive features in their dynamics when compared to the bulk or quantum well lasers. Conventional Lang-Kobayashi rate equation model cannot account for all these features adequately. Considering this fact we have carefully chosen a Quantum Dot Laser model from literature to simulate the delay dynamics. A detailed comparison of the proposed

measures is performed for different feedback rates and the delays. From the numerical calculations performed, we find Permutation Statistical Complexity to be the best candidate due to its distinctive maximum close to the delay. Also, we show that higher dimensionality of symbolic reconstruction will work with Permutation statistical complexity to get better contrast against the background as opposed to Permutation Entropy. Auto Correlation Function fails to give a distinctive identification unlike the other three measures. When the delay involved in feedback is close to the relaxation oscillation period of the laser delay identification become practically impossible with any of these techniques. Due to the finite laser response time all the measures have an error which give a slightly higher estimation of delay. For high feedback rates delay estimation become more accurate because the shift due to finite laser response reduces.

4

IDENTIFYING THE COMPONENTS IN THE DELAY DYNAMICS OF CURRENT MODULATED SEMICONDUCTOR LASERS

A close inspection of complex systems often reveal many interdependent processes that occur in different timescales. Resolving and understanding these timescales are essential for the proper modeling and prediction of their dynamics[80, 101]. Recent developments in this aspect of complex systems science provided examples where different numerical and information theoretical techniques could identify the component processes of complex dynamics[80, 88]. Delay estimation is an important subclass of this more general problem, where the focus is on identifying the delay signatures from the time series obtained by recording the values of at least one representative variable. Here the origin of delay is some sort of feedback mechanism present in the system as finite speed of information propagation always introduce a time lag in the feedback process. Some important works on this subject which are relevant to our results reported here are (a) time delay estimation in chaotic semiconductor lasers with optical feedback by Rontani et. al. making

use of Auto Correlation Function and Delayed Mutual Information [92] (b) the same problem is addressed by Soriano et. al. [80] using permutation entropy and permutation statistical complexity. With this approach, besides delay estimation they could also get clear indications of other time signatures like relaxation oscillations and picosecond pulsing (c) work of Zunino et. al. in which delay dynamics of Mackey-Glass system is explored using permutation-information theory[88]. Semiconductor lasers with optical feedback are particularly interesting systems because of its technological applications like high bandwidth modulation and encrypted chaotic communication[102–104]. Unlike many real world systems which exhibit complex dynamics but for which our control over the operating conditions or critical parameters is minimal, experiments with semiconductor lasers can be precisely controlled. This makes semiconductor lasers a favorite subject for investigations in dynamical systems. As mentioned earlier signatures of different inherent and induced processes can be extracted from the chaotic output time series of a semiconductor laser with optical feedback using numerical and information theoretical techniques. The fastest time scale is that of irregular picosecond pulsing which also is an indication of high dimensional chaos[80, 105]. The width of these pulses can have values around 100ps and have inter pulse separation less than 1 ns[105]. The relaxation oscillations typically fall into a few GHz range depending on the value of bias current. Time lag in the feedback process can range from a fraction of nanoseconds to a few nanoseconds. When relaxation oscillation period and delay are close it becomes extremely difficult to estimate the delay irrespective of the technique used[91]. In the present work we investigate a scenario where in addition to the feedback there is a periodic modulation of the bias current. From a more general point of view, this can be viewed as finding the timescales when an additional external periodic perturbation is present in the dynamics of the system. This is important because for complex systems prior knowledge of all the component processes and their time scales may not be available and there can be disturbances from hidden sources in unexpected ways. We analyze Auto Correlation Function(ACF), Delayed Mutual Information(DMI), Permutation Entropy(H_S), Permutation Statistical Complexity(C_{JS}) and Frequency spectra (FFT) computed on the intensity time series of SCL with delay feedback to find the timescales

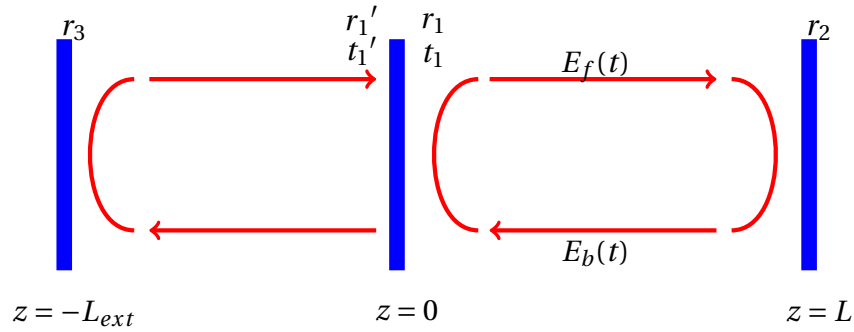


Figure 4.1: Schematic of semiconductor laser with an external cavity that constitute the delay feedback mechanism.

of the component processes. How these measures differentiate and resolve different processes for different delays and modulation frequencies are demonstrated and a detailed comparison is drawn.

4.1. SEMICONDUCTOR LASER WITH OPTICAL FEEDBACK : LANG-KOBAYASHI MODEL

Theoretical description of semiconductor laser dynamics with coherent optical feedback was developed by Lang and Kobayashi in 1980[55]. They put forward a delay differential system to explain experimentally observed phenomena like multistability and hysteresis in the presence of optical feedback. The rate equations of Lang-Kobayashi model is derived in this section[78]. Figure 4.1 shows the schematic of the laser diode with an external cavity which constitute the delay feedback mechanism. In the following discussions r and t represent reflection and transmission coefficients for the electric field amplitude and R and T represent reflection and transmission coefficients for the intensity. Laser cavity mirrors are located at $z = 0$ (mirror 1) and $z = L$ (mirror 2). The reflection and transmission coefficients of these mirrors for the waves inside the cavity are given by r_i and t_i , $i = 1, 2$. An external mirror is placed at $z = -L_{ext}$ (mirror 3). This mirror has reflection and transmission coefficients r_3 and t_3 respectively. For the waves traveling towards the cavity from mirror 3, the reflection and transmission coefficients at mirror 1 are r_1' and t_1' . Meaning of other symbols and terms are carried on from the second chapter. The round trip time in the ex-

ternal cavity, which is the delay involved in the feedback process, is given by $\tau = 2L_{ext}/c$. At any instant of time, the electric field coupled into the laser cavity from the external cavity ($t_1' E_{ext}(t)$) will have contributions from an infinite number of round trips in the external cavity, i.e.,

$$t_1' E_{ext}(t) = r_3 t_1 t_1' E_b(0, t - \tau) + r_3^2 r_1' t_1 t_1' E_b(0, t - 2\tau) + r_3^3 r_1'^2 t_1 t_1' E_b(0, t - 3\tau) + \dots + \frac{r_3^n r_1'^n}{r_1'} t_1 t_1' E_b(0, t - n\tau) \quad (4.1)$$

$E_b(0, t - n\tau)$ is the electric field amplitude at $z = 0$ at time $t - n\tau$. The reflection and transmission coefficients of the first mirror are related by the equations

$$t_1 t_1' = 1 - r_1^2 \quad (4.2)$$

$$r_1 = -r_1' \quad (4.3)$$

When the feedback is present, for calculating the field of the forward traveling wave at $z = 0$ the contribution due to the field transmitted from the external cavity is to be added. So equation 2.8 is modified as

$$E_f(t) = G_1 \exp(i\omega_{th}\tau_{in}) E_f(t - \tau_{in}) + \frac{r_1^2 - 1}{r_1^2} \sum_{n=1}^{\infty} (-r_1 r_3)^n E_f(t - n\tau) + F_E(t) \quad (4.4)$$

Proceeding in a similar way as the rate equations are derived in the second chapter, one can see that the time evolution of the complex amplitude of the electric field is $E(t)$ can be written as

$$\frac{dE}{dt} = \frac{1 + i\alpha_l}{2} [G(N, |E|^2) - \gamma_p] E(t) + \frac{1}{\tau_{in}} \frac{r_1^2 - 1}{r_1^2} \sum_{n=1}^{\infty} (-r_1 r_3)^n E(t - n\tau) + F_E(t) \quad (4.5)$$

In Lang-Kobayashi model only the first term in the summation is considered, meaning

the contribution of multiple reflected waves from the external cavity is neglected. This is a good approximation if the reflection from the external mirror is weak or the laser facet is antireflection coated. The feedback parameter γ is defined as

$$\gamma = (1 - r_1^2) \frac{r_3}{r_1} \quad (4.6)$$

The equation describing the carrier dynamics is unaffected by the presence of optical feedback. Taking into account these factors and assuming that the noise correlation time is much shorter than the carrier and photon decay times, final rate equations describing the dynamics in the presence of coherent optical feedback can be written as

$$\frac{dE}{dt} = \frac{1 + i\alpha_l}{2} [G(N, |E|^2) - \gamma_p] E(t) + \frac{\gamma}{\tau_{in}} E(t - \tau) + F_E(t) \quad (4.7)$$

$$\frac{dN}{dt} = \frac{1}{\tau_s} \left(p I_{th} - N - \frac{N - \delta}{1 - \delta} P \right) \quad (4.8)$$

where p is the pumping factor. Relaxation oscillation frequency Ω_R of the laser, calculated from the rate equations without feedback, is given by

$$\Omega_{RO} = \frac{1}{2\pi} \sqrt{\frac{G_N I_{th} (p - 1)}{q}} \quad (4.9)$$

4.2. SIMULATION AND RESULTS

4.2.1. COMPARISON OF THE QUANTIFIERS FOR LANG-KOBAYASHI MODEL

Before introducing modulation in the pump current, we compare the quantifiers calculated for Lang-Kobayashi model with constant pump. Two different operating conditions are considered, $p = 1.06$ and $p = 1.55$. Fig. 4.2 shows the chaotic time series and the plots obtained by applying five different techniques, FFT, ACE, DMI, H_S and C_{JS} to the chaotic time series for $p = 1.05$, at which Ω_{RO} is calculated to be 1.31GHz. Delay is 1.2ns and γ is 10GHz. From Fig. 4.2b, it can be seen that the dominant peak in the spectrum is at 0.85GHz, corresponding to a time period of 1.18ns, which is approximately equal to the

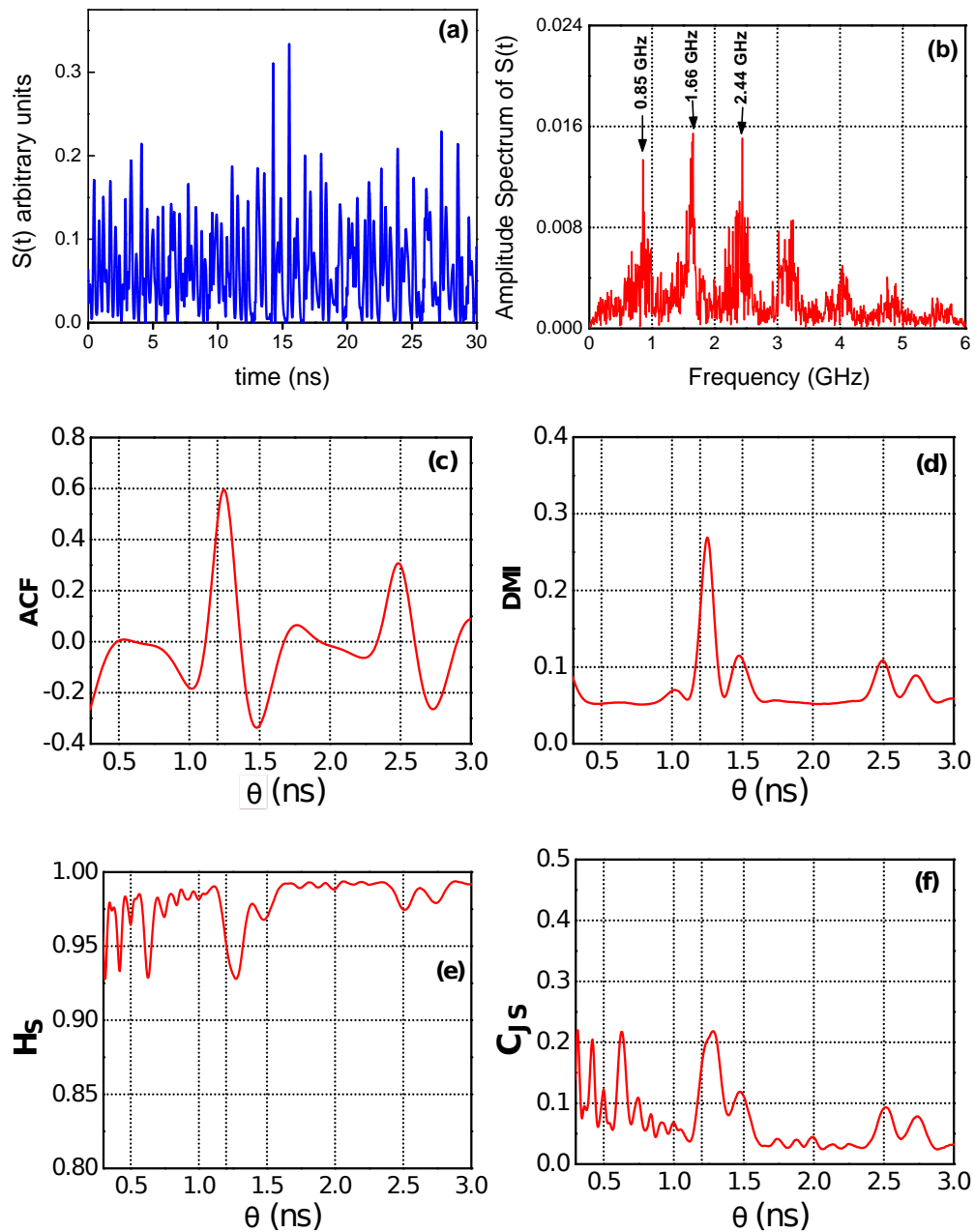


Figure 4.2: Time series, FFT, ACF, DMI, H_S and C_{JS} for $p=1.05$, $\gamma = 10$, $\tau = 1.2ns$ when there is no modulation present.

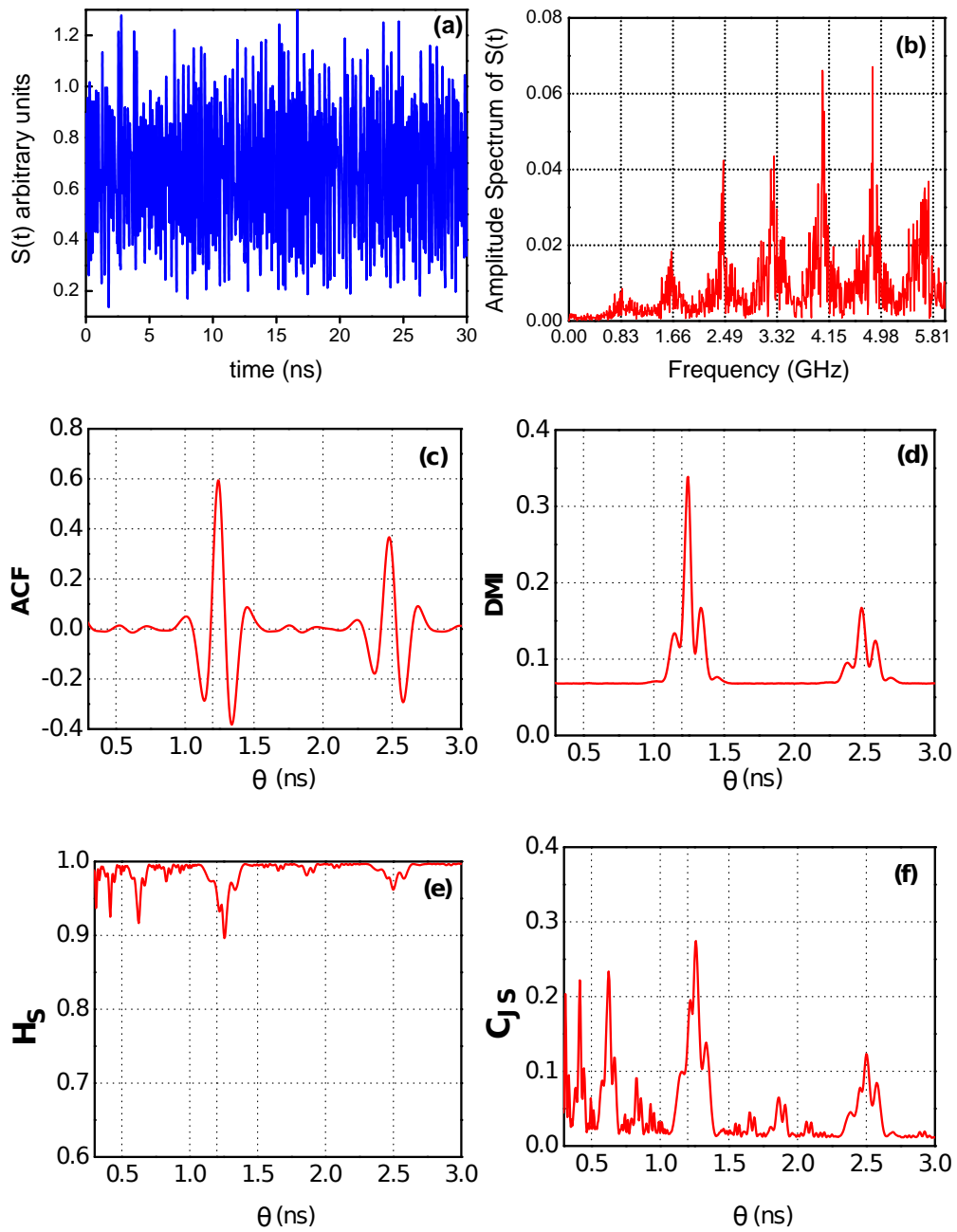


Figure 4.3: Time series, FFT, ACE, DMI, H_S and C_{JS} for $p=1.55$, $\gamma = 10GHz$, $\tau = 1.2ns$ when there is no current modulation.

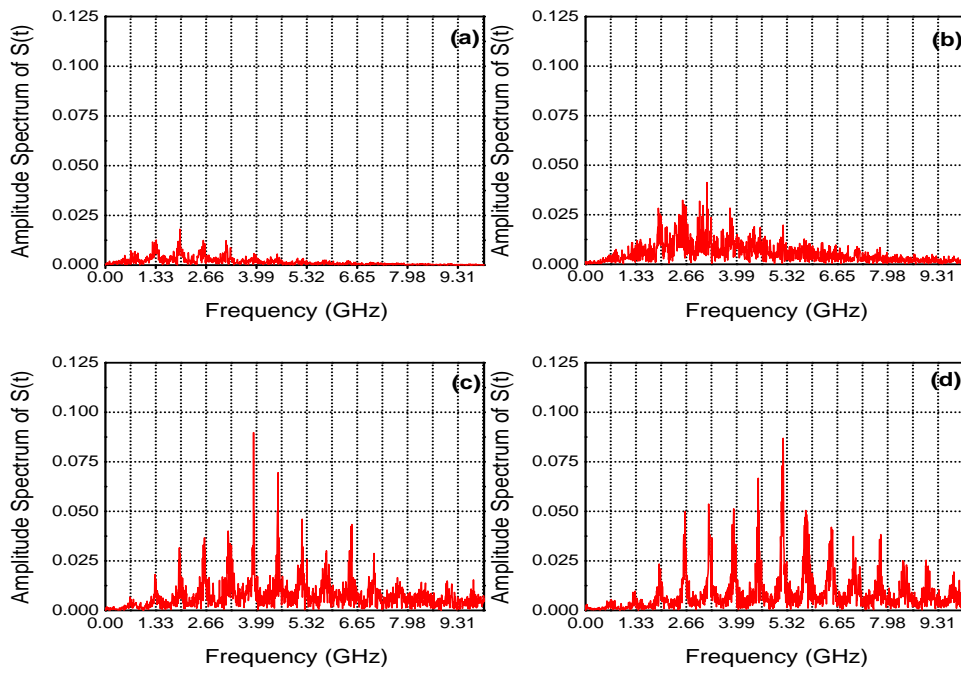


Figure 4.4: Spectra of chaotic time series of SCL output obtained without current modulation when $\tau = 1.5ns$, $\gamma = 10GHz$. (a),(b),(c) and (d) correspond to p values in the order 1.06,1.25,1.55 and 1.75.

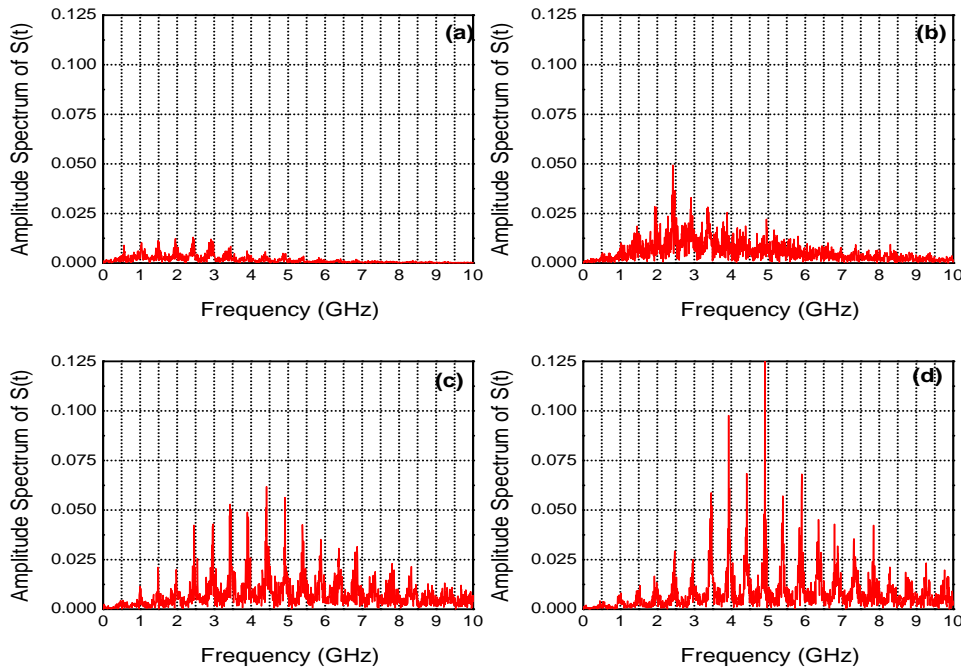


Figure 4.5: Spectra of chaotic time series of SCL output obtained without current modulation when $\tau = 2ns$, $\gamma = 10GHz$. (a),(b),(c) and (d) correspond to p values in the order 1.06,1.25,1.55 and 1.75.

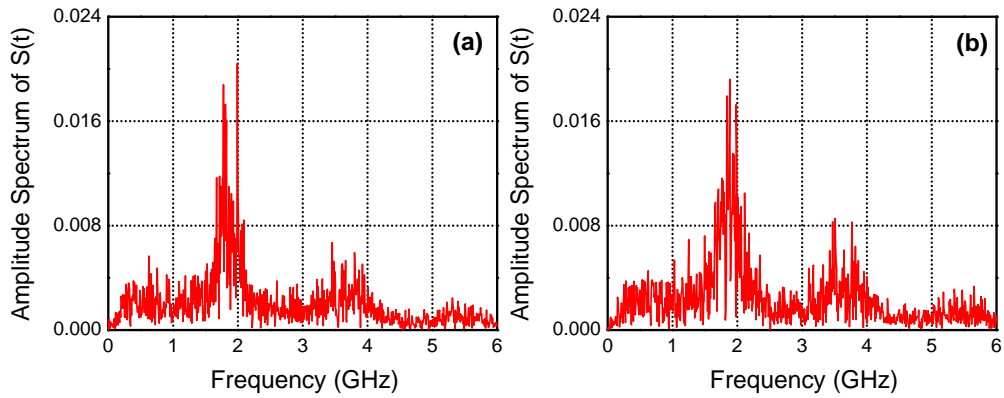


Figure 4.6: Spectra of the chaotic SCL output when $\tau < \tau_{RO}$. (a) $\tau_{RO} = 0.75ns$ and $\tau = 0.5ns$ (b) $\tau_{RO} = 0.69ns$ and $\tau = 0.5ns$

feedback delay in the laser. The peaks repeat at 1.66GHz and 2.44GHz which are close to the multiples of 0.85GHz. The same trend can also be observed in the spectrum in Fig. 4.3b where value of p is 1.55. Here the grid lines are drawn at multiples of 0.83GHz. The peaks are not equally spaced, but as frequency increases tend to occur at shorter separations. This behavior becomes visible near to Ω_{RO} which is equal to 4.38GHz in this case. For detailed investigation we plot FFTs with different pump currents and delay values. Fig.4.4 and Fig. 4.5 depict FFTs for feedback delays 1.5ns and 2ns respectively and for each value of τ , four pump factors (p) are chosen - 1.06,1.25,1.55 and 1.75. Ω_{RO} s for these values of pump currents in the given order are 1.44GHz, 2.95GHz, 4.38GHz and 5.11GHz. In Fig. 4.4 grid lines are drawn at multiples of 0.67GHz which give a time period equal to 1.5ns. The graphs reveal that the locations of the peaks are unchanged as the pump current and thereby the relaxation oscillation frequency are increased. But the relative strength of these frequency components change as the relaxation oscillation frequency is changed. A close observation shows that the most dominant components in the spectra are always close to the relaxation oscillation frequency. Again it can be seen that close to the relaxation oscillation frequency the peaks begin to occur at shorter separations. These observations hold also in Fig. 4.5 where the frequency corresponding to the period equal to feedback delay is 0.5GHz. From these observations we conclude that the peaks upto the relaxation oscillation frequency in the spectrum give a good estimate of the delay present in the system. This result can

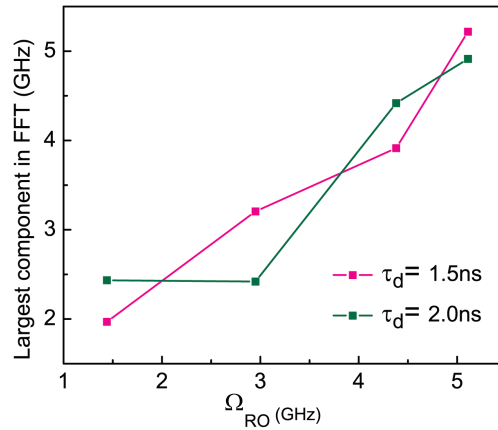


Figure 4.7: Graph of relaxation oscillation frequency vs. the largest component in the spectrum

be connected with the findings in [91] where they showed that when relaxation oscillation period is close to the delay, estimation of delay from output time series become extremely difficult using *ACF* or *DMI*. We look into this scenario by calculating FFTs when $\tau < \tau_{RO}$. In Fig. 4.6 two FFTs are shown for τ_{RO} values 0.75ns (a) and 0.69ns (b) while keeping τ at 0.5ns. In both cases the peaks are near to 2GHz which is the indication of the delay feedback process. This can be due to the strengthening of the periodic orbits of which the period or its multiples matches with that of the feedback delay. In Fig.4.6 a sharp peak exactly at 2GHz is present with a broader and slightly smaller shifted peak to the left. Fig.4.6b shows the peak at a slightly lower frequency value indicating a higher feedback delay value. The significance of this result is that delay signature can be observed with FFT while it is difficult to estimate it from *ACF* and *DMI*.

Fig. 4.7 shows the plot of the relaxation oscillation frequency vs. the largest component in the FFT. A linear relationship between these two shows the effect of relaxation oscillations on the peaks of the spectra and confirm the previously made observation that the highest component in FFT is always closer to the relaxation oscillation frequency.

In Fig. 4.2 and 4.3 *ACF* and *DMI* has clear and distinctive peaks at the delay value. In the *DMI* plot, smaller peaks appear on both sides of the delay peak. It can be seen that these peaks come closer in Fig. 4.3d compared to Fig. 4.2d . Evidently these peaks are the signatures of relaxation oscillations because for Fig.4.2d corresponds to a lower value of Ω_{RO} consequently a higher relaxation oscillation period. H_S and C_{JS} plots pick many correla-

tions from the time series that are absent in ACF or DMI. The dips(peaks) at $\tau, \tau/2, \tau/3$ and $\tau/4$ can be identified from Fig. 4.2e& f as well as from 4.3e & f. This property of Entropy and Complexity are very helpful when the correlations are very weak. In the case of Quantum Dot Laser the correlations in the output intensity series are weak because of the low sensitivity of Quantum Dot Lasers to feedback[27, 29, 106] as discussed in the third chapter. In that case only H_S and C_{JS} detected the delay feedback process. Bulk semiconductor lasers are more sensitive to delay feedback and so the information theory measures detect many more correlations.

Delay signature in the spectra posses one important difference when compared with other measures. All the measures except FFT produce a delay indication at a slightly higher value than the actual delay present in the system. In the case of FFT, the frequency component arising from the feedback delay can occur at higher, lower or exact value of the delay, for different parameter values. In Fig. 4.2 the actual value of τ is 1.2ns while the peak from the spectrum give 1.18ns which is less than τ . In Fig. 4.4c & d as well as on 4.5c & d, the initial peaks in the spectra occur exactly at τ and its multiples. Finally, in Fig. 4.6, the actual value of τ is 0.5ns, but the peak in the spectra gives a frequency less than 2GHz, which indicate τ is greater than 0.5ns.

4.2.2. EFFECTS OF CURRENT MODULATION

Fig. 4.8 shows the graphs of the quantifiers for different values of modulation frequency (Ω_m). Here the pumping factor is fixed at 1.05 and the modulation depth(m) at 0.05. Feedback rate and delay are 10GHz and 1.2ns respectively. In all the graphs the value of delay is indicated by an unlabeled dotted vertical line. Each row in the figure corresponds to the plots for a particular value of Ω_m . Ω_m is normalized to the relaxation oscillation frequency (Ω_{RO}) and the values chosen for Ω_m are 0.7,0.8,1.0,1.2 and 1.4 respectively. For these values the modulation periods(τ_m) are respectively 1.07,0.94,0.75,0.62 and 0.53 nanoseconds and the corresponding frequency values in GHz are 0.93,1.06,1.33,1.61 and 1.88. Relaxation oscillation frequency Ω_{RO} of the free running laser at $p = 1.05$ is 1.33GHz which corresponds to a period of 0.75ns. All the measures are shown for reconstruction delays(θ) from 0.35ns

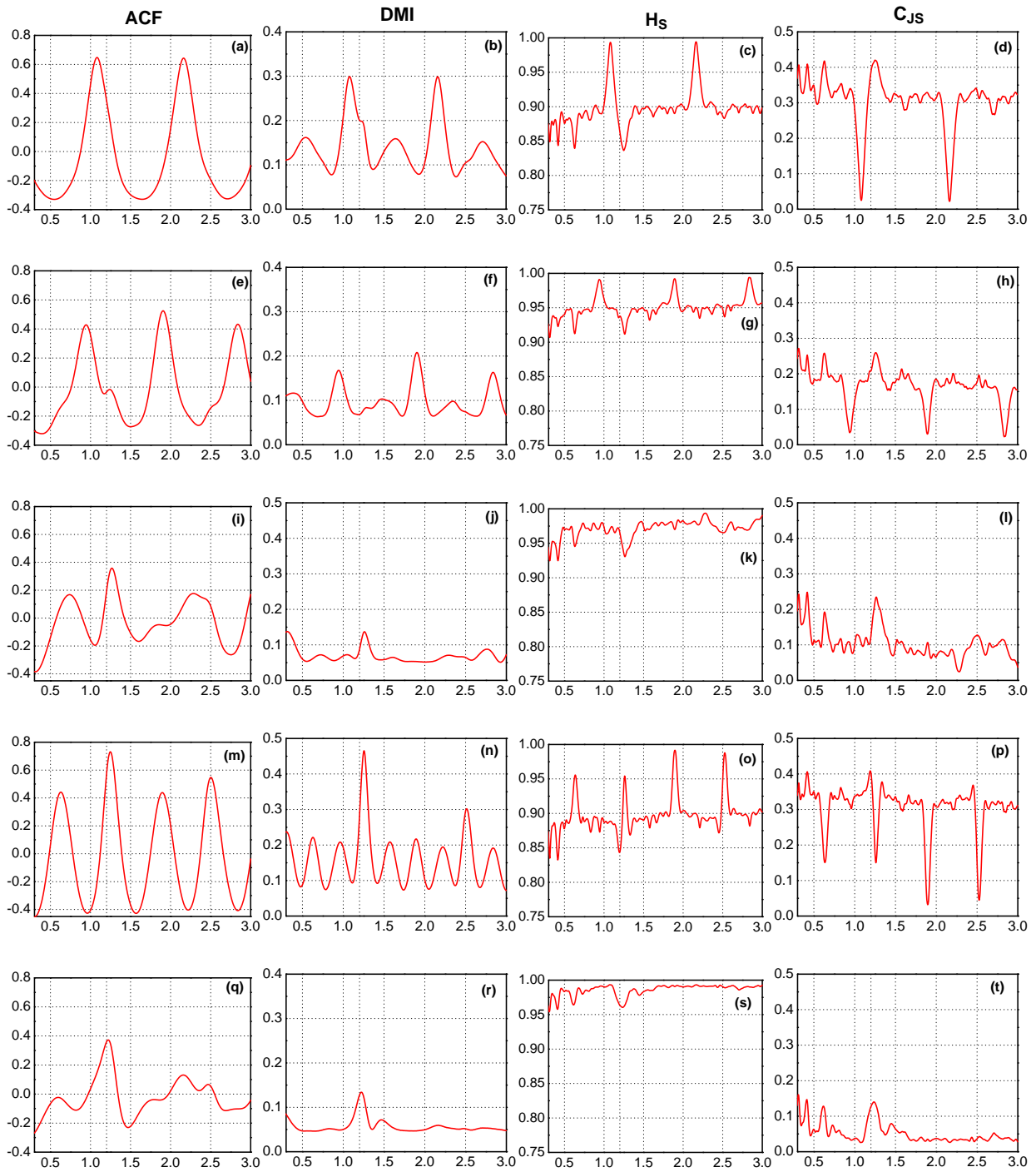


Figure 4.8: ACF, DMI, H_S and C_{JS} computed for different values of Ω_m at $p=1.05$. The rows from top to bottom correspond to Ω_m values 0.7,0.8,1,1.2,1.4 respectively. Other parameters are $\gamma = 10GHz$, $\tau = 1.2ns$ and $m = 0.05$. For ACF and DMI plots x axis represent the time shift and for H_S and C_{JS} x axis represent delay of reconstruction, both represented by θ

to 3ns. In this range one can look for the indications of three different processes in the quantifiers - Relaxation oscillations at 0.75ns, delay feedback at 1.2ns and modulation at the value chosen for Ω_m . Correlations arising from picosecond pulsing appears for values smaller than 0.35ns and the effect of modulation on those correlations is discussed later. Fig. 4.8a-d depict the quantifiers for $\Omega_m = 0.7$. It can readily seen that only the modulation process has got reflected in ACF. Broad and clear peaks are present at τ_m (1.07ns) and $2\tau_m$ (2.14ns). Other time signatures are completely absent. In DMI more features are visible, but peak at the modulation period is the most dominant and the only affirmative one. Entropy and complexity shows more resolved features compared to ACF and DMI. When delay of reconstruction (θ) is proper, the reconstructed time series appear more structured and consecutively there occur a reduction in entropy and an increment in complexity. But for other values of θ the reconstructed time series appear to be random and entropy maximizes and complexity minimizes. So when the delay of reconstruction equals the delay of feedback in the system, a dip in entropy and a peak in complexity are expected. This is what we find in Fig. 4.8c& d, but the dip in H_S and the peak in C_{JS} occur at slightly higher value θ . This is due to the finite response time of the laser and its value can depend on the parameters of the system as discussed in the third chapter. From a detailed literature survey on this subject, it seems that irrespective of the technique used, such a shift is always present in delay estimation from chaotic time series. Though we have shown examples in the previous section where exact estimation of delay is possible from the spectra, that is not the case always. This happens only for certain combination of τ and other parameter values, and cannot be predicted in advance. Unlike ACF and DMI, the delay signature and the correlation arising from modulation are resolved in H_S and C_{JS} . In addition to that, these two correlations are reflected in different ways in the information theory measures. At the value of τ_m the behavior of H_S and C_{JS} are reversed from that at τ . A dominant peak in H_S and a dominant dip in C_{JS} are present at τ_m . A minimum in complexity and a maximum in entropy indicate a completely random dynamics without any structure in the time series. This is exactly opposite to the results at τ where the results indicate a complex dynamics with complex structures hidden in the time series. This shows that when infor-

mation theory measures are calculated from time series choosing a proper value for delay of reconstruction is very critical. A slight change in its value may give completely different results as in the case shown here. The results also shows that H_S and C_{JS} can resolve processes that occur in very close timescales and for the same reason are not resolvable in ACF or DMI.

Now, we increase the value of Ω_m gradually and study how the quantifiers change. In the figure 4.8, second row to fifth corresponds to values of Ω_m respectively to 0.8,1,1.2 and 1.4. The indication of feedback process becomes dominant in ACF and DMI only for $\Omega_m \geq \Omega_{RO}$. At $\Omega_m = \Omega_{RO}$ the delay peak in DMI has a minimal background, making delay estimation clear and straightforward. Also, in H_S and C_{JS} the effect of modulating frequency is gradually reduces as Ω_m is increased to Ω_{RO} . One important difference is that irrespective of the value of Ω_m delay indications are always present in H_S and C_{JS} . At $\Omega_m = 1.2$, twice the modulation period become close to feedback delay. In fig. 4.8m & n, these two factors add up at τ to give enhanced peaks for ACF and DMI. On the other hand, delay signature is diminished in H_S and C_{JS} (4.8m & n), since the modulation and delay feedback are resolved. When Ω_m is increased to 1.4, all the quantifiers show dominant signatures of the delay feedback mechanism and the signatures of other processes disappear. ACF peak is broad but affirmative because of substantial reduction in the background. DMI gives the most obvious result at $\theta = \tau$, with a flat background. In H_S and C_{JS} , other than the dominant dip(peak) at τ , one can find less dominant dips(peaks) at $\tau/2$ and $\tau/3$.

Fig. 4.9 shows the spectra of the chaotic time series for the five sets of parameter values considered above. For $\Omega = 0.7$ & 0.8 , the modulation frequency and its higher harmonics have dominant peaks in the spectra. Delay indications are highly suppressed in these cases. At $\Omega_m = 1$, which means the modulation frequency is equal to the relaxation oscillation frequency, the higher harmonics in the spectra diminishes and the delay indication emerges at 0.85GHz which approximately give the period of 1.2 ns. This is in accordance with ACF and DMI, where delay signature is evident only when Ω_m is increased to 1. At $\Omega_m = 1.2$ there is a dominant peak at the modulation frequency, but higher harmonics are absent and delay signature is weak. When Ω_m is increased to 1.4, the strength of the modulation

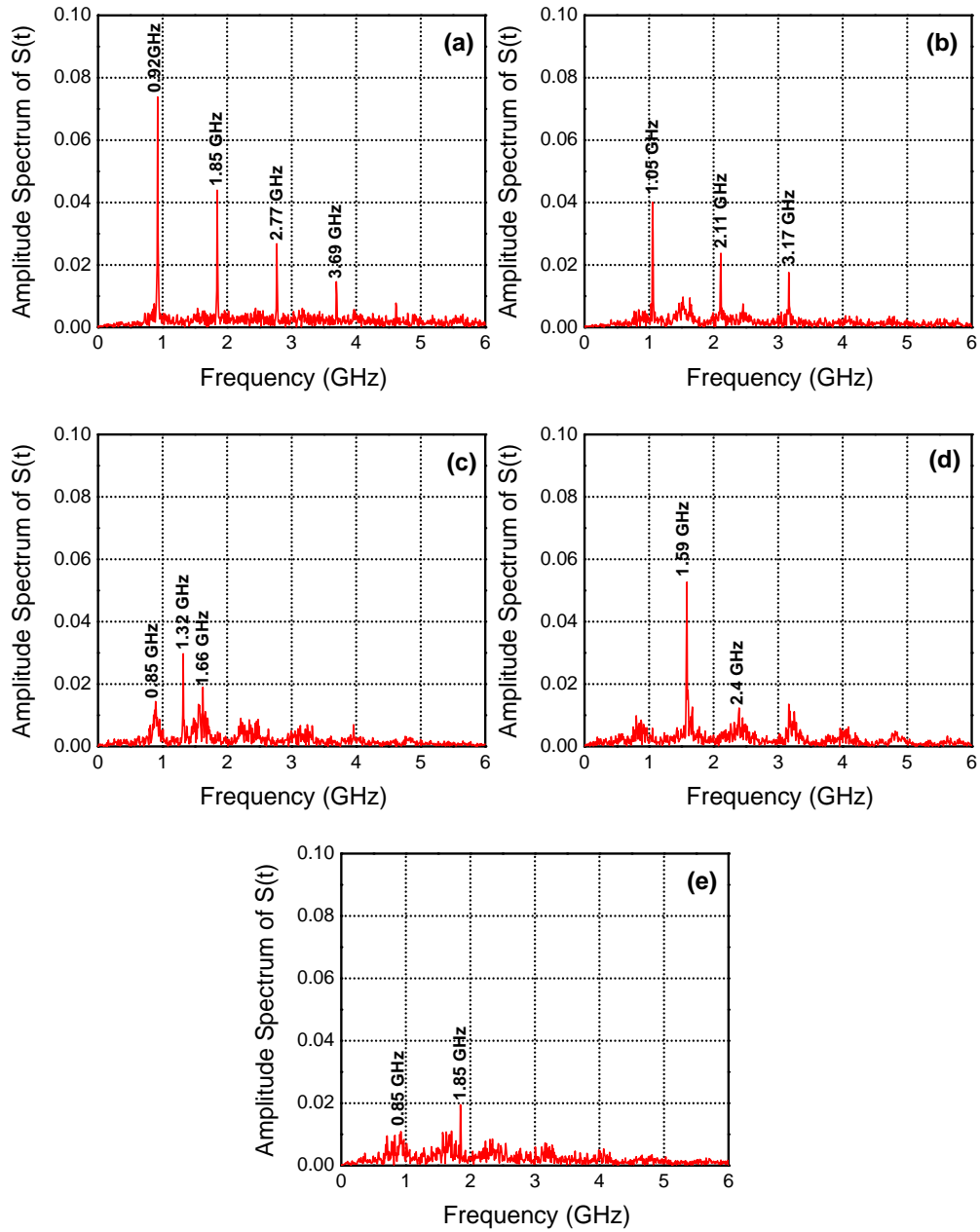


Figure 4.9: Spectra of the SCL chaotic output corresponding to the graphs given in 4.8. (a) $\Omega_m = 0.7$ (b) $\Omega_m = 0.8$ (c) $\Omega_m = 1.0$ (d) $\Omega_m = 1.2$ and (e) $\Omega_m = 1.4$.

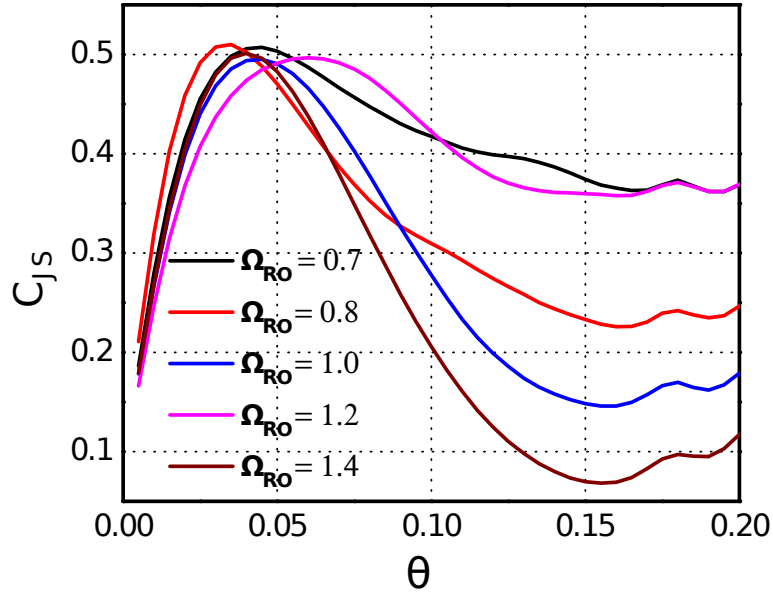


Figure 4.10: C_{JS} calculated for small values of embedding delays and for different values of Ω_{RO} . The first peak represent the minimum sampling time required to preserve all the correlations.

components drop substantially as is the case with the other quantifiers.

The curves in Fig. 4.10 depict the behavior of C_{JS} for small values of embedding delays and for all the values of Ω_{RO} considered in the above discussion. In all the cases the curves reach a maximum at an intermediate value of embedding delay and then drop again. As discussed in [80], this value of delay (τ_M) indicate the time scale of the fastest component process in the dynamics. This is attributed to the phenomenon of picosecond pulsing, which occur in faster timescale than the relaxation oscillations. τ_M determine the minimally required sampling rate which preserve all the nonlinear correlations occurring in the chaotic dynamics. From Fig. 4.10, we find that the value of τ_M is affected by the modulation process. τ_M is minimum when $\Omega_m = 0.8$ and then increases with increase in Ω_m . Again, when the Ω_m reaches 1.2, τ_M reaches a maximum and reduces with further increase in Ω_m . Even though the underlying mechanism is not evident here, this result clearly demonstrate how the presence of a periodic perturbation in the system alter the minimum sampling rate for loss less reconstruction of the system dynamics. In Fig. 4.11 the quantifiers calculated for $p = 1.26$ and in the presence of modulation are plotted. Here γ and τ are kept unchanged as in the previous discussions, respectively to 10GHz and 1.2ns. The graphs in

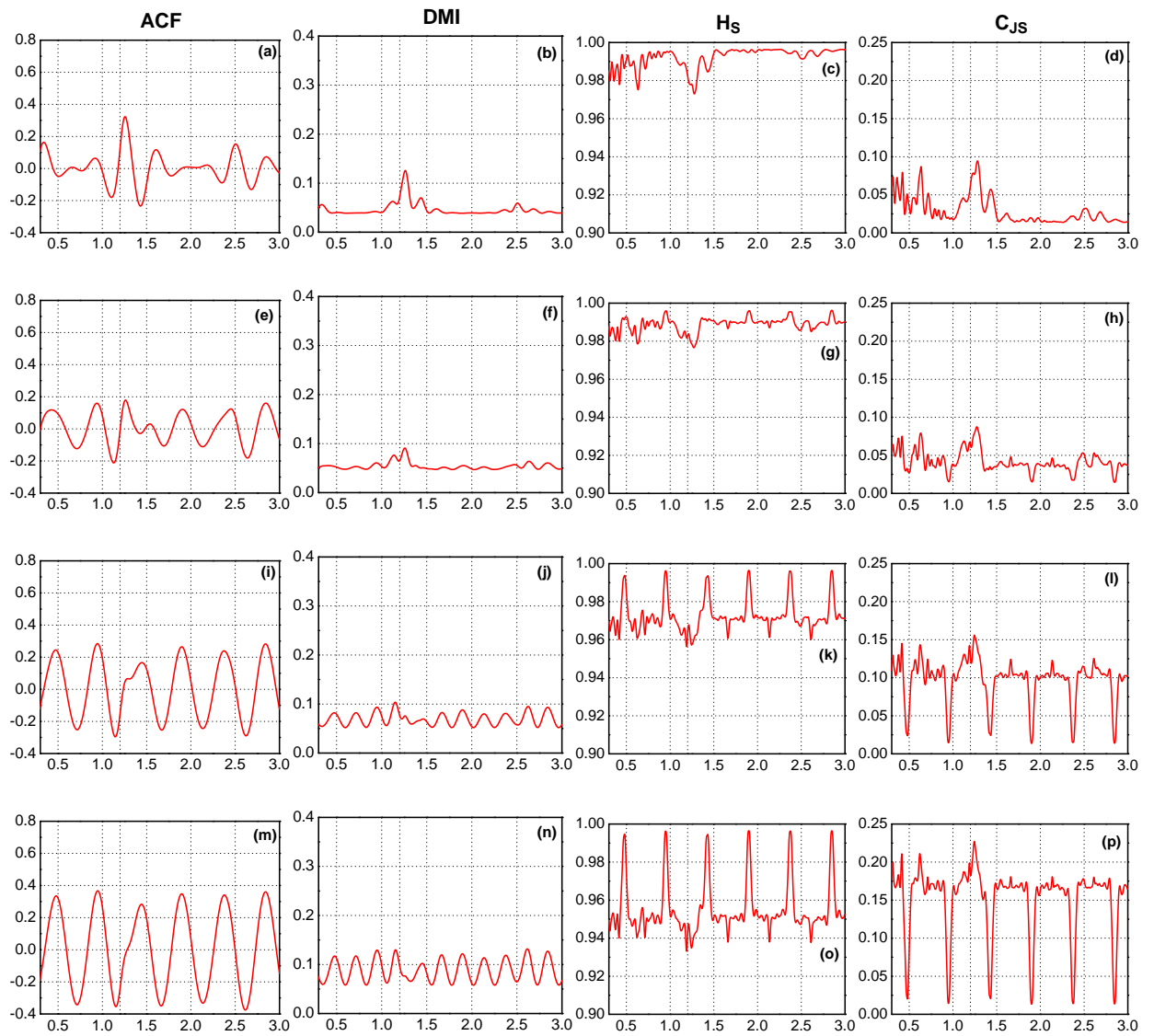


Figure 4.11: ACF, DMI, H_S and C_{JS} computed for different values of modulation strength(m) at $p = 1.26$. The rows from top to bottom correspond to m values 0,0.05,0.08,0.1 respectively. Other parameters are $\gamma = 10\text{GHz}$, $\tau = 1.2\text{ns}$ and $m = 0.05$. For ACF and DMI plots x axis represent the time shift and for H_S and C_{JS} x axis represent delay of reconstruction, both represented by θ

the first row are calculated from the chaotic time series of the LK model without any current modulation. The delay signatures as well as the side bands created by the relaxation oscillations are evident in all the four measures. In additions dips in entropy and peaks in complexity appear corresponding to $\tau/2$ and $\tau/3$. 2nd to 4th rows in Fig. 4.11 corresponds to m values 0.05, 0.08 and 0.1. Modulation process dominate in ACF for all values of m . At $m = 0.5$, DMI still produce a peak closer to 1.2ns, but highly diminished when compared to $m = 0$. With further increase in m , correlations arising from delay get completely submerged in the periodic correlations arising from the modulating frequency. The effect of modulation process manifest as peaks in entropy and the height of these peaks increases when modulation strength is increased. The dominance of delay indication in entropy diminishes with increase in modulation strength. Irrespective of the value of modulation depth a comparatively distinct delay peak is present in complexity for all values of m . Like H_S , in C_{JS} also the periodic correlations arising from modulation, get dominant for higher values of m , which in this case appear as dips.

4.3. CONCLUSIONS

Our results indicate that understanding and resolving component processes of complex dynamics from the time series of its observable variables is not trivial. Often a single approach to the problem may not give desired output. In the presented work, we applied different numerical and information theoretical techniques to the output intensity of a semiconductor laser with delay feedback. Different approaches to the same problem proved advantageous and most often essential to draw meaningful and more accurate conclusions. Special attention has been given to delay estimation from the simulated chaotic output of Lang-Kobayashi model, which has been the most successful model in predicting the semiconductor laser dynamics in the presence of coherent optical feedback. A detailed account of the delay calculation from the spectra of the chaotic intensity time series is presented. Also Auto-Correlation, Mutual Information, Entropy and Complexity measures are employed and how different internal and external processes of the semiconductor laser get

reflected in these measures are discussed. These methods are again applied when a periodic modulation is given to the bias current of the laser. We find that Information theory measures resolve and distinguish the delay feedback and modulation processes much better than other methods. Finally we show how the minimum sampling rate required for the loss less reconstruction of the intensity time series depend on the modulation frequency. To check the reliability of the different techniques and the results, calculations are always done with time series generated with different operating conditions of the laser.

5

SUMMARY

For last some decades semiconductor lasers have been key components in many applications like optical fiber communications, data storage and material processing. For most of these applications the laser need to be operated in a stable regime. In the initial phases of the development of semiconductor lasers the instabilities arising due to the backreflection from the external optical components were seriously investigated in order to minimize them. Later developments suggested that these instabilities, arising from self coupling or feedback phenomena, can be useful in many ways. In this thesis we investigate the role played by delay in the feedback mechanism, in producing different types of semiconductor laser dynamics.

The first chapter is dedicated to providing an introduction to the basics of semiconductor lasers and delay systems. We also discuss some of the interesting phenomena reported in semiconductor lasers with different types of feedback. In the following chapter, we do the stability analysis of the Delay Differential Equations that describe the dynamics of Semiconductor Lasers with optoelectronic feedback. We compute the critical delay curves in the Feedbacks strength-delay parameter space and simulate the delay differential equations of the system to show the Hopf bifurcations. Our results suggest that linear stability

analysis of nonlinear delay differential equations can show more complex behaviour compared to linear delay differential equations. We compute the stability islands of the fixed point in the Feedback strength-delay parameter space and show how they reshape, merge and disappear with changes in nonlinear gain reduction factor or bias current. Bistability exhibited by the system is studied by giving different physically meaningful initial conditions. We identify two type of bistable regions in Feedback strength-delay parameter space. In the first type of bistability, the system goes to a fixed point when the initial condition is a constant function and goes to an oscillatory state when the initial function is oscillatory. In the second type, the system goes to a fixed point if the initial function is oscillatory and goes to oscillatory output if the initial condition is a constant function. Here the constant function is the output of the laser without feedback, and the oscillatory initial condition is the laser output before the relaxation oscillations die out.

In the third chapter, we analyze the output of a Quantum Dot Laser with optical feedback using different methods. Quantum Dot Lasers have superior performance characteristics compared to other type of semiconductor lasers. We choose a proper model of Quantum Dot Laser with optical feedback from existing literature and simulate the dynamics. Computing Auto Correlation Function, Delayed Mutual Information, Permutation Entropy and Permutation Statistical Complexity on the output time series, we show how the value of delay taken for feedback can be retrieved. A comparison of the delay estimation for Quantum Dot Lasers and that of bulk Semiconductor Lasers shows that for Quantum Dot Lasers the delay signatures obtained with different measures are very weak. Also these signatures disappear very fast when the delay become closer to relaxation oscillation period. In chaos based optical secure communications, the security depends on the level of difficulty in retrieving the delay value from the chaotic laser output. So use of Quantum Dot Lasers in such communication systems can increase the layer of security. We also investigate how the delay estimation scenario changes if the operating conditions of the Quantum Dot Laser are changed.

In the last work, we employ different methods to unravel the timescales of different processes that contribute to the complex dynamics of a semiconductor laser with coherent

optical feedback and current modulation. Different techniques reflect different aspects of the laser dynamics and which also change with the change in feedback rate, delay, modulation strength and modulation frequency. We present our results by comparing five different techniques calculated on the output time series of the semiconductor laser. Interestingly, we find that information theory measures differentiate delay feedback and modulation processes in addition to giving indication of the timescales of these processes. We apply different tools on the time series obtained from the simulation for a wide range of parameter values to validate our results.

In chapter 3 & 4 we use different statistical, numerical and information theoretical methods to extract information about the dynamics of the respective laser systems with delay feedback. This approach proved very successful and can be extended to biological or climatological systems, where we may not have the exact dynamical equations in hand. Comparison of different measures in these cases may provide crucial information about the underlying mechanisms that produce the complex output and which may help to better understand, model and predict their dynamics.

BIBLIOGRAPHY

- [1] A. Sennaroglu, *Photonics and Laser Engineering: Principles, Devices, and Applications* (McGraw-Hill Education, 2010).
- [2] M. C. Soriano, J. García-Ojalvo, C. R. Mirasso, and I. Fischer, *Complex photonics: Dynamics and applications of delay-coupled semiconductor lasers*, *Rev. Mod. Phys.* **85**, 421 (2013).
- [3] C. Risch, C. Voumard, F. Reinhart, and R. Salathe, *External-cavity-induced nonlinearities in the light versus current characteristic of (Ga,Al)As continuous-wave diode lasers*, *IEEE Journal of Quantum Electronics*, **13**, 692 (1977).
- [4] C. Weiss and R. Vilaseca, *Dynamics of lasers*, Nonlinear systems (VCH, 1991).
- [5] Y. C. Kouomou, P. Colet, L. Larger, and N. Gastaud, *Hyperchaotic Breathers in Semiconductor Lasers with Delayed Electro-Optical Feedback*, in *Conference on Lasers and Electro-Optics/Quantum Electronics and Laser Science and Photonic Applications Systems Technologies* (Optical Society of America, 2005) p. JTuC76.
- [6] R. Vicente, J. Dauden, P. Colet, and R. Toral, *Analysis and characterization of the hyperchaos generated by a semiconductor laser subject to a delayed feedback loop*, *IEEE Journal of Quantum Electronics* **41**, 541 (2005).
- [7] G.-y. JIANG, J. ZHANG, and Y. HUANG, *Chaos and its control in semiconductor laser with delayed negative optoelectronic feedback*, *Turk J Phys* **37**, 296 (2013).
- [8] T. Deng, G.-Q. Xia, Z.-M. Wu, X.-D. Lin, and J.-G. Wu, *Chaos synchronization in mutually coupled semiconductor lasers with asymmetrical bias currents*, *Opt. Express* **19**, 8762 (2011).

- [9] R. N. Hall, G. E. Fenner, J. D. Kingsley, T. J. Soltys, and R. O. Carlson, *Coherent Light Emission From GaAs Junctions*, Phys. Rev. Lett. **9**, 366 (1962).
- [10] M. I. Nathan, W. P. Dumke, G. Burns, F. H. Dill, and G. Lasher, *STIMULATED EMISSION OF RADIATION FROM GaAs p-n JUNCTIONS*, Applied Physics Letters **1**, 62 (1962).
- [11] T. M. Quist, R. H. Rediker, R. J. Keyes, W. E. Krag, B. Lax, A. L. McWhorter, and H. J. Zeigler, *SEMICONDUCTOR MASER OF GaAs*, Applied Physics Letters **1**, 91 (1962).
- [12] Z. I. Alferov, *Nobel Lecture: The double heterostructure concept and its applications in physics, electronics, and technology*, Rev. Mod. Phys. **73**, 767 (2001).
- [13] H. Kroemer, *Nobel Lecture: Quasielectric fields and band offsets: teaching electrons new tricks*, Rev. Mod. Phys. **73**, 783 (2001).
- [14] I. Hayashi, M. B. Panish, P. W. Foy, and S. Sumski, *JUNCTION LASERS WHICH OPERATE CONTINUOUSLY AT ROOM TEMPERATURE*, Applied Physics Letters **17**, 109 (1970).
- [15] H. Kawaguchi, *Bistabilities and Nonlinearities in Laser Diodes*, Artech House optoelectronics library (Artech House, 1994).
- [16] G. Agrawal and N. Dutta, *Semiconductor Lasers* (Springer US, 1993).
- [17] A. M. Stoneham, *Non-radiative transitions in semiconductors*, Reports on Progress in Physics **44**, 1251 (1981).
- [18] T. Heil, I. Fischer, and W. Elsässer, *Influence of amplitude-phase coupling on the dynamics of semiconductor lasers subject to optical feedback*, Phys. Rev. A **60**, 634 (1999).
- [19] C. Henry, *Phase noise in semiconductor lasers*, Journal of Applied Physics **4**, 298 (1986).

- [20] B. Zhao, T. Chen, and A. Yariv, *A comparison of amplitude-phase coupling and linewidth enhancement in semiconductor quantum-well and bulk lasers*, *IEEE Photonics Journal* **29**, 1027 (1993).
- [21] H. Gerhardt, H. Welling, and A. Güttner, *Measurements of the laser linewidth due to quantum phase and quantum amplitude noise above and below threshold. I*, *Zeitschrift für Physik* **253**, 113 (1972).
- [22] J. Coleman, J. Young, and A. Garg, *Semiconductor Quantum Dot Lasers: A Tutorial*, *Journal of Light Microscopy* **29**, 499 (2011).
- [23] Y. Arakawa and H. Sakaki, *Multidimensional quantum well laser and temperature dependence of its threshold current*, *Applied Physics Letters* **40**, 939 (1982).
- [24] G. P. Agrawal, *Effect of gain nonlinearities on period doubling and chaos in directly modulated semiconductor lasers*, *App.Phys.Lett* **49**, 1013 (1986).
- [25] S. Bennett, C. M. Snowden, and S. Iezekiel, *Nonlinear dynamics in directly modulated multiple-quantum-well laser diodes*, *IEEE Photonics Journal*, **33**, 2076 (1997).
- [26] R. Nagarajan, T. Fukushima, S. W. Corzine, and J. E. Bowers, *Effects of carrier transport on high-speed quantum well lasers*, *Applied Physics Letters* **59**, 1835 (1991).
- [27] A. Al-Khursan, B. Ghalib, and S. Al-Obaidi, *Numerical simulation of optical feedback on a quantum dot lasers*, *Semiconductors* **46**, 213 (2012).
- [28] B. A. Ghalib, S. J. Al-Obaidi, and A. H. Al-Khursan, *Modeling of synchronization in quantum dot semiconductor lasers*, *Optics & Laser Technology* **48**, 453 (2013).
- [29] D. O'Brien, S. P. Hegarty, G. Huyet, and A. V. Uskov, *Sensitivity of quantum-dot semiconductor lasers to optical feedback*, *Opt. Lett.* **29**, 1072 (2004).
- [30] M. Lakshmanan and D. V. Senthilkumar, *Dynamics of Nonlinear Time Delay Systems*, Springer series in synergetics (Springer, 2010).

- [31] E. Tziperman, L. Stone, M. A. Cane, and H. Jarosh, *El Nino Chaos: Overlapping of Resonances Between the Seasonal Cycle and the Pacific Ocean-Atmosphere Oscillator*, *Science* **264**, 72 (1994), <http://www.sciencemag.org/content/264/5155/72.full.pdf>.
- [32] I. Boutle, R. H. S. Taylor, and R. A. Römer, *El Niño and the delayed action oscillator*, *American Journal of Physics* **75**, 15 (2007).
- [33] K. Ikeda, H. Daido, and O. Akimoto, *Optical Turbulence: Chaotic Behavior of Transmitted Light from a Ring Cavity*, *Phys. Rev. Lett.* **45**, 709 (1980).
- [34] F. A. Hopf, D. L. Kaplan, H. M. Gibbs, and R. L. Shoemaker, *Bifurcations to chaos in optical bistability*, *Phys. Rev. A* **25**, 2172 (1982).
- [35] H. M. Gibbs, F. A. Hopf, D. L. Kaplan, and R. L. Shoemaker, *Observation of Chaos in Optical Bistability*, *Phys. Rev. Lett.* **46**, 474 (1981).
- [36] A. Neyer and E. Voges, *Dynamics of electrooptic bistable devices with delayed feedback*, *IEEE Journal of Quantum Electronics* **18**, 2009 (1982).
- [37] R. Vallee and C. Delisle, *Mode description of the dynamical evolution of an acousto-optic bistable device*, *IEEE Journal of Quantum Electronics* **21**, 1423 (1985).
- [38] H. U. Voss, *Anticipating chaotic synchronization*, *Phys. Rev. E* **61**, 5115 (2000).
- [39] E. M. Shahverdiev, S. Sivaprakasam, and K. A. Shore, *Inverse anticipating chaos synchronization*, *Phys. Rev. E* **66**, 017204 (2002).
- [40] M. Mackey and L. Glass, *Oscillation and chaos in physiological control systems*, *Science* **197**, 287 (1977), <http://www.sciencemag.org/content/197/4300/287.full.pdf>.
- [41] M. Szydłowski, A. Krawiec, and J. Tobała, *Nonlinear oscillations in business cycle model with time lags*, *Chaos, Solitons & Fractals* **12**, 505 (2001).
- [42] S. Manjunath, D. Ghosh, and G. Raina, *A Kaldor-Kalecki model of business cycles: Stability and limit cycles*, in *Control and Decision Conference (2014 CCDC), The 26th Chinese* (2014) pp. 2650–2656.

- [43] A. Krawiec and M. Szydlowski, *The Kaldor Kalecki business cycle model*, Annals of Operations Research **89**, 89.
- [44] L. Shampine and S. Thompson, *Solving {DDEs} in Matlab*, Applied Numerical Mathematics **37**, 441 (2001).
- [45] W. Enright and M. Hu, *Interpolating Runge-Kutta methods for vanishing delay differential equations*, Computing **55**, 223 (1995).
- [46] Wikipedia, *Runge-Kutta methods* — *Wikipedia, The Free Encyclopedia*, (2015), [Online; accessed 26-October-2015].
- [47] K. In't Hout and M. Spijker, *Stability analysis of numerical methods for delay differential equations*, Numerische Mathematik **59**, 807 (1991).
- [48] I. Fudziah, *Numerical Treatment of Delay Differential Equations by Runge Kutta Method Using Hermite Interpolation*, Matematika **18**, 79 (2002).
- [49] R. Broom, *Self modulation at gigahertz frequencies of a diode laser coupled to an external cavity*, Electronics Letters **5**, 571 (1969).
- [50] R. F. Broom, E. Mohn, C. Risch, and R. Salathe, *Microwave self-modulation of a diode laser coupled to an external cavity*, IEEE Journal of Quantum Electronics **6**, 328 (1970).
- [51] C. Mirasso, P. Colet, and P. Garcia-Fernandez, *Synchronization of chaotic semiconductor lasers: application to encoded communications*, Photonics Technology Letters, IEEE **8**, 299 (1996).
- [52] J.-P. Goedgebuer, L. Larger, H. Porte, and F. Delorme, *Chaos in wavelength with a feedback tunable laser diode*, Phys. Rev. E **57**, 2795 (1998).
- [53] P. R. Roelfsema, A. K. Engel, P. Konig, and W. Singer, *Visuomotor integration is associated with zero time-lag synchronization among cortical areas*, Nature **385**, 157 (1997).

- [54] Bogatov73, *Study of the single-mode injection laser*, *IEEE Journal of Quantum Electronics* **9**, 392 (1973).
- [55] R. Lang and K. Kobayashi, *External optical feedback effects on semiconductor injection laser properties*, *IEEE Journal of Quantum Electronics* **16**, 347 (1980).
- [56] Y. C. KOUOMOU, *Nonlinear Dynamics of Semiconductor Laser Systems with Feedback*, (2006).
- [57] J. Mulet and C. R. Mirasso, *Numerical statistics of power dropouts based on the Lang-Kobayashi model*, *Phys. Rev. E* **59**, 5400 (1999).
- [58] J. Tiana-Alsina, M. C. Torrent, O. A. Rosso, C. Masoller, and J. Garcia-Ojalvo, *Quantifying the statistical complexity of low-frequency fluctuations in semiconductor lasers with optical feedback*, *Phys. Rev. A* **82**, 013819 (2010).
- [59] C. Risch and C. Voumard, *Selfpulsation in the output intensity and spectrum of GaAs-AlGaAs cw diode lasers coupled to a frequency-selective external optical cavity*, *Journal of Applied Physics* **48**, 2083 (1977).
- [60] D. Lenstra, B. Verbeek, and A. Den Boef, *Coherence collapse in single-mode semiconductor lasers due to optical feedback*, *IEEE Journal of Quantum Electronics* **21**, 674 (1985).
- [61] T. Takizawa, Y. Liu, and J. Ohtsubo, *Chaos in a feedback Fabry-Perot interferometer*, *IEEE Journal of Quantum Electronics* **30**, 334 (1994).
- [62] S. Rajesh and V. Nandakumaran, *Suppression of chaos in a directly modulated semiconductor laser with delayed optoelectronic feedback*, *Physics Letters A* **319**, 340 (2003).
- [63] S. Tang and J. Liu, *Chaotic pulsing and quasi-periodic route to chaos in a semiconductor laser with delayed opto-electronic feedback*, *IEEE Journal of Quantum Electronics* **37**, 329 (2001).

- [64] E.-Y. Lin and J.-M. Liu, *Nonlinear dynamics of a semiconductor laser with delayed negative optoelectronic feedback*, *EPL* **39**, 562 (2003).
- [65] S. Strogatz, *Nonlinear Dynamics and Chaos: With Applications to Physics, Biology, Chemistry, and Engineering*, Advanced book program (Westview Press, 1994).
- [66] M. Lakshmanan and S. Rajasekar, *Qualitative Features*, in *Nonlinear Dynamics*, Advanced Texts in Physics (Springer Berlin Heidelberg, 2003) pp. 31–74.
- [67] M. Lakshmanan and S. Rajasekar, *Bifurcations and Onset of Chaos in Dissipative Systems*, in *Nonlinear Dynamics*, Advanced Texts in Physics (Springer Berlin Heidelberg, 2003) pp. 75–121.
- [68] B. Krauskopf, *Bifurcation analysis of laser systems*, AIP Conference Proceedings **548**, 1 (2000).
- [69] H. Fujino and J. Ohtsubo, *Synchronization of Chaotic Oscillations in Mutually Coupled Semiconductor Lasers*, *Optical Review* **8**, 351.
- [70] J. Sacher *et al.*, *Intensity instabilities of semiconductor lasers under current modulation, external light injection, and delay feedback*. *Phys.Rev.A* **45**, 1893 (1992).
- [71] S.Rajesh and V.M.Nandakumaran, *Control of bistability in a directly modulated semiconductor laser using delayed optoelectronic feedback*, *Physica D* **213**, 113 (2006).
- [72] S. M. Wieczorek, in *Nonlinear Laser Dynamics* (Wiley-VCH Verlag GmbH & Co. KGaA, 2012) pp. 269–291.
- [73] T. Erneux and P. Glorieux, *Laser Dynamics* (Cambridge University Press, 2010).
- [74] E.-Y. Lin and J.-M. Liu, *Chaotic lidar*, *Selected Topics in Quantum Optics* **10**, 991 (2004).
- [75] C. Masoller, C. Cabeza, and A. Sicardi Schifino, *Effect of the nonlinear gain in the visibility of a semiconductor laser with incoherent feedback in the coherence collapsed regime*, *IEEE Journal of Quantum Electronics* **31**, 1022 (1995).

- [76] B. Krauskopf, G. R. Gray, and D. Lenstra, *Semiconductor laser with phase-conjugate feedback: Dynamics and bifurcations*, Phys. Rev. E **58**, 7190 (1998).
- [77] R. Vicente *et al.*, *Dynamics of semiconductor lasers with bidirectional optoelectronic coupling: Stability, route to chaos, and entrainment*, Phys.Rev.E **70** (2004).
- [78] F. Rogister, *Nonlinear Dynamics of Semiconductor Lasers Subject to Optical Feedback*, Phd thesis (2001).
- [79] T.P.Lee *et al.*, *Short cavity InGaAsP injection lasers: dependence of mode spectra and single-longitudinal-mode power on cavity length*, IEEE journal of quantum electronics **QE-18**, 1101 (82).
- [80] M. Soriano, L. Zunino, O. Rosso, I. Fischer, and C. Mirasso, *Time Scales of a Chaotic Semiconductor Laser With Optical Feedback Under the Lens of a Permutation Information Analysis*, E E J o r n a l o f Q E **47**, 252 (2011).
- [81] J. M. Buldú, J. García-Ojalvo, C. R. Mirasso, M. C. Torrent, and J. M. Sancho, *Effect of external noise correlation in optical coherence resonance*, Phys. Rev. E **64**, 051109 (2001).
- [82] D. V. Ramana Reddy, A. Sen, and G. L. Johnston, *Time Delay Induced Death in Coupled Limit Cycle Oscillators*, Phys. Rev. Lett. **80**, 5109 (1998).
- [83] M. Parvathi, *Nonlinear Dynamics of Nd:YAG lasers: Hopf bifurcation, Multistability and Chaotic Synchronization*, Ph.D. thesis, <http://dyuthi.cusat.ac.in/xmlui/purl/1951> (2009).
- [84] C. Otto, K. Lüdge, and E. Schöll, *Modeling quantum dot lasers with optical feedback: sensitivity of bifurcation scenarios*, physica status solidi (b) **247**, 829 (2010).
- [85] M. J. Bünner, M. Popp, T. Meyer, A. Kittel, and J. Parisi, *Tool to recover scalar time-delay systems from experimental time series*, Phys. Rev. E **54**, R3082 (1996).

- [86] R. Hegger, M. J. Bünner, H. Kantz, and A. Giaquinta, *Identifying and Modeling Delay Feedback Systems*, Phys. Rev. Lett. **81**, 558 (1998).
- [87] V. S. Udaltsov, L. Larger, J. P. Goedgebuer, A. Locquet, and D. S. Citrin, *Time delay identification in chaotic cryptosystems ruled by delay-differential equations*, J. Opt. Technol. **72**, 373 (2005).
- [88] L. Zunino, M. C. Soriano, I. Fischer, O. A. Rosso, and C. R. Mirasso, *Permutation-information-theory approach to unveil delay dynamics from time-series analysis*, Phys. Rev. E **82**, 046212 (2010).
- [89] M. Siefert, *Practical criterion for delay estimation using random perturbations*, Phys. Rev. E **76**, 026215 (2007).
- [90] A. V. Uskov, Y. Boucher, J. Le Bihan, and J. McInerney, *Theory of a self-assembled quantum-dot semiconductor laser with Auger carrier capture: Quantum efficiency and nonlinear gain*, Applied Physics Letters **73**, 1499 (1998).
- [91] D. Rontani, A. Locquet, M. Sciamanna, and D. S. Citrin, *Loss of time-delay signature in the chaotic output of a semiconductor laser with optical feedback*, Opt. Lett. **32**, 2960 (2007).
- [92] D. Rontani, A. Locquet, M. Sciamanna, D. Citrin, and S. Ortin, *Time-Delay Identification in a Chaotic Semiconductor Laser With Optical Feedback: A Dynamical Point of View*, IEEE Journal of Quantum Electronics **45**, 879 (2009).
- [93] C. Bandt and B. Pompe, *Permutation Entropy: A Natural Complexity Measure for Time Series*, Phys. Rev. Lett. **88**, 174102 (2002).
- [94] T. M. Cover and J. A. Thomas, *Elements of Information Theory* (Wiley-Interscience, New York, NY, USA, 1991).
- [95] D. Jungnickel, *Algorithms and Complexity*, in *Graphs, Networks and Algorithms*, Algorithms and Computation in Mathematics, Vol. 5 (Springer Berlin Heidelberg, 2013) pp. 35–63.

- [96] M. Martin, A. Plastino, and O. Rosso, *Statistical complexity and disequilibrium*, Physics Letters A **311**, 126 (2003).
- [97] M. Martin, A. Plastino, and O. Rosso, *Generalized statistical complexity measures: Geometrical and analytical properties*, Physica A: Statistical Mechanics and its Applications **369**, 439 (2006).
- [98] X. Calbet and R. López-Ruiz, *Tendency towards maximum complexity in a nonequilibrium isolated system*, Phys. Rev. E **63**, 066116 (2001).
- [99] R. López-Ruiz, H. Mancini, and X. Calbet, *A statistical measure of complexity*, Physics Letters A **209**, 321 (1995).
- [100] B. A. Huberman and T. Hogg, *Complexity and Adaptation*, Phys. D **2**, 376 (1986).
- [101] W. Bechtel, *The Compatibility of Complex Systems and Reduction: A Case Analysis of Memory Research*, Minds and Machines **11**, 483 (2001).
- [102] A. Locquet, *Chaos-Based Secure Optical Communications Using Semiconductor Lasers*, in *Handbook of Information and Communication Security*, edited by P. Stavroulakis and M. Stamp (Springer Berlin Heidelberg, 2010) pp. 451–478.
- [103] B. Krishna, M. John, and V. Nandakumaran, *Bidirectional communication using delay coupled chaotic directly modulated semiconductor lasers*, Pramana **74**, 177 (2010).
- [104] X. Li, W. Pan, B. Luo, and D. Ma, *Chaos Synchronization and Communication of Cascade-Coupled Semiconductor Lasers*, J. Lightwave Technol. **24**, 4936 (2006).
- [105] I. Fischer, G. H. M. van Tartwijk, A. M. Levine, W. Elsässer, E. Göbel, and D. Lenstra, *Fast Pulsing and Chaotic Itinerancy with a Drift in the Coherence Collapse of Semiconductor Lasers*, Phys. Rev. Lett. **76**, 220 (1996).
- [106] E. A. Viktorov, P. Mandel, and G. Huyet, *Long-cavity quantum dot laser*, Opt. Lett. **32**, 1268 (2007).

A

PUBLICATIONS



Turkish Journal of Physics
<http://journals.tubitak.gov.tr/physics/>

Research Article

Turk J Phys
 (2015) 39: 60 – 68
 © TÜBİTAK
 doi:10.3906/fiz-1405-13

Analysis and simulation of semiconductor laser dynamics with optoelectronic delay feedback

Varghese BEJOY^{1,*}, Sivasankaran RAJESH², Vadakkedath Madhom NANDAKUMARAN^{1,3}

¹International School of Photonics, Cochin University of Science and Technology, Kochi, India

²Department of Physics, N.S.S. College, Pandalam, Pathanamthitta, India

³Department of Physics, Amrita School of Arts and Sciences, Amrita Viswavidyapeetham, Kollam, India

Received: 23.05.2014 • Accepted: 25.08.2014 • Published Online: 23.02.2015 • Printed: 20.03.2015

Abstract: In this work we investigate semiconductor laser dynamics with optoelectronic delay feedback, both analytically and numerically. Stability criteria are derived from the delay differential equations of the system. Stability curves are obtained in the feedback strength–delay parameter space. We show that delay has a role in determining the stability only for a range of feedback strength and this range can vary depending on other parameters. Effects of bias current and nonlinear gain reduction on the stability curves are shown in the analysis and numerically verified.

Key words: Semiconductor laser, delay feedback, stability, Hopf bifurcation

1. Introduction

Semiconductor lasers (SLs) with delayed feedback have been investigated extensively in recent years, due to the rich variety of nonlinear phenomena they exhibit and also because of their potential applications [1]. They are excellent dynamical models that show many exciting phenomena such as low and high dimensional chaos [2], local and global bifurcations [3], control [4] and synchronization of chaos [5,6], intensity instabilities [7], multistability and hysteresis [8], and stochastic resonance effects [9,10]. Incorporating time delay into the system makes it infinite dimensional and consequently the system can exhibit very complex dynamics. Many aspects of delay dynamics have been observed and studied first in laser systems [1,11]. These nonlinear effects in semiconductor lasers have novel technological applications like secure information encryption [9,12] and chaotic lidar [13]. Modification of laser dynamics with feedback depends on many factors such as type and strength of feedback, delay time involved in the feedback mechanism, bias current, and other parameters like gain nonlinearities. Feedback mechanism can be either optical [14,15] or optoelectronic [16,17]. In optical feedback, a part of the output laser field is injected back into the laser cavity. The other technique involves a high bandwidth photodetector for optoelectronic conversion of the laser output and the injection of a suitably amplified detector signal into the pumping current of the SL. Even when the nonlinear gain reduction is strong enough to inhibit period doubling and chaos in current modulated semiconductor lasers [18], delay feedback has been proved to induce bifurcations and chaos [19]. Destabilization of the fixed point by Hopf bifurcation in SLs with optoelectronic feedback has been reported in many works [15,17]. Given such considerations, it is of utmost importance for the system designer to know how the SL stability varies with feedback and changes with different parameters. In this work, we analyze the delay differential equations of the SL with optoelectronic

*Correspondence: bejoyrosily@gmail.com

delay feedback to study the dependence of Hopf bifurcation phenomena on the nonlinear gain reduction factor, for a range of values of feedback strength and bias current. In addition, the effect of initial condition on the dynamics is studied by switching on the delay mechanism at different stages in the operation of the laser.

2. Model and analysis

In optoelectronic delay feedback the phase of the output optical field is not involved in determining the system dynamics. Therefore, the dynamics can be studied using 2 rate equations, one for carrier density (N) and the other for photon density (P). Single mode rate equations of an SL are given by [18,20]

$$\frac{dN}{dt} = \frac{1}{\tau_e} \left(\frac{I}{I_{th}} - N - \frac{N - \delta}{1 - \delta} P \right) \quad (1)$$

$$\frac{dP}{dt} = \frac{1}{\tau_p} \left(\frac{N - \delta}{1 - \delta} (1 - \varepsilon P) P - P + \beta N \right), \quad (2)$$

where I is the total pumping current, I_{th} is threshold laser current, and τ_e and τ_p are the electron and photon lifetimes, respectively. $\delta = n_0/n_{th}$, n_0 is the carrier density required for transparency and n_{th} is the threshold carrier density. ε is related to the nonlinear gain reduction factor ε_{NL} by the equation [18]

$$\varepsilon = \varepsilon_{NL} \Gamma \left(\frac{\tau_e}{\tau_p} \right) n_{th}. \quad (3)$$

is the confinement factor. β is the spontaneous emission factor. When optoelectronic feedback is introduced the total pumping current at any instant of time becomes

$$I(t) = I_b + FP(t - \tau). \quad (4)$$

Here I_b is the constant bias current, F is the feedback strength, and τ represents the delay in feedback. This delay can arise from time taken for external transit of the laser beam and finite response time of the detector as well as the intentional delays included in the feedback circuitry. The values of the parameters are chosen as $\tau_p = 6$ ps, $\tau_e = 3$ ns, $\delta = 0.692$, $\beta = 5.0 \times 10^{-5}$ [18].

To determine the stability of the fixed point of the system consisting of Eqs. (1) and (2), the nature of the roots of the characteristic equation has to be calculated. The characteristic equation of a delay differential system is a transcendental equation that admits several solutions, given by [11]

$$|J_0 + e^{-\lambda\tau} J_\tau - \lambda I| = 0, \quad (5)$$

where J_0 is the Jacobian with respect to the present variables, J_τ is the Jacobian with respect to the delayed variables evaluated at the equilibrium point, and λ s are the eigen values with $\lambda = \alpha + i\gamma$. If all of the eigenvalues of the characteristic equation have negative real parts, then the equilibrium point is said to be stable. On the other hand, if at least one of the eigenvalues has a positive real part, then the equilibrium point is unstable. The characteristic equation for our set of rate equation becomes

$$\lambda^2 + K_2\lambda + K_3 + K_4e^{-\lambda\tau} = 0, \quad (6)$$

where

$$K_2 = \left(\frac{1}{\tau_e} \right) \left[1 + \frac{P_0}{(1 - \delta)} \right] - \frac{(N_0 - 1 - 2\varepsilon P_0)(N_0 - \delta)}{\tau_p(1 - \delta)} \quad (7)$$

BEJOY et al./Turk J Phys

$$K_3 = \frac{-1}{\tau_e \tau_p (1 - \delta)} \left[\left(1 + \frac{P_0}{(1 - \delta)} \right) (N_0 - 1 - 2\varepsilon P_0 (N_0 - \delta)) + (\varepsilon P_0^2 - P_0 - \beta (1 - \delta)) \left(\frac{N_0 - \delta}{1 - \delta} \right) \right] \quad (8)$$

$$K_4 = \frac{-F}{\tau_e \tau_p I_{th} (1 - \delta)} [-\varepsilon P_0^2 + P_0 + \beta (1 - \delta)]. \quad (9)$$

A change in stability can occur only when a root of Eq. (5) crosses the imaginary axis, that is when the real part of the eigenvalue changes from negative to positive, where λ with $\alpha = 0$ is a solution of the equation. Substituting $\alpha = 0$ in Eq. (6) and equating the real and imaginary parts of the resulting equation we get

$$K_2 \gamma - K_4 \sin(\gamma \tau) = 0 \quad (10)$$

and

$$-\gamma^2 + K_3 + K_4 \cos(\gamma \tau) = 0, \quad (11)$$

which leads to

$$\tau_{\pm} = \frac{\pm \arccos\left(\left[\frac{\gamma^2 - K_3}{K_4}\right]\right) + 2n\pi}{\gamma}, \quad (12)$$

where n is an integer. Squaring and adding Eqs. (10) and (11) result in a fourth degree equation in γ

$$\gamma^4 + \gamma^2 (K_2^2 - 2K_3) + (K_3^2 - K_4^2) = 0. \quad (13)$$

This equation is solved to find the range of F , where γ^2 is real and positive. τ_{\pm} are calculated using Eq. (12) for these values of F . Both τ_- and τ_+ satisfy the characteristic equation for $\alpha = 0$. The results we present in this work are specific to 2 types of feedback schemes: when feedback starts after the SL has stabilized to steady state operation and when feedback is present from the beginning of SL operation. In the first scheme the bifurcations happen on τ_- , but feedback can be applied in many possible ways, of which one may lead to bifurcations on τ_+ . As delay systems generally exhibit abundant multistability, to devise such a unique scheme can be difficult. Since the feedback schemes we use in this work do not give bifurcations on τ_+ , in the following discussions we assume

$$\tau_i(n) = \frac{-\arccos\left(\frac{\gamma_i^2 - K_3}{K_4}\right) + 2n\pi}{\gamma_i}, \quad (14)$$

$i = 1, 2$ corresponding to 2 real and positive solutions of Eq. (13). Negative or imaginary values of γ will yield $\tau_i(n)$'s that are unphysical. These are the critical values of delay (τ_c) where the stability changes. To find the direction in which the eigen value crosses the imaginary axis, $d\alpha/d\tau$ is calculated on each $\tau(n)$. If $d\alpha/d\tau$ is positive, at delay equal to $\tau_i(n)$, the eigenvalue crosses the imaginary axis to the positive side as the delay is increased and the fixed point becomes unstable. If $d\alpha/d\tau$ is negative at $\tau_i(n)$, the eigen value crosses the imaginary axis to the negative side of α and the fixed point becomes stable. Thus it can be seen that for the same value of F , depending on the value of delay, the fixed point can be stable or unstable.

$$\frac{d\alpha}{d\tau}_{\lambda=i\gamma} = \frac{-(K_4) \gamma \sin(\gamma \tau) (-K_2 + K_4 \tau \cos(\gamma \tau)) - K_4 \gamma \cos(\gamma \tau) (2\gamma - K_4 \tau \sin(\gamma \tau))}{(-K_2 + K_4 \tau \cos(\gamma \tau))^2 + (2\gamma - K_4 \tau \sin(\gamma \tau))^2} \quad (15)$$

3. Simulation and results

Figure 1a shows the plot of $\tau(n)$'s from Eq. (12) plotted against F/I_{th} for the parameter values $I_0 = 1.5$ and $\varepsilon = 0.025$, where I_0 is defined as I_b/I_{th} . Solid curves represent the critical delays with $d\alpha/d\tau$ positive and the dashed curves represent the critical delays with $d\alpha/d\tau$ negative. Substituting Eq. (14) in Eq. (15) we find that $d\alpha/d\tau$ is positive for τ_1 and negative for τ_2 for all values of n . τ_1 and τ_2 for the same value of n join to form closed curves ($\tau_1\tau_2(n)$). Four such closed curves for n equal 1 to 4 are shown in Figure 1a. They exist only for a range of F ; outside this range stability does not depend on τ . Moreover, immediately outside this range, α is negative, indicating the fixed point is stable. Figure 1b shows the scan of $(F/I_{th}, \tau)$ parameter space, by simulating the laser dynamics with feedback at each point. The shaded area represents points where the solution $P(t)$ converged to a fixed point and the unshaded region represent the points where $P(t)$ is oscillatory. Substituting $\tau = 0$ in the characteristic equation and solving, we find that α is negative at $\tau = 0$ below the curve τ_1 ($n = 1$). Therefore, the fixed point is stable at $\tau = 0$. Thus the first stability region is the area enclosed between the curves $\tau = 0$ and τ_1 ($n = 1$). In Figure 1b, this is the shaded region below the first unshaded patch. From τ_1 ($n = 1$), stability regions are formed between a lower dashed curve and an upper solid curve. Inside the region enclosed by $\tau_1\tau_2$ (n), the fixed point is always unstable because α calculated at the fixed point is always greater than zero, as indicated by the solid lower curves and dashed upper curves. However, at both ends of these curves, where there are no overlaps, stability regions are formed between $\tau_2(n)$ and $\tau_1(n + 1)$. These are the protruding shaded regions on both sides in Figure 1b. Successive curves overlap to greater extent in the middle and the stability regions are pushed towards both sides, reducing their area. In the simulations it is assumed that the feedback is applied after the laser has stabilized to its steady state. What happens when the feedback is applied before stabilization is discussed in section 3.3. Figure 2 depicts the Hopf bifurcations at the critical delay values. At $F/I_{th} = 0.45$, the first instance of losing stability occurs at the critical value of delay $\tau_c = 0.33$ ns; this point is marked P1 in Figure 1a. Figure 2a shows $P(t)$ at 0.2 ns where $\tau < \tau_c$. When feedback is applied $P(t)$ suddenly stabilizes to the new fixed point with highly damped oscillations. At $\tau = \tau_c$ a periodic solution appears as shown in Figure 2b. When $\tau > \tau_c$, undamped growing oscillations are obtained

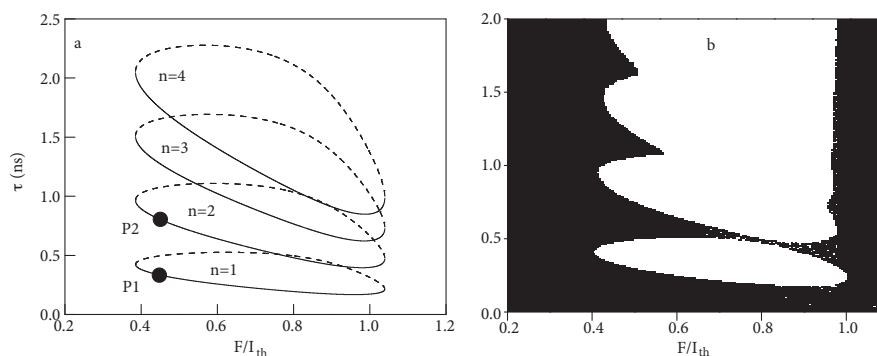


Figure 1. (a) Curves representing Eq. (14) for the parameter values $I_0 = 1.5$ and $\varepsilon = 0.025$ and for n from 1 to 4. Solid curves represent $\tau_1(n)$ and dashed curves represent $\tau_2(n)$. τ_1 and τ_2 for the same value of n are joined to form closed curves. $d\alpha/d\tau_n$ is positive for τ_1 and negative for τ_2 . (b) Stability regions obtained by simulating the dynamical Eqs. (1) and (2). Shaded regions show the points at which the laser goes to a steady state when feedback is applied and the unshaded regions show the points at which the laser goes to an oscillatory state.

BEJOY et al./Turk J Phys

(Figure 2c). Figures 2d–2f depict the same scenario across the second instance (marked P2 in Figure 1a) of losing stability at $\tau_c = 0.8$ ns. This numerically verifies the Hopf bifurcation phenomena occurring along the critical delay curves with $d\alpha/d\tau$ is positive, that is, on $\tau_1(n)$.

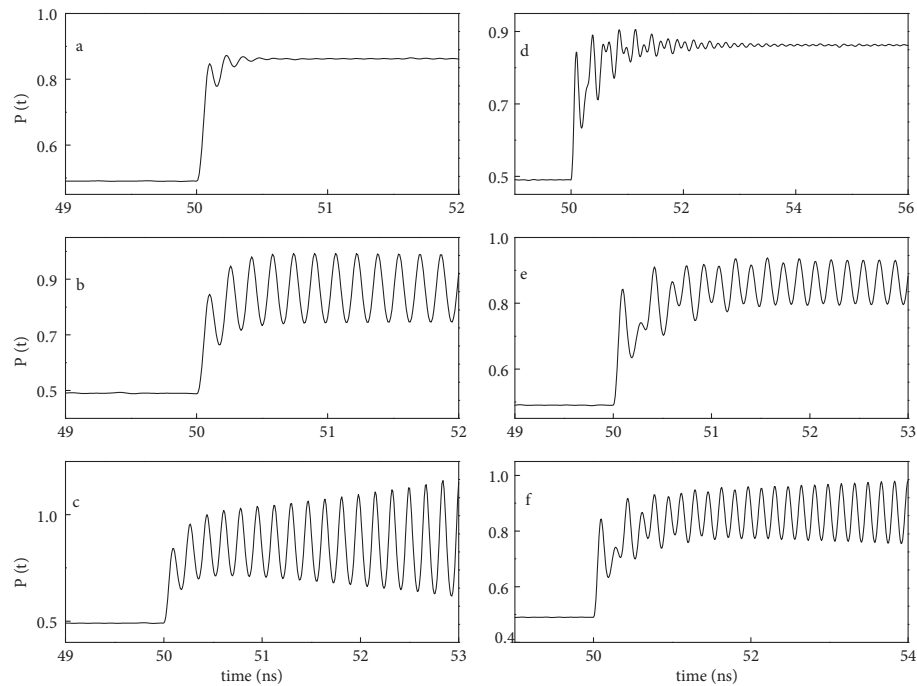


Figure 2. Solution $P(t)$ of the laser dynamical equations when the feedback is applied at $t = 50$ ns with $F/I_{th} = 0.45$. (a) Damped oscillatory decay to the fixed point at $\tau = 0.2$ ns. (b) Periodic solution at $\tau = \tau_c = 0.33$ ns. (c) Undamped growing oscillations at $\tau = 0.4$ ns. (d) Damped oscillatory decay to the fixed point at $\tau = 0.75$ ns. (e) Periodic solution at $\tau = \tau_c = 0.8$ ns. (f) Undamped growing oscillations at $\tau = 0.85$ ns. (a),(b), and (c) show Hopf bifurcation happening at $\tau_c = 0.33$ ns and (d),(e), and (f) show the same for $\tau_c = 0.8$ ns.

3.1. Effect of nonlinear gain reduction factor

We show that changes in ε can drastically change the critical delay curves. In Figure 3 delay curves for increasing values of ε are plotted. For small values of ε stability regions are formed only on the lower side of F/I_{th} except for the first stability region that lies between $\tau = 0$ and $\tau_1(n = 1)$. This result is shown in Figure 3a for the value 0.01 of ε . Here all τ_1 's where $d\alpha/d\tau_n$ is positive (solid curves) converge closer to the $\tau = 0$ axis for higher values of F/I_{th} and at least one eigen value has a positive real part above $\tau_1(n = 1)$, on the right end. The span of the curves decreases as ε is increased to 0.02 in Figure 3b, which indicates that delay has a role in determining stability only for shorter ranges of F/I_{th} . With further increase in ε , the curves with $d\alpha/d\tau_n$ positive and negative for the same n join at the right end to form closed structures ($\tau_1\tau_2(n)$) and stability regions are formed at both ends. At the same time, the extent of overlap between these closed

curves decreases. In Figure 3c, $\tau_1\tau_2(1)$ and $\tau_1\tau_2(2)$ completely move apart from overlap for $\varepsilon = 0.03$ and the stability region becomes continuous between them. More curves move apart as ε is increased and they change to elliptical as shown in Figure 3d. Around $\varepsilon = 0.035$ the curves completely disappear, making the stability of the fixed point independent of τ .

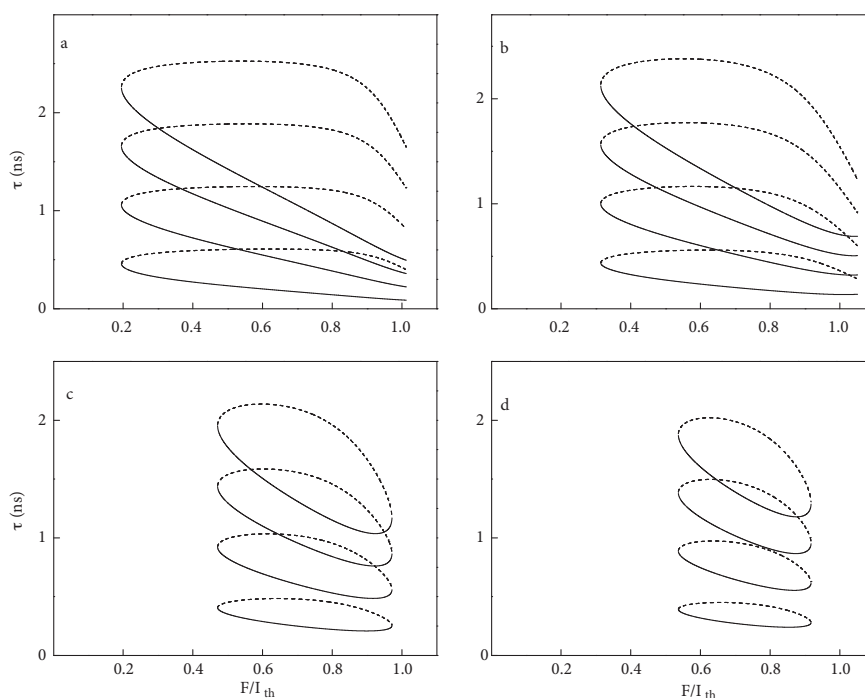


Figure 3. Critical delay curves for 4 different values of ε . (a) $\varepsilon = 0.01$, (b) $\varepsilon = 0.02$, (c) $\varepsilon = 0.03$, (d) $\varepsilon = 0.031$.

3.2. Effect of bias current

Figures 4a–4c show critical delay curves at $\varepsilon = 0.025$ for I_0 equal to 1.4, 1.7, and 1.9, respectively. Increase in I_0 has similar effects as increase in ε . Dependence of stability on delay converges to shorter ranges of F for higher I_0 's. The closed curve structures ($\tau_1\tau_2(n)$) change to oval and the extent of overlap between them decreases. Around I_0 equal to 1.9 four curves move apart and form continuous stability regions between them. As a result of flattening of the curves, for higher I_0 successive Hopf bifurcations come closer in delay. The curves completely disappear before I_0 is increased up to 2.

3.3. Effect of initial condition

Numerical simulations in the previous sections had the assumption that the laser has settled to the steady state before feedback is applied. Thus for the delay differential equations representing the delay feedback dynamics the initial condition is a constant function, namely the steady state solution without feedback. However, situations can arise where this is not the case. Feedback can be present from $t = \tau$, where τ is the delay in feedback. Here,

BEJOY et al./Turk J Phys

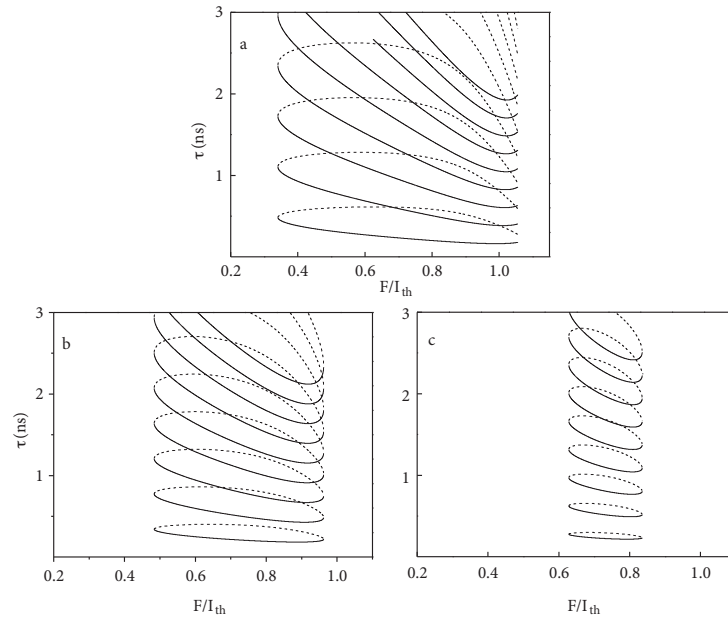


Figure 4. Critical delay curves for 3 different values of I_0 . (a) $I_0 = 1.4$, (b) $I_0 = 1.7$, (c) $I_0 = 1.9$.

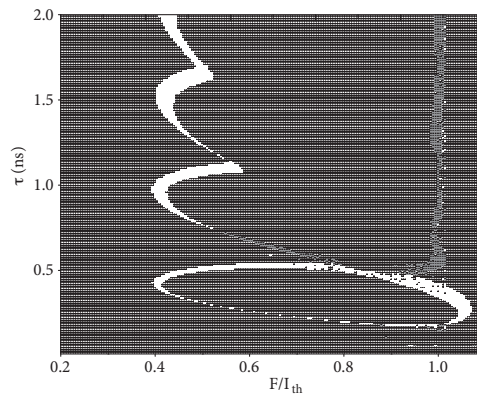


Figure 5. Differences in final states when feedback is applied after the SL is stabilized to the fixed point and before stabilization for the parameter values $I_0 = 1.5$, $\varepsilon = 0.025$. In the completely shaded region the SL goes to the same final state in both cases. In the completely unshaded area, SL goes to a fixed point when feedback is started after the laser is stabilized to the fixed point and to an oscillatory solution when the feedback is started at time $t = \tau$ (delay). In the half-shaded regions the dynamics are switched. The SL goes to an oscillatory state in the first situation and to a fixed point in the second.

if τ is shorter than the time taken by SL to stabilize to the fixed point after relaxation oscillations, the initial function is not a constant. In this scheme the parameter space is divided based on 3 types of behavior: regions where the attractor remained the same as with the previous case, regions where the attractor changed from fixed point to a limit cycle, and regions where the attractor changed from a limit cycle to a fixed point. Figure 5 characterizes the $(F/I_{th}, \tau)$ parameter space for these 3 types of behavior. One such instance for parameter values $F/I_{th} = 0.52$, $I_0 = 1.5$, and $\tau = 1.1$ ns is given in Figure 6. In Figure 6a, when the feedback is applied at $t = 50$ ns, SL is already operating at the steady state, and $P(t)$ settles to the new fixed point after damped oscillations. Figure 6b shows the case when feedback is present from 1.1 ns, which is equal to the delay. In this case $P(t)$ is undamped and slowly growing. Such points are represented by the unshaded regions in Figure 5. If $P(t)$ is oscillatory when the initial feedback function is constant, one would expect the same for a case when the initial feedback function itself is oscillatory, but we get the unexpected result as shown in Figures 6c and 6d. Here the final state is the fixed point when feedback is applied at $t = \tau$ (0.53 ns), but the final state is oscillatory when feedback is applied after the stabilization of the SL to the fixed point. The half-shaded regions in Figure 5 represent this behavior.

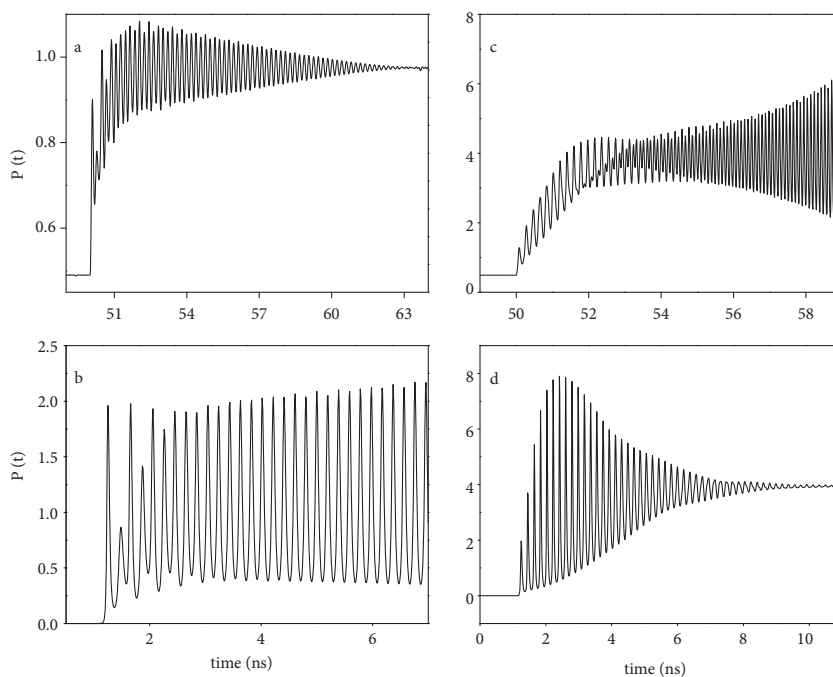


Figure 6. Solution $P(t)$ of the rate equations for 2 different initial conditions for the parameter values $F/I_{th} = 0.52$, $I_0 = 1.5$, and $\tau = 1.1$ ns. (a) Feedback is applied at 50 ns when the laser is already operating at its steady state. Dynamics converge to the new fixed point after damped oscillations. (b) Feedback mechanism is present from a time $t = \tau$ after the beginning of the operation. Here the solution goes to oscillatory state. (c) and (d) show the final states switched for $F/I_{th} = 0.99$ and $\tau = 0.53$ ns.

BEJOY et al./Turk J Phys

4. Conclusions

We have done the linear stability analysis of the nonlinear delay differential equations arising in a SL with optoelectronic delay feedback. Critical stability curves and Hopf bifurcation points obtained from the analysis are verified by simulating the delay dynamics of the SL. Here simulations are done such that delay feedback is switched on only after the SL has stabilized to the fixed point. Deviations from the predicted behavior, when the feedback is present from the beginning, are discussed. Effects of nonlinear gain reduction factor and bias current are deduced from the analysis and are numerically verified. Increase in both of these parameters reduces the range of feedback strength where the stability depends on delay. Beyond a critical value, stability of the steady state solution becomes independent of delay.

Acknowledgments

Authors Varghese Bejoy and Vadakkedath Madhom Nandakumaran thank the Board of Research in Nuclear Sciences (BRNS), India, for its financial support. The authors thank Manu P John for discussions and suggestions.

References

- [1] Soriano, M. C.; Garcia-Ojalvo, J.; Mirasso, C. R.; Fischer, I. *Rev. Mod. Phys.* **2013**, *85*, 421–470.
- [2] Weiss, C. O.; Vilaseca, R. *Dynamics of Lasers*, Wiley-VCH: Weinheim, Germany, 1991.
- [3] Krauskopf, B. In *AIP conference proceedings: Nonlinear Dynamics: Concepts, Mathematics, Physics, and Applications International Spring School*, Texel, the Netherlands, 16–19 April 2000.
- [4] Jiang, G.; Zhang, J.; Huang, Y. *Turk. J. Phys.* **2013**, *37*, 296–303.
- [5] Deng, T.; Xia, G.; Wu, Z.; Lin, X.; Wu, J. *Opt. Express* **2011**, *19*, 8762–8773.
- [6] Fujino, H.; Ohtsubo, J. *Opt. Rev.* **2001**, *8*, 351–357.
- [7] Sacher, J.; Baums, D.; Pankin, P.; Elsasser, W.; Gobel, E. O. *Phys. Rev. A* **1992**, *45*, 1983–1905.
- [8] Rajesh, S.; Nandakumaran, V. M. *Physica D* **2006**, *213*, 113–120.
- [9] Ludge, K.; Schuster, H. G. *Nonlinear Laser Dynamics: From Quantum Dots to Cryptography, Reviews of Nonlinear Dynamics and Complexity*, Wiley-VCH: Weinheim, Germany, 2011.
- [10] Erneux, T.; Glorieux P. *Laser Dynamics*, Cambridge University Press: Cambridge, UK, 2010.
- [11] Lakshmanan, M.; Senthilkumar, D. V. *Dynamics of Nonlinear Time-Delay Systems*, Springer-Verlag: Berlin, Heidelberg, Germany, 2010.
- [12] Kouomou Y. C. PhD, Department of Physics, University of the Balearic Islands, Palma de Mallorca, 2006.
- [13] Lin, F.; Liu, J. *IEEE J. Select. Topics Quantum Electron.* **2004**, *5*, 991–997.
- [14] Masoller C.; Cabeza C.; Schifino, A. S. *IEEE J. Quantum Electron.* **1995**, *31*, 1022–1028.
- [15] Krauskopf, B.; Gray, G. R.; Lenstra, D. *Phys. Rev. E* **1998**, *58*, 7190–7197.
- [16] Sacher, J.; Baums, D.; Pankin, P.; Elsasser, W.; Gobel, E. O. *Phys. Rev. A* **1992**, *45*, 1983–1905.
- [17] Vicente, R.; Tang, S.; Mulet, J.; Mirasso, C. R.; Liu, J. *Phys. Rev. E* **2004**, *70*, 046216.
- [18] Agrawal G. P. *Appl. Phys. Lett.* **1986**, *49*, 1013–1015.
- [19] Rajesh, S.; Nandakumaran, V. M. *Phys. Lett. A* **2003**, *319*, 340–347.
- [20] Lee, T. P.; Burrus, C. A.; Copeland, J. A.; Dental, A. G.; Marcuse, D. *IEEE J. Quantum Electron.* **1982**, *QE-18*, 1101–1113.

PRAMANA
— journal of
physics

© Indian Academy of Sciences

Vol. xx, No. x
xxxx xxxx
pp. 1–11

Delay signatures in the chaotic intensity output of a Quantum Dot Laser with optical feedback.

BEJOY VARGHESE^{a,*}, MANU P. JOHN^{b,†}, V.M.NANDAKUMARAN^{a,c,‡}

‡

^aInternational School of Photonics, Cochin University of Science And Technology, Kochi 22, India

^bDepartment of Physics, Union Christian College, Aluva, India

^cDepartment of Physics, Amrita School of Arts and Sciences, Amrita Viswa Vidyapeetham, Kollam, India

Abstract. Delay identification from the chaotic intensity output of a Quantum Dot Laser with optical feedback is done using numerical and information theoretical techniques. Four quantifiers, namely Auto Correlation function, Delayed Mutual Information, Permutation Entropy and Permutation Statistical Complexity are employed in delay estimation. A detailed comparison of these quantifiers with different feedback rates and delay is undertaken. Permutation Entropy and Permutation Statistical Complexity are calculated with different dimensions of symbolic reconstruction to obtain the best results.

Keywords. Quantum Dot Laser, Delay, Information Entropy, Statistical Complexity, Mutual Information

PACS Nos. 05.10.-a

1. Introduction

Research in complex systems require quantitative predictions of their dynamics, even before we completely understand the underlying mechanisms. This can only be done by collecting data about the past evolution and retrieving the structures in the dynamics from the collected data. Numerous statistical and information theoretical approaches have been successfully employed for analyzing the time series obtained from the observation of complex processes. Due to finite speed of information propagation, interaction between different components of a complex system do inevitably involve time delays. Identifying these delays are crucial for modeling and forecasting applications in different fields including biology[1], optics[2, 3] and climate science[4]. Most conventional and widely used methods for estimating delay in complex dynamics are auto correlation function (ACF) and delayed mutual information (DMI). Several new techniques were recently discovered for delay identification. Information theory measures like Entropy and Complexity have been shown to be particularly useful in the case of nonlinear systems[3, 5]. In the

*bejoyrosily@gmail.com

†tav.john@gmail.com

‡nandakumaranvm@gmail.com

present work we focus on the dynamics of a Quantum Dot Laser(QDL) with optical feedback working in the coherence collapse regime. Dynamics of QDLs show quite distinctive features compared to bulk semiconductor dynamics. Conventional Lang-Kobayashi equations fail in many places to accurately predict QDL dynamics[6]. In QDLs relaxation oscillations are strongly damped due to different carrier capture dynamics into the Quantum Dots (QDs)[7]. Strong damping added with relatively small line width enhancement factor(α) make QDLs less sensitive to optical feedback[8]. So instabilities in QDLs occur at higher feedback strengths compared to bulk or Quantum Well(QW) lasers. Synchronization of QDLs working in the chaotic regime is currently an active research area with the prospect of using them for secure communication with chaotic carriers[9]. A major concern in chaos based secure communication is the level of difficulty to identify the parameters of the chaotic emitter from the output time series. Chaos generated in feedback systems can have very high dimensionality due to the infinite number of degrees of freedom introduced by time delay. But once the delay value is retrieved from the time series, the high dimensional attractor can be projected to a low dimensional phase space, which may result in low complexity numerical techniques to decrypt the information. This security aspect of chaos based communication had been addressed for semiconductor lasers modeled with conventional Lang-Kobayashi equations[3, 10, 11]. Rontani et.al. [10] showed that a careful choice of laser operating conditions can make delay retrieval extremely difficult. In another work [11], the same group also demonstrated that the time scales of laser dynamics in its route to chaos influence the difficulty in delay identification. Recently, information theory measures like permutation entropy(H_S) and permutation statistical complexity(C_{JS}) were employed to get good estimates of delay value from the time series of delay differential systems. Soriano et. al.[3] used this approach to find the intrinsic time scales in the dynamics of a semiconductor laser with optical feedback operating in the coherence collapse regime. We use ACF,DMI, H_S and C_{JS} to retrieve delay from the chaotic output intensity series of a QDL with external cavity. Reliability of these measures are investigated when external cavity round trip time and feedback rates are varied.

2. Theoretical Framework

2.1 Rate Equation Model

We adopt the dynamical model of QDL from Ref. [8]. This model presumes that the carriers are first injected into the quantum well before being captured into the quantum dots. The dynamics is described by the following set of delay differential equations that give the time evolution of the complex amplitude of the electric field(E), occupation probability in a dot(ρ) and the carrier density in the well(N).

$$\dot{E} = -\frac{E}{2\tau_s} + \frac{g_0 V}{2} (2\rho - 1) E + i\frac{\delta\omega}{2} E + \frac{\gamma}{2} E(t - \tau) \quad (1)$$

$$\dot{\rho} = -\frac{\rho}{\tau_d} - g_0 (2\rho - 1) |E|^2 + F(N, \rho) \quad (2)$$

$$\dot{N} = \frac{J}{q} - \frac{N}{\tau_n} - 2N_d F(N, \rho) \quad (3)$$

τ_s, τ_n and τ_d are the photon lifetime, carrier lifetime in the well and the carrier lifetime in the dot, respectively. $g_0 = \sigma v_g$ where σ is the cross section of interaction of the carriers in the dots with the electric field and v_g is the group velocity. $V = 2N_d\Gamma/d$, where N_d is the two dimensional density of dots, Γ is the confinement factor and d is the thickness of the dot layer. γ is the feedback rate and τ is the delay involved in the feedback process. $F(N, \rho)$ is the rate of exchange of carriers between the well and dots and is given by $F(N, \rho) = R_{cap}(1 - \rho) - R_{esc}\rho$. $R_{cap} = CN^2 + BN$ where B describes carrier-phonon capture and C describes Auger carrier capture. For simulations B is taken as zero. This is justified because discrete nature of QD energy levels and fixed energies of Longitudinal Optical (LO) phonons make carrier-phonon capture in QD structures highly improbable [7]. Temperature dependent carrier escape from the dots is given by R_{esc} . $\delta\omega$ take into account the dependence of laser frequency on carrier densities in QW and QD regions. $\delta\omega = \beta_1 N + \beta_2 \rho$ where plasma effect from the carriers in the well is described by β_1 and variations caused by population in the dots is described by β_2 [8]. The values used in the simulations are $\tau_s = 3ps$, $\tau_n = \tau_d = 1ns$, $g_0 = 0.9259 \times 10^{-10} m^3 s^{-1}$, $V = 2.4 \times 10^{22} m^{-3}$, $N_d = 2 \times 10^{15} m^{-2}$, $\beta_1 = 0$, $\beta_2 = 2$, $C = 10^{-20} m^4 s^{-1}$, $R_{esc} = 0$ [8].

2.2 Auto Correlation Function

ACF quantifies the linear relationship between a signal and its time-shifted version. ACF for a random process $X(t)$ is defined as

$$\Gamma(\theta) = \frac{1}{\sigma_X^2} \langle (x(t) - \hat{\mu}_X)(x(t + \theta) - \hat{\mu}_X) \rangle \quad (4)$$

$x(t)$ and $x(t + \theta)$ are sampled from $X(t)$. $\hat{\mu}_X = \langle x(t) \rangle$ and $\hat{\sigma}_X = \langle (x(t) - \hat{\mu}_X)^2 \rangle^{1/2}$. $\langle \cdot \rangle$ denotes expectation value.

2.3 Permutation Entropy

One of the natural approaches to quantify the information content of a process is the Shannon Entropy(H). H is calculated from a probability distribution $P = \{p_i : i = 1, \dots, M\}$ of some observable, associated with the process. M represent the total number of states the observable can take.

$$H[P] = - \sum_{i=1}^M p_i \ln(p_i) \quad (5)$$

It is also the measure of uncertainty associated with the process. If we can perfectly predict the outcome at any instant, there is minimum uncertainty, and $H[P] = 0$. In contrast, if there is equal probability for all the states to occur, uncertainty is maximum and $H[P_e] = \ln(M)$. Here P_e denotes uniform probability distribution $P_e = \{1/M, 1/M, \dots, 1/M\}$. To find the associated probability distribution, we use Bandt and Pompe symbolization method, which has recently been applied successfully in the time series analysis of chaotic dynamical systems. A detailed description about the method is given in references [3] and [5]. The method is briefly explained below. Given a time series $x_t, t = 1, 2, \dots, n$, an embedding dimension D and a time delay (τ), a D dimensional

vector is constructed as

$$s \mapsto (x_{s-(D-1)\tau}, x_{s-(D-2)\tau}, \dots, x_{s-\tau}, x_s) \quad (6)$$

This vector is then rearranged as

$$x_{s-r_0\tau} \geq x_{s-r_1\tau} \geq x_{s-r_2\tau} \dots \geq x_{s-r_{D-2}\tau} \geq x_{s-r_{D-1}\tau} \quad (7)$$

to get an ordinal pattern

$$\pi = (r_0, r_1, \dots, r_{D-1}) \quad (8)$$

Each possible ordinal pattern that is generated in this way, is an element of the set of all permutations of $(0, 1, \dots, D-1)$. If we have a sufficiently long time series that satisfy $N \gg D!$, an ordinal pattern probability distribution $P = \{p(\pi_i), i = 1, 2, \dots, D!\}$ can be generated. Shannon Entropy calculated using this probability distribution is the Permutation Entropy denoted by H_S . In the following discussions, Permutation Entropy is always used in the normalized form given by

$$H_S[P] = H[P]/H[P_c]. \quad (9)$$

2.4 Delayed Mutual Information

Mutual Information of two discrete random variables X & Y , is defined as [10, 11]

$$I(X, Y) = \sum_{x \in X} \sum_{y \in Y} p(x, y) \log \left(\frac{p(x, y)}{p(x)p(y)} \right) \quad (10)$$

where $p(x)$ and $p(y)$ are marginal probability density functions and $p(x, y)$ is the joint probability density function. DMI can also be defined in terms of H

$$I(\theta) = H(X(t)) + H(X(t + \theta)) - H(X(t), X(t + \theta)) \quad (11)$$

DMI between $X(t)$ and $X(t + \theta)$ can be obtained from the first definition as

$$I(\theta) = \sum_{x, x(t+\theta) \in X} p(x(t), x(t + \theta)) \log \left(\frac{p(x(t), x(t + \theta))}{p(x(t))p(x(t + \theta))} \right) \quad (12)$$

2.5 Permutation Statistical Complexity

Statistical Complexity measures can provide useful information about the structure of the underlying dynamics when the dynamics is not perfectly random or ordered[12]. So by definition, statistical complexity goes to zero as the process tend to either of these

extremes.[13, 14] Permutation Statistical Complexity (C_{JS}) is defined over two probability distributions - probability distribution of the ordinal patterns(P) obtained as discussed previously and the uniform distribution(P_e).

$$C_{JS}[P] = Q_J[P, P_e]H_S[P] \quad (13)$$

where Q_J is the disequilibrium which quantify how distant P is from P_e . Q increases if the system has preferred states among the accessible ones. Q_J is defined in terms of Jensen-Shannon divergence $\mathcal{J}[P, P_e]$.

$$Q_J[P, P_e] = Q_0 \mathcal{J}[P, P_e] \quad (14)$$

with

$$\mathcal{J}[P, P_e] = H[(P + P_e)/2] - H[P]/2 - H[P_e]/2 \quad (15)$$

Q_0 is a normalization constant corresponding to the maximum possible value of $\mathcal{J}[P, P_e]$ which is equal to $-2 \{((N + 1)/2) \ln(N + 1) - 2 \ln(2N) + \ln N\}^{-1}$. Maximum value for $\mathcal{J}[P, P_e]$ occurs for a distribution P, which has a particular component (p_j) equal to 1, and all the remaining components zero.

3. Numerical Simulations

Dynamical equations are scaled properly before performing numerical calculations. Time(t) is nondimensionalized by scaling it with respect to the photon lifetime as $t/2\tau_s$. Feedback rate(γ) and Electric field(E) are scaled as $\tau_s\gamma$ and $(2\tau_s g_0)^{-1/2}E$, respectively. Simulations are done using second order Runge-Kutta method and the output is sampled with a period $\Delta_s = 0.01$. 2×10^8 points are used for the calculations. Figure 1 shows the graph of the four quantifiers discussed in previous sections for $\gamma = 0.18$ and $\tau = 66.66$. This delay value corresponds to 400ps in the original time scale. Relaxation oscillation period is approximately 89ps which scale to $\tau_{RO} \approx 14.83$. Figure 1a shows ACF as a function of the shift in time series. ACF does not have any vividly indicative feature near the value of τ , from which one can estimate the time delay involved in the feedback process. In contrast to ACF, all the other three quantifiers give an affirmative indication of the delay. For highly nonlinear systems like QDL with optical feedback, it is necessary to detect the nonlinear nonlocal time correlations in the output intensity series if one wants to estimate the inherent delay in the time evolution of state variables. The ambiguity in delay estimation from ACF is attributed to the fact that it detect only linear correlations[11]. Figure 1b plot DMI with the inset graph showing the enlarged portion near the delay value. There is a pronounced peak near τ , which is slightly shifted to the right. This shift originate from the finite response time of the laser. The prediction of the response time beforehand is difficult and is an inherent property of the laser. Two less dominant peaks appear on both sides of the delay peak at $\tau \pm \tau_{RO}/2$. In the figure the peak on the higher side of τ is more dominant than on the lower side. The height of the delay peak as well as of the sidebands depends on the value of γ . This dependence is discussed later in this section. Figure 1c & 1e shows the plots obtained for H_S and C_{JS} for D values from 5 to 9. When the dynamics is reconstructed with a proper value of delay, a minimum in entropy and a maximum in complexity are expected. 1c shows the plot of both the measures together. The more

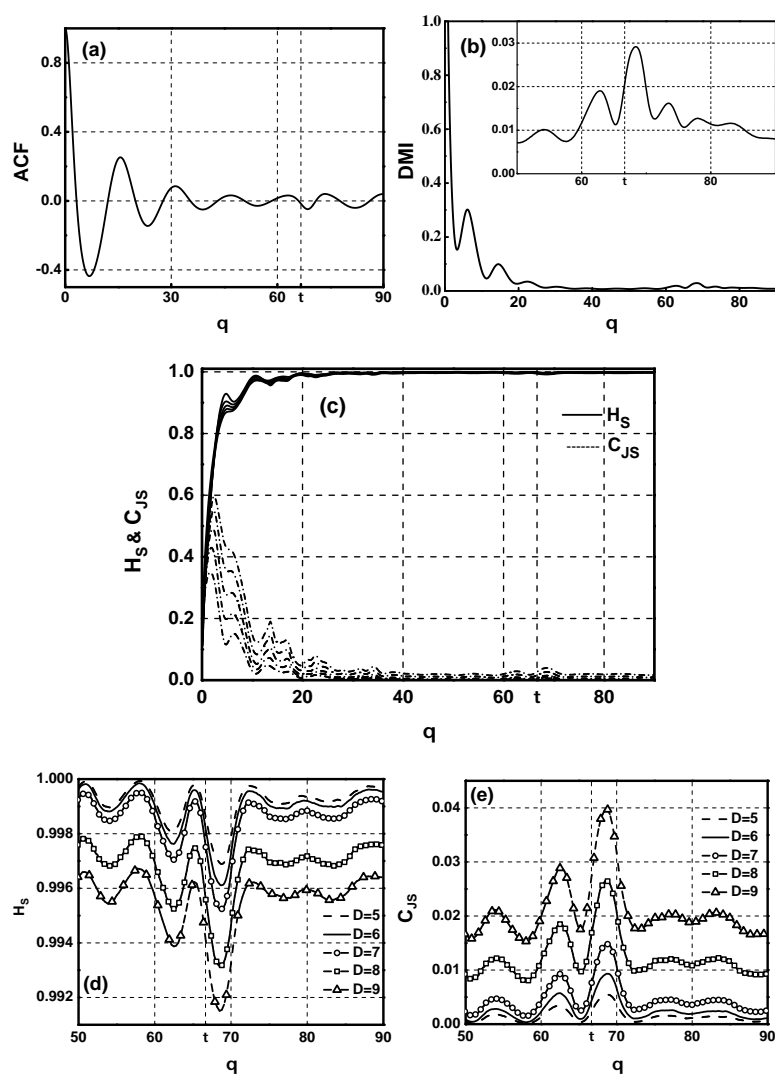


Figure 1. ACF, DMI, H_S and C_{JS} calculated from output intensity time series of QDL for $\tau = 400ps$ and $\gamma = 0.18$. For H_S and C_{JS} , D is varied from 5 to 9.

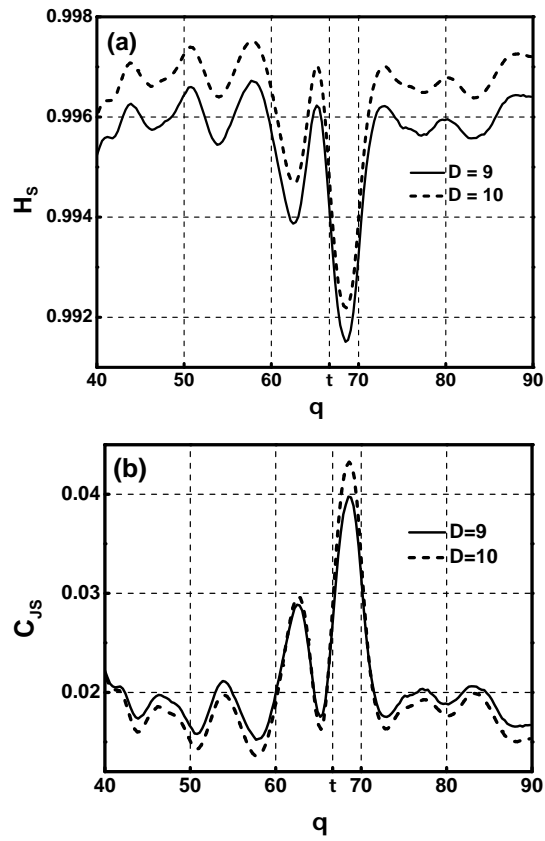


Figure 2. H_S and C_{JS} for D equal to 9 and 10. $\tau = 400ps$ and $\gamma = 0.18$

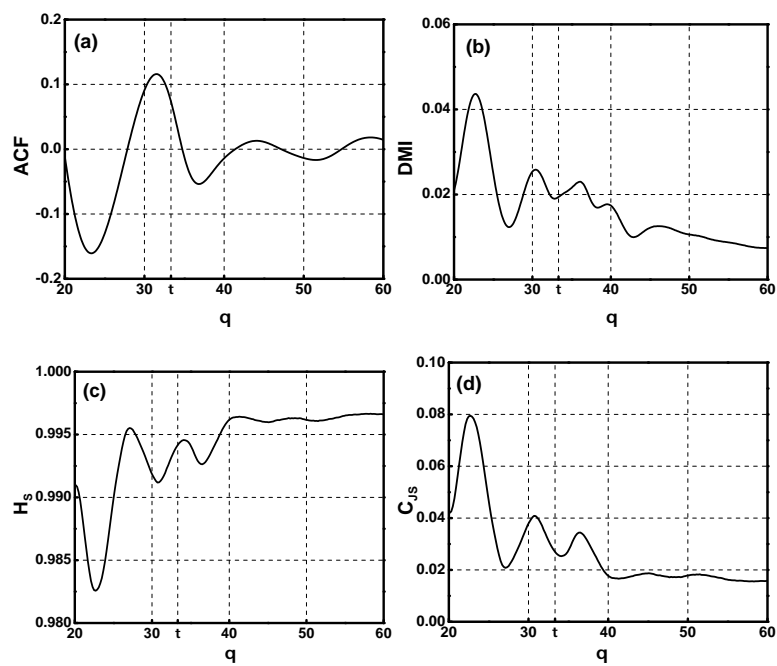


Figure 3. ACF, DMI, H_S and C_{JS} calculated from output intensity time series of QDL for $\tau = 33.33(200ps)$ and $\gamma = 0.18$. D is taken as 9 for H_S and C_{JS}

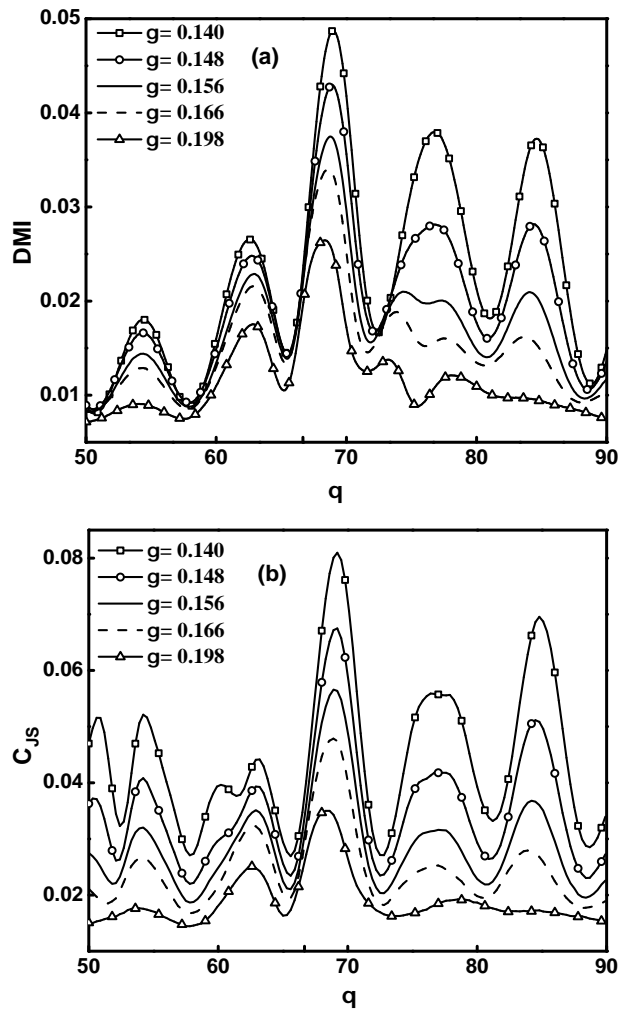


Figure 4. DMI and C_{JS} calculated for six different values of feedback rate(γ) with $\tau = 66.66(400ps)$

pronounced C_{JS} peak is visible in this plot, but it is difficult to spot the dip in H_S as its contrast from the baseline is low. The dip in H_S and the peak in C_{JS} near $\theta = \tau$ is evident from the enlarged graphs in figure 1d and 1e. Like DMI, delay estimation from both these measures suffer from the finite response time of the laser. Shift in the peak(dip) from the actual value of delay is found to be the same in all the three cases. In the complexity and entropy plots, the peak(dip) at $\tau + \tau_{RO}/2$ is suppressed while the one at $\tau - \tau_{RO}/2$ is visible. As the dimensionality of reconstruction increases the delay signature become prominent in both H_S and C_{JS} . But increasing D to 10 give a different result. In Figure 2 entropy and complexity are plotted for D equal to 9 and 10. For $D = 10$, H_S increases for all the values of θ reducing the contrast of the dip near τ . But C_{JS} peaks near $\theta = \tau'$ and $\tau' - \tau_{RO}'/2$ are enhanced. Interestingly, for other values of θ , $C_{JS}[D = 10]$ is less than $C_{JS}[D = 9]$. This shows that better delay retrieval using higher values of D is possible if one uses C_{JS} , even when H_S fail to give an estimation. For higher values of D, we get better contrast for the delay peak because the values of complexity in the background get considerably reduced. Next we perform the same calculations for $\tau \approx 33.33(200ps)$ keeping all other parameters constant. The results are given in Figure 3. H_S and C_{JS} are plotted only for $D = 9$. Even with a closer scrutiny no affirmative feature indicative of delay can be spotted in any of the four plots. This reveal the practical impossibility of delay identification when the actual delay get closer to the relaxation oscillation period. Numerous correlations exist in the QDL dynamics which die only long after the value of θ exceeds the value of τ . So when the delay get closer to the relaxation oscillation period, the delay signature get immersed in these correlations and a proper estimation becomes impossible. Finally we study the behavior of DMI and C_{JS} when feedback rate is varied. Figure 4a& b shows these quantifiers for six different values of γ . Delay is set to 66.66(400ps) in all the cases and the feedback rates are chosen such that the dynamics is chaotic. For both DMI and C_{JS} higher peaks are obtained for lower values of γ . In the figure highest peak is obtained for the value of γ equal to 0.14. But due to the pronounced peaks at $\tau \pm \tau_{RO}/2$, delay estimation can become ambiguous. As feedback rate increases the delay peaks reduce height but since the nearby peaks diminish faster, contrast from the baseline get enhanced. Especially for C_{JS} , peaks at $\theta > \tau$ get flattened. When feedback rate is high the delay estimation become more accurate because the shift due to the finite laser response time reduces and the peaks get more closer to the actual value of the delay. This happens identically for both DMI and C_{JS} .

4. Conclusions

We investigate the delay estimation scenarios from the chaotic time series using four quantifiers - namely Auto Correlation Function, Delayed Mutual Information, Permutation Entropy and Permutation Statistical Complexity. These numerical and information theoretical techniques are applied to the chaotic output intensity of a Quantum Dot Laser with optical feedback. A detailed comparison of these measures is performed for different feedback rates and the delays. From the numerical calculations performed, we find Permutation Statistical Complexity to be the best candidate due to its distinctive maximum close to the delay. Also, we show that higher dimensionality of symbolic reconstruction will work with Permutation statistical complexity to get better contrast against the background as opposed to Permutation Entropy. Auto Correlation Function fails to give a distinctive identification unlike the other three measures. When the delay involved in feedback is close to the relaxation oscillation period of the laser, delay identification becomes practically impossible with any these techniques. Due to the finite laser response

time all the measures have an error which give a slightly higher estimation of delay. For high feedback rates delay estimation become more accurate because the shift due to finite laser response reduces.

5. Acknowledgements

Authors thank BRNS for its financial support.

References

- [1] MC Mackey and L Glass, *Science* **197**, 4300, 287 (1977). <http://www.sciencemag.org/content/197/4300/287.full.pdf>, URL <http://www.sciencemag.org/content/197/4300/287.abstract>.
- [2] Christian Otto, Kathy Ldge and Ekehard Schll, *physica status solidi (b)* **247**, 4, 829 (2010). URL <http://dx.doi.org/10.1002/pssb.200945434>.
- [3] M.C. Soriano, L. Zunino, O.A. Rosso, Ingo Fischer and C.R. Mirasso, *Quantum Electronics, IEEE Journal of* **47**, 2, 252 (2011).
- [4] Eli Tziperman, Lewi Stone, Mark A. Cane and Hans Jarosh, *Science* **264**, 5155, 72 (1994). <http://www.sciencemag.org/content/264/5155/72.full.pdf>, URL <http://www.sciencemag.org/content/264/5155/72.abstract>.
- [5] L. Zunino, M. C. Soriano, I. Fischer, O. A. Rosso and C. R. Mirasso, *Phys. Rev. E* **82**, 046212 (2010). URL <http://link.aps.org/doi/10.1103/PhysRevE.82.046212>.
- [6] AminH. Al-Khursan, BasimAbdullattif Ghalib and SabriJ. Al-Obaidi, *Semiconductors* **46**, 2, 213 (2012). URL <http://dx.doi.org/10.1134/S1063782612020029>.
- [7] A. V. Uskov, Y. Boucher, J. Le Bihan and J. McInerney, *Applied Physics Letters* **73**, 11, 1499 (1998). URL <http://scitation.aip.org/content/aip/journal/apl/73/11/10.1063/1.122185>.
- [8] D. O'Brien, S. P. Hegarty, G. Huyet and A. V. Uskov, *Opt. Lett.* **29**, 10, 1072 (2004). URL <http://ol.osa.org/abstract.cfm?URI=ol-29-10-1072>.
- [9] Basim Abdullattif Ghalib, Sabri J. Al-Obaidi and Amin H. Al-Khursan, *Optics & Laser Technology* **48**, 0, 453 (2013). URL <http://www.sciencedirect.com/science/article/pii/S0030399212005385>.
- [10] D. Rontani, A. Locquet, M. Sciamanna and D. S. Citrin, *Opt. Lett.* **32**, 20, 2960 (2007). URL <http://ol.osa.org/abstract.cfm?URI=ol-32-20-2960>.
- [11] D. Rontani, A. Locquet, M. Sciamanna, D.S. Citrin and S. Ortin, *Quantum Electronics, IEEE Journal of* **45**, 7, 879 (2009).
- [12] M.T. Martin, A. Plastino and O.A. Rosso, *Physica A: Statistical Mechanics and its Applications* **369**, 2, 439 (2006). URL <http://www.sciencedirect.com/science/article/pii/S0378437106001324>.
- [13] B A Huberman and T Hogg, *Phys. D* **2**, 1-3, 376 (1986). URL <http://dl.acm.org/citation.cfm?id=25201.25226>.
- [14] M.T Martin, A Plastino and O.A Rosso, *Physics Letters A* **311**, 23, 126 (2003). URL <http://www.sciencedirect.com/science/article/pii/S0375960103004912>.

